The Hong Kong Polytechnic University

Department of Applied Physics

All-oxide Giant Magnetoresistive Devices

Chan Yuk Kwan

A thesis submitted in partial fulfillment of the

requirements

for the degree of master of Philosophy

August 2008

CERTIFICATE OF ORIGINALITY

I hereby declare that this thesis is my own work and that, to the best of my knowledge and belief, it reproduces no material previously published or written, nor material that has been accepted for the award of any other degree or diploma, except where due acknowledgement has been made in the text.

_____

Chan Yuk Kwan

Abstract

Giant magnetoresistance effect (GMR) has been broadly employed in hard disk read heads and non-volatile memory devices since its discovery by Albert Fert and Peter Grunberg. The importance of GMR was further confirmed by their sharing of the Nobel Prize in 2007. Commercial GMR devices are dominated by spin valve (SV) structures, in which a thin non-magnetic layer is sandwiched between two ferromagnetic layers. Currently, commercial SV are dominated by metal-based structures, because of their simplicity in theoretical treatment and fabrications. Recently, all-oxide SVs and oxide-based SVs have attracted research interests, using oxide materials with high spin polarization such as CrO_2 and rare-earth doped manganites like (La,Sr)MnO_3. The aim of this project is to demonstrate GMR in all-oxide SVs with such oxides.

In this work, I fabricated pseudo SV (PSV) devices, which do not rely on antiferromagnetic layers for introducing coercivity contrast between magnetic layers. Well-defined magnetic states were achieved by intrinsic differences between coercivities of the two ferromagnetic layers. The materials selected in this work were $La_{1-x}A_xMnO_3$ (where A = Ca and Sr) for ferromagnetic electrodes and $LaNiO_3$ (LNO) for non-magnetic layer. All samples were fabricated by pulsed laser deposition (PLD). PLD is an advanced technique to deposit thin

films which can retain the stoichiometry of target materials.

This work was primarily divided into two parts. The first part was the optimization of deposition conditions for each layer in the PSV. The second part was concerned with measurements of the PSV devices.

The surface morphology and crystallinity of thin films were investigated by atomic force microscopy and x-ray diffractometry. GMR responses are generally worsened by rough surfaces and poor crystallinity of thin films. Precise optimization of deposition parameters, such as substrate-to-target distances, laser fluence, repetition rate and oxygen pressure, are therefore necessary to obtain thin films with extremely flat surfaces and highly crystalline structure. Two PLD systems were utilized to deposit thin films in this project, one was a typical PLD system and the other one a laser molecular beam epitaxy (LMBE) system. Compared with PLD, LMBE can produce epitaxial films with atomic flatness. Experimental results showed that the roughness (~1 nm) and crystallinity (FWHM ~ 0.2° obtained from ω-scan) of the films fabricated by LMBE were superior to those produced by PLD. Magnetic properties, such as magnetization and coercive field of the separate layer were studied by vibrating sample magnetometer. For 100 nm thick $La_{0.7}Sr_{0.3}MnO_3$ (LSMO) thin films on $LaAlO_3$ (LAO) (001) substrates, Curie temperatures were about 330 K, as estimated by

both magnetization-temperature and resistance-temperature measurements.

After the optimization of deposition parameters, PSV devices were fabricated. All devices were prepared by standard processes of UV-lithography, dry etching and lift-off. There are two measurement configurations for demonstrating GMR effect, namely current-in-plane (CIP) and current-perpendicular-to-plane (CPP) geometries.

CIP devices were fabricated with PSV structure $La_{0.67}Sr_{0.33}Mn_{0.95}Ru_{0.05}O_3$ (LSMRO) (100 nm)/ LNO(15 nm)/LSMO(50 nm). Ru doping in LSMO has been shown to induce coercivity enhancement 2.5 times that of LSMO (~100 Oe at 80K). Double coercivity was clearly observed in the devices. Magnetoresistance measurements were performed on the device at 10 K.

LSMO(50 nm)/ LNO(15 nm)/$La_{0.7}Ca_{0.3}MnO_3$ (25 nm) PSV, prepared to be fabricated into CPP device, was deposited on LAO with LNO as the bottom electrode. Microstructural analysis showed the epitaxial nature of the films, and hysteresis loop measurements illustrated double coercivity characteristic of the heterostructure. Successful preparation of PSV structures described here would serve as a protocol for further investigations of spin transport in other oxide systems.

List of Publications

1. W.F.Cheng, A.Ruotolo, Y.K.Chan, K.H.Wong and C.W.Leung, "Spacerless metal-manganite pseudo-spin-valve structure," *J. Appl. Phys.*, vol. 103, pp. 103903, 2008.

2. Y.K.Chan, W.F.Cheng, H.K.Lau, C.W.Leung, “Study of Coercivity-enhanced Ruthenium-doped $La_{0.67}Sr_{0.33}MnO_3$ Thin Films for Pseudo Spin Valve Devices,” Mater. Res. Soc. Symp. Proc., vol. 1074, I03-06

Acknowledgement

I have benefited from the help and assistance of numerous people during the study in past two years. First, I am certainly indebted to my supervisor, C.W.Leung for his patient guidance. I especially enjoy the lunches on saturdays with him when he shared his experience in research. No words can actually describe my appreciation to him. None of this work would have been possible without his help and efforts. I also wish to thank Prof. K.H.Wong and Dr. C.L.Mak for their useful scientific discussions in the group meetings. Special thanks to W.F.Cheng for everything (too many to be specified) that he taught me. I am grateful to C.Y.Lam for training me on the PLD system and the XRD. Thanks must also go to Matthew for assistance on all computer-related matters and for training me on the AFM. Particular thanks must go to an Italian, Antonio for teaching and training me on the photolithography process. I would also like express my sincere thanks to an American engineer, Travis for training me the VSM and Hall system in 5 days.

The people have made my life more enjoyable in research, office and lab in these two years. So, in no particular order, many thanks to Irene, Janet, Pai, CK, Wen Chao, Bang, Boscope, Jin Xing, Flora, Willy, Yin (Antony), Ming, Fred, Argus and Alfa.

Finally, away from the campus, this work could not be possible without the great love from my parents and brothers. Lastly, I would like to express my utmost appreciation to my girlfriend, Law Mui Mui for her unconditional love and support.

This work was supported financially by the Research Grants Council of the Hong Kong Special Administrative Region, China (project No. PolyU 5216/06E).

Table of contents

List of Figures

List of Tables

Chapter 1 Introduction

1.1 Motivation of this thesis

The giant magnetoresistive (GMR) effect, in which the resistance of magnetic multilayers or granular systems change by the order of 10% in the presence of an applied magnetic field, opens up a new field of research which utilizes the spin degree of freedom in charge carriers, namely, spintronics (Section.1.3). Recent experiments of current-induced magnetization switching [1.1-1.3] even demonstrated that in such GMR systems the magnetization could be controlled by current instead of magnetic field. GMR-based devices are therefore one of the candidates for the next-generation nonvolatile memory devices. However, the large current density required ($>10^7$ A/cm^2) for device operations is not suitable for those metallic structures due to electromigration problem. Two approaches were suggested to overcome this problem: (1) to reduce the current density and (2) to replace metallic systems with more robust structures.

In this work, the second route was adopted, and I investigated all-oxide GMR system because of its high structural tolerance compared with metallic ones. Besides, reports on GMR effect in all-oxide structures were very scarce,

and those reporting magnetization switching by means of current in such structures were even less. Detailed investigations, such as the effect of interfaces between different oxide layers or the spin diffusion lengths of non-magnetic conducting oxides on GMR, are required for a deeper understanding of GMR effect in such systems. Successful demonstration of these effects will be a crucial step towards the realization of non-magnetic-field controlled magnetic devices.

Materials in GMR devices are required to be conductive, and perovskite oxides are chosen among conductive oxides (the reasons and details of which will be presented in Section.1.4). Pseudo spin valve (PSV) structure (Section.3.2) was selected to show magnetoresistive effect due to its simplicity in fabrication. The proposed devices were fabricated by pulsed laser deposition (PLD) and photolithography processes.

1.2 Giant magnetoresistance

Year 2007, the second year I engaged into the research of GMR effect, was a milestone for modern electronic devices. In this year, Albert Fert and Peter Grunberg were awarded the Nobel Prize in Physics [1.4-1.6] for their discovery of GMR effect. Needless to say, massive data storage devices such as iPods, ultra-lightweight mobile laptops could not be made possible without the discovery of GMR. GMR is therefore of great importance in terms of

information storage industry and more importantly, it has started the research on the manipulation of *spin* degree of freedom in charge carriers.

GMR effect, discovered individually by Fert [1.7] and Grunberg [1.8] in 1988, originates from the imbalanced scattering of electrons when they are traveling through two separated ferromagnetic conductors. The degree of scattering depends on the relative orientations between electron spins and the magnetization directions of the conductors. An antiparallel magnetization configuration in the two magnetic layers represents the high resistance state, while the parallel configuration is the low resistance state. It should be noted that although Fert and Grunberg discovered GMR when they investigated metallic multilayers, there is a wide range of materials (e.g. oxides [1.9, 1.10] and organic materials [1.11, 1.12]) that can exhibit GMR.

The significant changes in resistances in response to slight variations of magnetic field make GMR devices extremely sensitive to magnetic field. The phenomenon was therefore quickly employed in magnetic recording heads, which were first commercialized in 1997 [1.4]. Until now, over 5 billion recording heads have been manufactured, and GMR heads were gradually replaced by ones utilizing tunneling magnetoresistance (TMR) effect (Chapter 3). Many scientists suggested that GMR and TMR can also be used in non-volatile

data storages as magnetic random access memory (MRAM) [1.13]; such MRAMs have advantages of non-volatility and low energy consumption compared with conventional DRAM and SRAM.

As mentioned above, GMR refers to a large resistance change induced by means of magnetic field. Interestingly, such enormous resistance changes can also be realized by current injection [1.1, 1.2]. In 1996, Slonczewski [1.14] suggested the possiblility of current-induced resistance changes, and explained this with spin torque. Spin torque received considerable attention from experimentalists [1.3, 1.15-1.18] and theorists [1.19] in recent years. In addition, microwave generation by spin torque induced magnetic precession [1.20, 1.21] provides another research direction. Apart from data storage devices, Baselt *et al.* [1.22] even promoted the idea of GMR for biological application, details of which were reviewed by Megens and Prins [1.23].

1.3 Spintronics

Figure.1.1 summarizes important discoveries about electron spins. As early as 1896, Zeeman effect already suggested the presence of the spin degree of freedom, although it had not been discovered when Zeeman observed the effect. Unlike charges, electron spins were ignored in the mainstream charge-based electronics in the 20th century. Even with the discovery of dilute magnetic

semiconductors by Robert Gałązka and colleagues [1.25], few scientists thought about incorporating spins into their electronic devices. Luckily, inspired by the birth of GMR, many researchers began to contemplate the function of spins and since then, spintronics ("spin" elec"tronics") attracted great interests from research institutes and the storage industry [1.26-1.32] because of its underlying physics and potential applications.

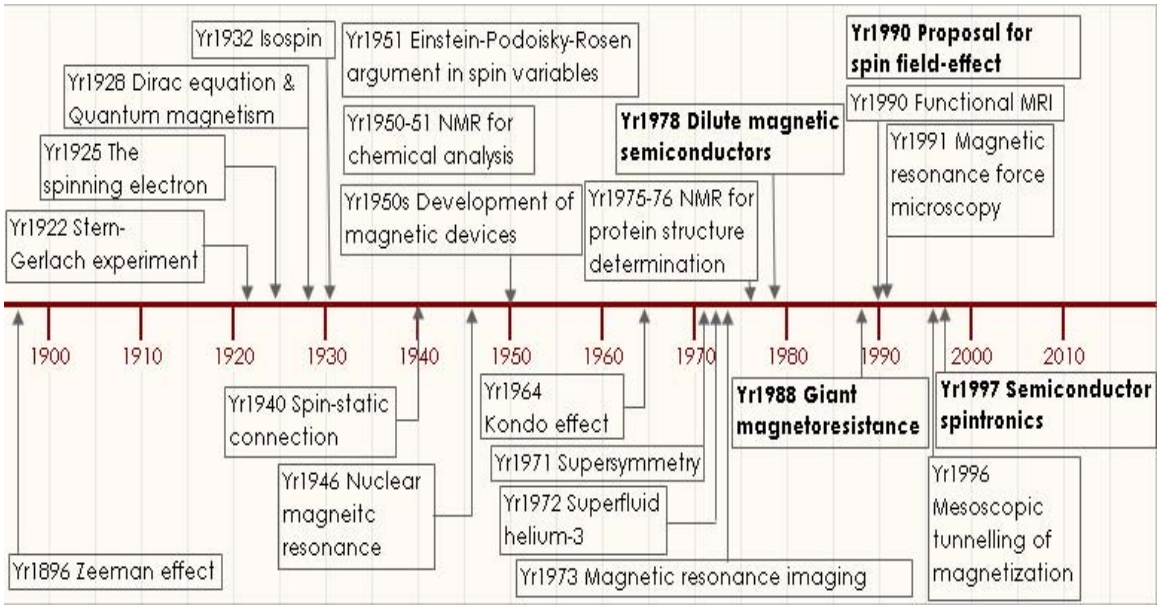

Figure 1-1 A timeline showing milestones for spin-related researches. (After Ref.[1.24])

In the field of spintronics, the major interests are achieving high spin polarization, and retaining specific spin states for the longest-possible time. Material scientists tried to achieve the first goal by using half metallic materials (Chapter 2), a new class of materials proposed by de Groot in 1983 [1.33]. Promising half metallic materials, including Heusler alloys [1.34], perovskite manganese oxides (the material used in this work) [1.35], and CrO_2 [1.36, 1.37]

have been intensively studied. Research efforts are also focused on maintaining the spin states in mateials, because of the potential outstanding performance of quantum computers [1.38]. Such investigations have been done on nanostructures, e.g. carbon nanotubes [1.39] and quantum dots [1.40], or in novel materials including oxides [1.41] and organics materials [1.42]. Datta and Das took one step forward and suggested the spin field effect transistor (spin FET) [1.43]. The spin FET possesses entirely different functionalities compared with conventional FET devices. Lastly, the electronics industry is interested in incorporating spin-based devices into silicon-based electronics [1.31].

1.4 Material Selection

For ferromagnetic electrodes in my PSV devices, rare-earth optimally-doped lanthanum manganites (mainly $La_{0.67}Sr_{0.33}MnO_3$) and their derivatives were chosen because of the following reasons.

1. They are half-metallic, and therefore the devices can possibly attain high resistance changes.
2. Theoretical predictions suggested that the current density required for magnetization switching in GMR devices is inversely proportional to the spin polarization, and roughly proportional to the saturation magnetization. Since rare-earth-doped lanthanum manganites are half metallic (i.e. with 100% spin

polarization) compared with ~20-40% in 3d transition metals, and have low saturation magnetization (~500 emu/cm^3) compared with Co (1440 emu/cm^3), they are suitable candidate for such devices in these regards.

3. They have comparatively low resistivity among conductive oxides.
4. Many perovskite oxides have similar lattice constants, and this allows epitaxial growth of oxide films on typical single crystal substrates such as $SrTiO_3$ (STO) or $LaAlO_3$ (LAO).
5. $La_{0.67}Sr_{0.33}MnO_3$, for example, is a room temperature ferromagnet (i.e. Curie temperature above room temperature), and therefore room temperature GMR device is possible in this regard.

In this study, four different lanthanum manganites were employed, including $La_{0.7}Sr_{0.3}MnO_3$ (LSMO), $La_{0.7}Ca_{0.3}MnO_3$ (LCMO), $(La_{0.85}Nd_{0.15})_{0.7}Sr_{0.3}MnO3$ (LNSMO), and $La_{0.67}Sr_{0.33}Mn_{0.95}Ru_{0.05}O_3$ (LSMRO).

The aforementioned LSMO was primarily used in this work. For demonstrating GMR effect, PSV relies solely on the difference between coercivities of two ferromagnetic layers. Normally, coercivity contrast was achieved by depositing ferromagnetic layers of different thicknesses and identical compositions. This approach limits the design of PSV, for example on layer thicknesses. Therefore, other magnetic materials were used for inducing

coercivity contrast between two ferromagnetic electrodes, in order to produce well-defined antiparallel magnetization state and hence introduce pronounced step-like magnetoresistance responses.

It was suggested [1.44] that low-level Ru-doping in LSMO would induce a charge transfer between Ru and Mn ions through the reaction $Mn^{4+}+Ru^{4+}\rightarrow Mn^{3+}+Ru^{5+}$. The (antiferromagnetic) coupling between Mn and Ru spins, together with the strong spin-orbit interaction of Ru-site spins, was postulated to cause a much stronger magnetic anisotropy and hence larger coercivity than the otherwise undoped LSMO. Interestingly, various properties of the Ru-doped LSMO (such as lattice parameters, saturation magnetization, Curie temperature and resistivity) were not dramatically affected by Ru doping. Such properties favor the combination of LSMO and LSMRO as the soft and hard layers of spin valves or magnetic tunnel junctions [1.45]. It should be noted that there is some controversy concerning the Ru-doping approach, as very different results have been reported in literature[1.46].

Apart from B-site doping (Ru doping is in the B site of perovskite structure i.e.ABO_3), A-site doping by Nd was also employed to produce coercivity contrast, as reported previously by researchers in the Department of Applied Physics (AP) [1.47, 1.48].

LCMO is another doped lanthanum manganite that is under intensive studies. LCMO (~500Oe) is well known to have larger coercivity than LSMO (~50-100Oe) at low temperature. The marked coercivity contrast is enough to fabricate a magnetoresistive device with reproducible step-like magnetoresistance behavior. As repeatable production of LSMRO films was very difficult using the thin film deposition system in AP, LCMO was an alternative to introduce coercivity contrast with LSMO in PSV. The main drawback for using LCMO as one of the ferromagnetic layers in PSV is that the Curie temperature of LCMO is only 260K, which is slightly below the room temperature. PSV utilizing LCMO can only be operated at low temperatures.

Regarding the choice of spacer layer in PSV, $LaNiO_3$ (LNO) is the only suitable candidate as it is paramagnetic as well as highly conductive in the temperature range (10-400K) to be measured. It has a resistivity which is about an order of magnitude lower than LSMO. This promising property reduces spin independent scattering in the non-magnetic layer. More importantly, LNO is a perovskite structured oxide with very similar lattice parameters as LSMO, which enable the epitaxial growth of the heterostructure.

1.5 Overview of this thesis

The main theme of this thesis is an experimental study on the magnetotransport properties of perovskite oxide heterostructures. The study could not be possible without understanding the properties of single layers constituting the heterostructures. Therefore, the study also included characterization of single oxide layers. This thesis can be divided into two parts. In the first part, readers will be introduced to various topics related to the current project. As mentioned above, a very brief description on magnetoresistance and its relation with spintronics is given in Chapter 1. In Chapter 2, I will introduce half-metallic perovskite manganites from structural, electrical and magnetic points of view. Following that, I will discuss magnetoresistance effects, with an emphasis on GMR, in Chapter 3.

In the second part, focus will be shifted to the core subject of this thesis, which is the experimental study. Chapter 4 presents the experimental methods, including sample preparation by PLD, sample characterization by means of x-ray diffraction, surface morphological, electrical and magnetic characterizations techniques, and device fabrication using photolithographic methods. In Chapter 5, characterization of single-layered perovskite oxides will be shown. Characterizations are divided into two parts, dealing with oxide thin films

prepared by PLD and LMBE. Chapter 6 describes the magnetoresistive effect of all-oxide heterostructure in current-in-plane (CIP) geometry. The results show a combination of magnetoresistance in individual layers in the heterostructure. The last chapter (Chapter 7) on experimental study ends with an analysis of microstructure and hysteresis loops measurements of another all-oxide heterostructure that will be fabricated into current-perpendicular-to-plane (CPP) device in the near future. Chapter 8 finally summarizes the findings.

Chapter 2 Review of the perovskite manganites

2.1 Background

Perovskite manganites ($AMnO_3$ where A=La, Ca, Ba, Sr, Pb, Nd, Pr) have long been studied since 1950s [2.1] by Jonker and Van Santen. The main research interest of manganites arose from the complexity of such correlated electron systems, within which the spin, charge, orbital and lattice degrees of freedom interact simultaneously. In such complicated correlated electron systems, classical independent electrons treatments do not work anymore. These studies of manganites not only provide a protocol for investigations of correlated electron systems, but also give a reexamination of modern condensed matter physics theories [2.2-2.5].

The re-discovery of colossal magnetoresistance (CMR) (will be mentioned in Chapter 3) in manganites in 1990s provoked hopes for developing commercial applications rather than pure scientific interests (for a review see [2.6]). Many devices concepts [2.7-2.12] have been proposed and demonstrated. However, the development of industrial applications based on manganites are still hindered by the large field required for exhibiting CMR effect and their low Curie temperatures, and hence were not adopted so far.

The focus of studies was then shifted to GMR and TMR effect (both will be mentioned in Chapter 3) in multilayered structures partly composed of manganites, based on the half-metallic nature [2.13] of manganites (strictly speaking, $La_{1-x}Ae_xMnO_3$ where Ae=Ca, Sr, Ba). Recent research efforts have also focused on studying magnetoresistance (mostly on TMR [2.14]), as well as the interplay between electronic, magnetic and crystal structures [2.15-2.17] of these lanthanum manganites.

In this Chapter, I will briefly review on the crystal structure, electronic and magnetic properties of perovskite lanthanum manganites and their correlations.

2.2 Crystal structure

The ideal crystal structure of mixed-valence lanthanum manganites is the perovskite structure, as shown in Figure.2.1.(a). The Mn ion (B site ion) at the center of the unit cell is surrounded octahedrally by oxygen ions. La ions or substitute alkanline earth ions (A site ion) such as Sr ions are distributed at the eight corners of the unit cell. However, most of the time, the MnO_6 octahedral is distorted, and hence the perovskite structure is usually orthorhombic. The relations between orthorhombic and ideal cubic perovskite structure is shown in Figure.2.1.(b).

The crystal structure of perovskite lanthanum manganites is governed by a

tolerance factor suggested by Jonker and Van Santen [2.1]:

$$f = (r_{Ae} + r_O) / \sqrt{2}(r_{Mn} + r_O),$$

where Ae is alkaline earth ion, and r_x is the shortest distance between the x (Ae, O, and Mn) ion and the origin. The perovskite structure is stable with *f* between 0.89 and 1.02 [2.1] and *f* = 1 represents the perfect cubic structure. Depending on oxygen stoichiometry and composition content of substitute B-site ion (divalent ion), there are variations in the Mn-O-Mn bond angle. This induces a change from cubic to orthorhombic structure for the manganite unit cells, as mentioned before. In the study of manganites in 1950, Jonker and Van Santen [2.1] further concluded that Curie temperature (T_c) was determined by the Mn-O-Mn bond angle. This bond angle is also closely related to the double exchange mechanism [2.18], which will be discussed in Section.2.4.1. Therefore, it can be seen that the crystalline structures (Mn-O-Mn bond angle) of manganites are intimately related to their electronic (double exchange mechanism) and magnetic properties (Curie temperature).

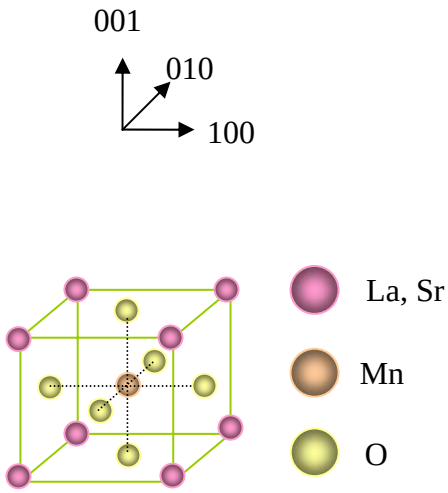

Figure 2.1.(a)

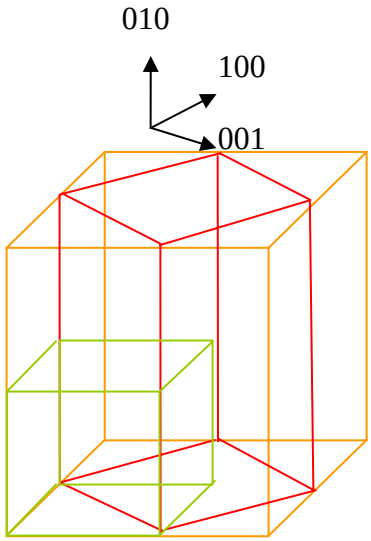

Figure 2.1.(b)

Figure 2-1 (a) Perovskite unit cell of LSMO (b) Orthorhombic (red) and cubic (green) unit cells for perovskite manganites and the relative orientations of the crystallographic axes.

2.3 Electronic structure and properties

2.3.1 Electronic orbitals

The electronic configuration of a neutral manganese atom is $1s^2 2s^2 2p^6 3s^2 3p^6 3d^5 4s^2$. For a Mn^{3+} ion, there are one 3d and two 4s electrons to be lost, and hence the electronic configuration would be $1s^2 2s^2 2p^6 3s^2 3p^6 3d^4$. In contrast to Mn^{3+}, the electronic configuration of Mn^{4+} would be $1s^2 2s^2 2p^6 3s^2 3p^6 3d^3$. The electronic properties of the manganites are mainly due to the interactions between Mn 3d orbitals and the 2p orbitals of neighbouring oxygen ions [2.17]. In the ideal case, the perovskite is cubic and this structure

provides a crystal field [2.19] to split the 3d orbitals into 5-fold degeneracy as shown in Figure.2.4. The 3d orbital levels consist of higher energy e_g doublets and lower energy t_{2g} triplets.

However, as mentioned before, the perovskite unit cells are always distorted, and this kind of distortion is named Jahn-Teller distortion [2.20]. The e_g and t_{2g} of energy levels are further split by this distortion. Jahn-Teller distortion only occurs for Mn^{3+} with one single e_g electron, because the distortion is only energetically favourable when either t_{2g} or e_g energy level is partially occupied.

Electrical conduction in perovskite manganites is mainly carried out by Mn-O-Mn bonds [2.17]. The t_{2g} orbitals rarely overlap with the oxygen 2p orbitals, and the electrons on the t_{2g} orbitals are more localized. On the other hand, the e_g orbitals have a large degree of overlapping with the O-2p orbitals as depicted in Figure.2.2. Figure.2.3 shows the 3-dimensional 3d orbitals in orthorhombic perovskites. The hopping mechanism between Mn e_g orbitals and O 2p orbitals is responsible for electrical conduction in perovskite manganites.

In this section, I have introduced the electrical properties of manganites from charges and orbital point of view.

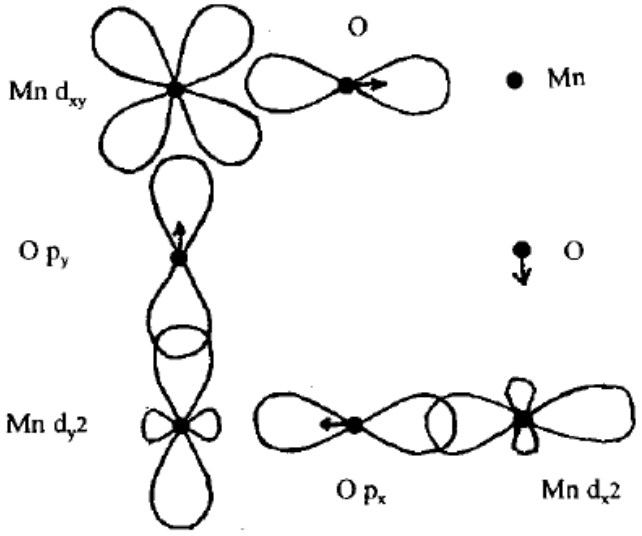

Figure 2-2 Orbital overlap in a plane of the perovskite structure. The t_{2g} d_{xy} orbital overlaps slightly with the O 2p orbital, and the e_g d_x^2 and d_y^2 orbitals have large overlaps with the O 2p orbital. (Taken from [2.21]*)*

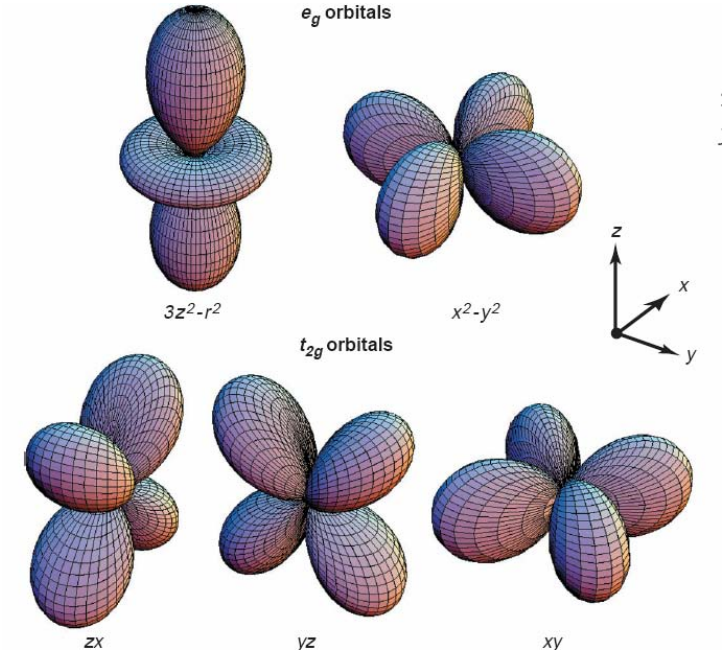

Figure 2-3 The five 3d orbitals, including two e_g orbitals and three t_{2g} orbitals in orthorhombic perovskites. (Taken from [2.17]*)*

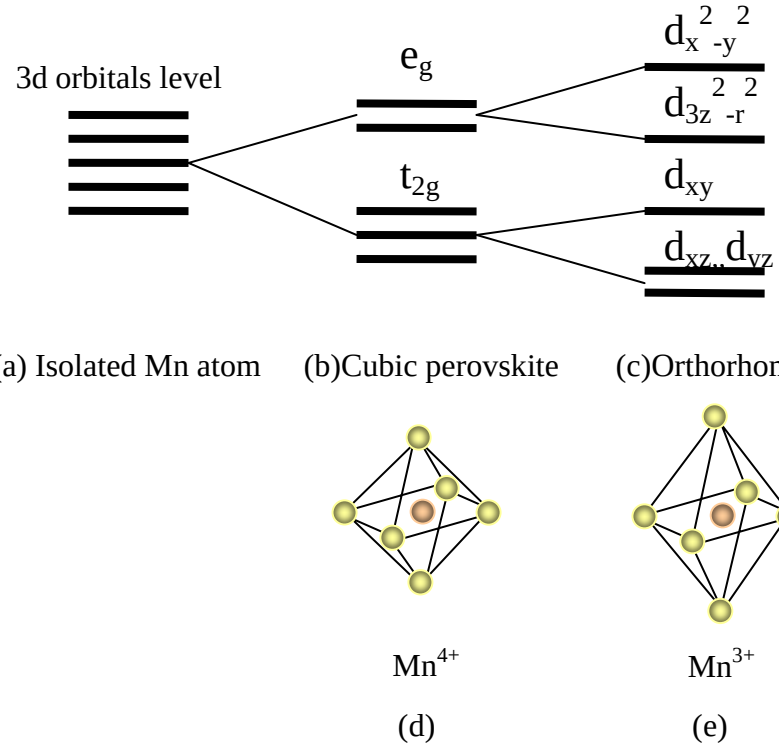

Figure 2-4 A schematic showing the relative energies of the Mn 3d orbitals: (a) Isolated Mn atom, (b) in MnO_6 octahedron, and (c) MnO_6 octahedron after Jahn-Teller distortion. (d) Shape of MnO_6 octahedron with Mn^{4+} and (e) Mn^{3+} ions (the latter one undergoes a Jahn- Teller distortion) (Taken from [2.6]*)*

2.3.2 Anisotropic resistivity

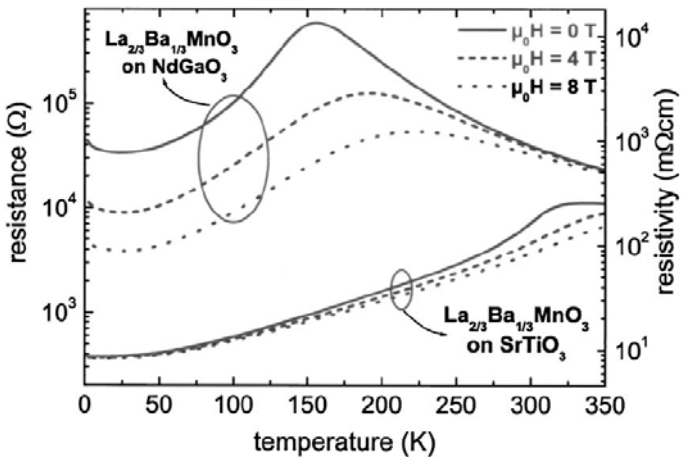

Figure 2-5 Resistance-temperature measurements along in-plane direction for two 68-nm thick $La_{0.66}Ba_{0.33}MO_3$ (LBMO) films grown on (100) STO (strain-free) and (110) $NdGaO_3$ substrates (compressive in-plane strain).Measurements were taken under various external magnetic fields (0, 4,and 8 T). (Taken from [2.22]*)*

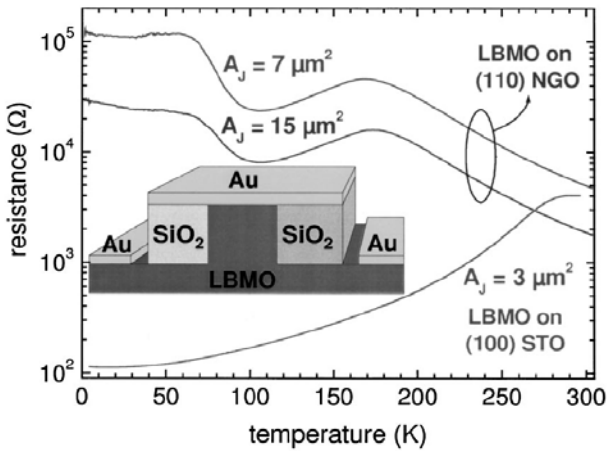

Figure 2-6 Temperature dependence of resistance measured along out-of-plane direction using mesa structures with area A_J, for one LBMO film grown on (100) STO (strain free) and another one on (110) NGO (compressive in-plane strain) substrates. The inset shows a schematic cross-sectional view of the mesa structure. (Taken from [2.22])

Figure.2.5 and Figure.2.6 show the investigations of anisotropic resistivity in manganite thin films by Klein *et al*. [2.22]. They found that barium-doped lanthanum manganite films with compressive in-plane stress exhibited metallic conduction behaviour in plane, and insulating behavior in perpendicular-to-plane direction. This anisotropy, however, was ignored by some authors [2.23, 2.24] who used Van der Pauw method [2.25] for resistivity measurements, a technique which should be applied to homogeneous sample. The resistivity measured in this work employed typical four point probe method, as will be mentioned in Chapter 4.

2.4 Magnetic interactions and properties

In perovskite manganites, magnetic properties are governed by the

interactions between spins of Mn ions. The magnetic properties of the perovskite manganite are interrelated with the electrical properties, which originate from electron transfer between Mn 3d orbitals and O 2p orbitals, as mentioned in the previous section. In the coming sections, two primary magnetic interactions that affect electron transfer in perovskite manganites, double exchange and superexchange interactions, will be discussed .

2.4.1 Double exchange

Zener [2.18] was the first one to propose double exchange mechanism for electrical conduction in manganites. Double exchange starts with a single e_g electron in Mn^{3+} ion, which is transferred from the Mn 3d orbital to an oxygen 2p orbital. Simultaneously, electron transfer occurs from the same oxygen 2p orbital to an empty e_g orbital in an adjacent Mn^{4+} ion. After the transfer of electrons, Mn^{3+} becomes Mn^{4+} and vice versa. The simultaneous transfer of electrons was the reason why it was named “double” exchange.

The transfer parameter t_{ij} for the hopping of an e_g electron from Mn^{3+} to Mn^{4+} ion depends on the relative orientation between adjacent manganese t_{2g} spins .This is summarized in the relation $t_{ij} = t\cos\left(\frac{\theta_{ij}}{2}\right)$,where θ_{ij} is the angle between neighbouring manganese spins. To summarize double exchange

mechanism (Figure.2.7) in a sentence: when the adjacent manganese spins are in parallel state, the probability of hopping by e_g electron along the Mn^{3+}-O-Mn^{4+} bond is maximized, and hence the electrical conductivity should be at its highest value.

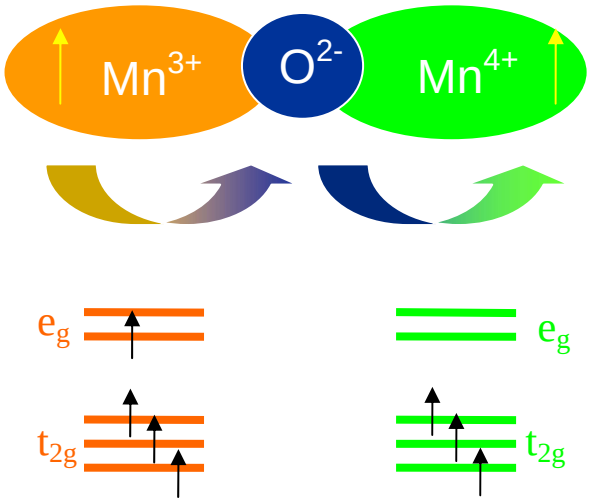

Figure 2-7 A schematic for double exchange mechanism.

2.4.2 Superexchange

In perovskite manganites, superexchange [2.26] describes the magnetic interactions between Mn ions separated by an intervening closed-shell non-magnetic O^{2-} (electronic configuration: $1s^2 2s^2 2p^6$) ion. If the orbitals of two adjacent ions point toward each other, the electron in O 2p orbital will spend part of its time on the empty orbital when one orbital is fully occupied and another orbital is vacant. In manganites, this means that electrons in the fully occupied O 2p orbital can appear on the empty Mn e_g orbital for a certain period of time. The

electron originally in the O 2p orbital is said to be “shared” by O and Mn ions. This kind of electron sharing is the characterisitic of superexchange mechanism.

There is a misconception that superexchange necessarily leads to an antiferromagnetic state. It can also, however, lead to ferromagnetic state. There are three cases of interactions within Mn-O-Mn bond for superexchange mechanism. The cases are Mn^{3+}-O-Mn^{4+}, Mn^{4+}-O-Mn^{4+} and Mn^{3+}-O-Mn^{3+} as shown in Figure.2.8. However, among these three cases, there are only two sorts of transfers of electrons. For Mn^{3+}, one of the e_g orbital is occupied. By Pauli Exclusion Principle, spin of the transferred electron must have opposite orientation with that of the electron in e_g orbital, as the t_{2g} and e_g must have the ferromagnetic alignment of spins by Hund’s coupling. On the other hand, for Mn^{4+}, the transferred electron must have the parallel alignment of spins with the t_{2g} electrons. Finally, it can be clearly shown that Figure.2.8(a) and (b) depict antiferromagnetic coupling while (c) ferromagnetic coupling between Mn^{3+} and Mn^{4+} in superexchange mechanism.

It should be reminded that, superexchange interaction can not only lead to antiferromagnetism but also to ferromagnetism (Figure.2.8) while double exchange can only lead to ferromagnetism. However, in view of electrical property, double exchange always corresponds to metallic state while

superexchange corresponds to insulating state.

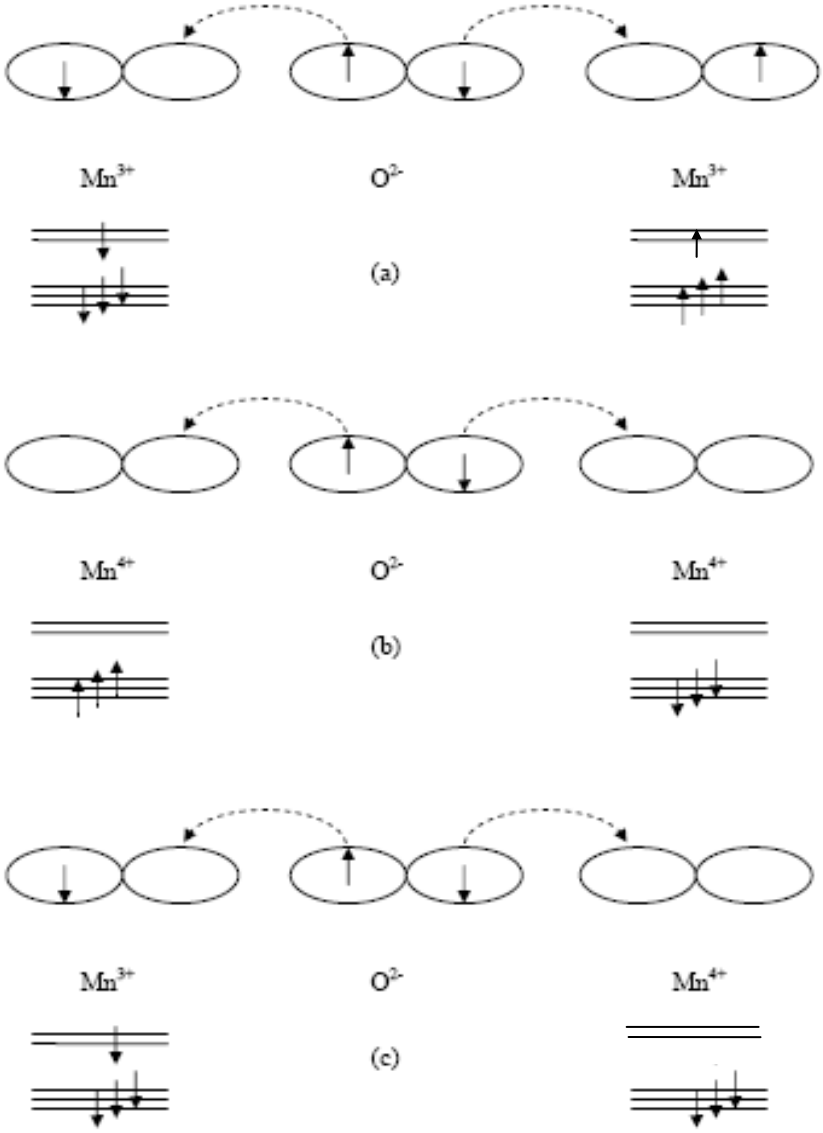

Figure 2-8 Schematic showing the possible cases of the combination of both spin alignment of Mn^{3+} and Mn^{4+} and orbitals involved. (After Ref.[2.27]*).*

2.4.3 Coercivity tuning

This work aims at demonstrating GMR effect in all-oxide PSV structures, in which magnetic materials with marked contrast in coercivity were employed. The study of coercivity tuning in manganite thin films was emphasized in this work.

Since the discovery of GMR, only a few articles [2.28,2.29] reported the presence of GMR effect in all-oxide PSV. In such investigations, two ferromagnetic electrodes of identical compositions and different thicknesses were utilized to achieve coercivity contrast. This approach is limited by, for example, the layer thickness of the spin valve structures.

Various approaches have been examined in order to induce coercivity contrast, such as magnetostatic coupling due to shape anisotropy [2.30], or using different magnetic materials with marked coercivity differences [2.31]. In this work, low level (i.e. doping in small quantities) B-site Ru-doping into LSMO was employed to enhance the coercivity of bare LSMO films. Details of coercivity modification in Ru-doped LSMO thin films were given in Section.1.3.

2.5 Half metallicity in manganites

Other than typical behavior of ferromagnetic metals, manganites also exhibit the unique feature of half metallicity. Half metallic ferromagnet was first suggested in 1983 [2.32]. In half metals, up-spin band and down-spin band are separated, and one of the spin bands is empty. This is different from convectional ferromagnetic metals, in which both up and down spin bands are occupied (Figure.**3**.7). Other than perovskite manganites, double perovskites (e.g. A_2FeMoO_6 ; A = Ca, Sr, Ba) [2.33], CrO_2 [2.34, 2.35], magnetite (e.g.Fe_3O_4)

[2.36] and Heusler alloys [2.37] also exhibit half metallicity and high Curie temperatures (T_C). Theoretically, since one of the spin bands is empty in half metallic materials, electrons that are transmitted through these materials can be 100% spin polarized [2.32, 2.38]. Therefore, half metallic materials can be utilized as perfect spin polarizers.

The first experiment showing the presence of half metallic materials was done by Park and colleagues [2.13] in 1998. In the same year, Soulen *et al.* tried to measure the spin polarization of theoretically proposed half metallic materials [2.39]. The results are summarized in Table.2.1. The percentage values of spin polarization vary with measurement methods. This can be seen from the results (98%) of Park *et al.* as measured by spin resolved photoemission, and the results (78%) from Soulen *et al.* who measured the spin polarization value by superconducting point contacts on LSMO thin films.

In spite of the success in these experimental studies, scientists are still confronting some problems on realizing technological applications with such materials. For example, as for Heusler alloys, the study is still at its infancy because of increased complexity of electronic structure analysis. Detailed review of half metallic materials in both theoretical and experimental aspects can be found elsewhere [2.40, 2.41].

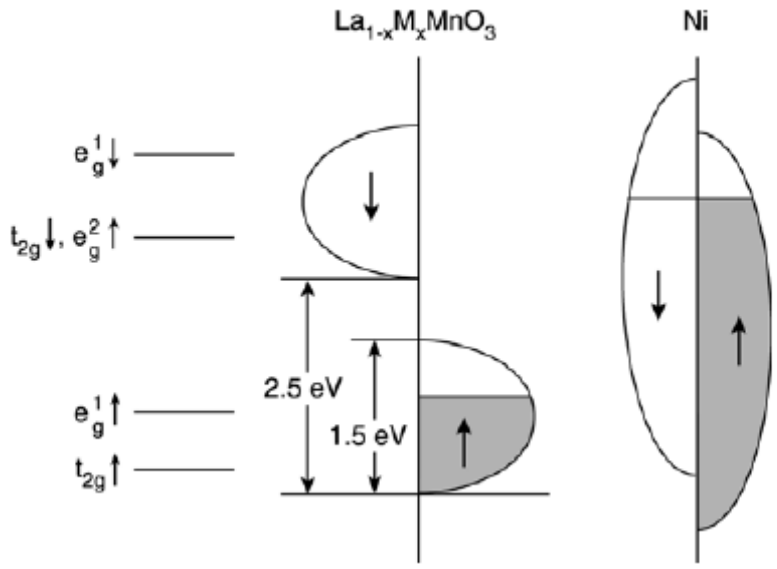

Figure 2-9 Electronic density of states of lanthanum manganites and Ni at T=0K. (After Ref.[2.6]*).*

Ferromagnetic materials	Spin polarization (%)
CrO_2	90
LSMO	78
NiMnSb	58
Ni	~46.5%
Fe	~46
Co	42
NiFe	37

Table 2-1 Spin polarization of some ferromagnetic materials. (After Ref.[2.39]*).*

2.6 Oxygenation of perovskite manganite

Oxygen vacancies are very important in oxide materials. They play crucial roles in determining resistivity, metal-insulator transition temperature T_{IM} and ferromagnetic-paramagnetic transition temperature T_C in manganites. Oxygen vacancies can induce non-stoichiometries in thin films compared with the target materials. During film deposition, there are always interactions between gaseous oxygen and oxygen vacancies, which the reaction rate and direction depends on

the applied oxygen partial pressure:

$$O^{2-} \leftrightarrow \frac{1}{2}O_2 + 2e^- + vacancy$$

When there are vacancies in the thin film lattice, the chemical formula, for example LSMO, is rewritten as $(La^{3+})_{1-x}(Sr^{2+})_x(Mn^{3+})_{1-y}(Mn^{4+})_y(O^{2-})_{3-\delta}$, where δ is the number of oxygen vacancies per formula unit. According to conservation of charges, x, y and δ are interrelated by

$$2\delta = x - y$$

Therefore, the applied oxygen partial pressure affects the number of oxygen vacancies and hence the number of La^{3+}, Sr^{2+}, Mn^{3+} and Mn^{4+} ions in the lattice. The variations of the Mn^{3+} and Mn^{4+} contents play a key role in determining magnetic interactions (as mentioned in section.2.4), and this in turn alters the resistivity, T_C and metallic-semi-conducting transition temperature (T_{IM}) of manganite films.

2.7 Effects of strain and thickness on thin film manganites

Materials	Out-of-plane Lattice constant (Å) (Bulk)	Lattice mismatch with LAO	Lattice mismatch with STO
$SrTiO_3$ (STO)	3.905	N/A	N/A
$LaAlO_3$ (LAO)	3.788	N/A	N/A
$La_{0.7}Sr_{0.3}MnO_3$	3.873	-2.2%	0.8%
$La_{0.7}Ca_{0.3}MnO_3$	3.858	-1.8%	1.20%
$LaNiO_3$	3.84	-1.3%	1.70%

Table 2-2 Lattice parameters of materials and their corresponding lattice mismatches with common substrate materials LAO and STO.

Epitaxial thin films can be successfully grown only if they are prepared on

substrates with well-matched lattice parameters. Table.2.2 summarizes the lattice parameters of some materials used and their lattice mismatch (defined as $\Delta = (Å_{substrate}-Å_{bulk})/Å_{substrate}$) with common substrate materials. Positive lattice mismatches suggest the films being subjected to in-plane tensile strains, whereas negative values represent in-plane strain compressive strains. As mentioned in previous sections, magnetic, electronic and other properties of manganites are partly determined by the electron-lattice interactions (e.g. variations in electron transport properties with different Mn-O-Mn bond angles). Therefore, in-plane strain-induced lattice distortions (Figure.2.10) play a crucial role in deciding the properties of manganites.

Sun *et al* [2.42] have done a systematic study on the effect of substrates and film thicknesses on electron- and magneto-transport properties of LSMO films. Their results showed a typical behavior that resistivity decreases with thicker films on the same kind of substrates. On the other hand, substrate-dependent resistivities of the films were determined by the variations in Mn-O-Mn bond length induced by the strain of substrate, i.e., the shorter the bond length is, the lower the resistivity.

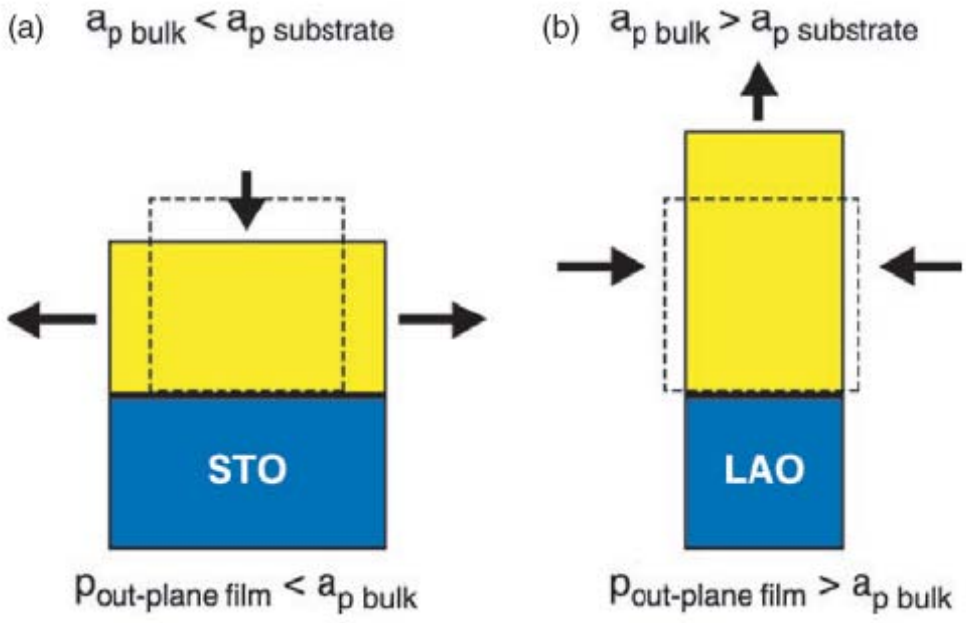

Figure 2-10 The distortion of epitaxy thin film (a) under in-plane tension and (b) in-plane compression. (Taken from [2.6])

Properties such as magnetic anisotropy and coercivity enhancement of strained manganite films were examined in the current study. Other substrate-induced strain effects on manganite films, including magnetic anisotropy [2.43], coercivity tuning [2.44], and surface morphology [2.45] have been investigated by others, which provided clues for explanation of the features exhibited by the films deposited in this work.

In practical situations, the lattice parameters of the films under stress would not be identical along the thickness. As the film thickness increases, the top layers of the film are less influenced by the substrate. This results in the "relaxation" of the film. Overall, there are three kinds of microstructures of an epitaxy film under stress, as illustrated in Figure.2.11. To summarize the points

above, substrate-induced strain is a determining factor for manganite thin film properties.

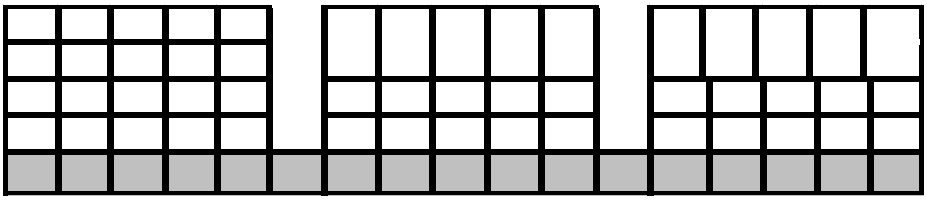

Figure 2-11 Three possible lattices, (a) coherently strained, (b) partially relaxed and (c) fully relaxed of epitaxy thin film under substrate-induced strain.

Chapter 3 Magnetoreistance (MR)

3.1 Background

The magnetoresistive effect (MR) was first observed by Lord Kelvin [3.1] 150 years ago; to be more precise, the phenomenon Lord Kelvin detected was "anisotropic magnetoresistance" (AMR) (Section.3.1.2). However, MR effect was completely ignored until 1950s. Since 1950s, many research efforts have been placed on colossal magnetoresistance (CMR) (which will be mentioned in Section.3.1.3 [3.2, 3.3] However, the large magnetic field required to achieve the resistance change severely limited its applications.

MR once again attracted intensive investigations due to the discovery of GMR [3.4, 3.5] effect (Section.3.2) in 1988. In merely 10 years' time, GMR was employed in read heads of magnetic hard disks (Figure.3.2). On the other hand, TMR (Section.3.1.4) -based devices are gradually replacing their GMR counterparts in various applications. TMR devices generally exhibit larger changes in resistances compared with similar devices based on the GMR effect; its main drawback is the need of depositing very thin insulating layers. GMR (Figure.3.1) or TMR heads are still the mainstream technologies in the production of digital storage devices and such technologies have grown

tremendously recently, as shown in Figure.3.1. Details of these effects will be discussed.

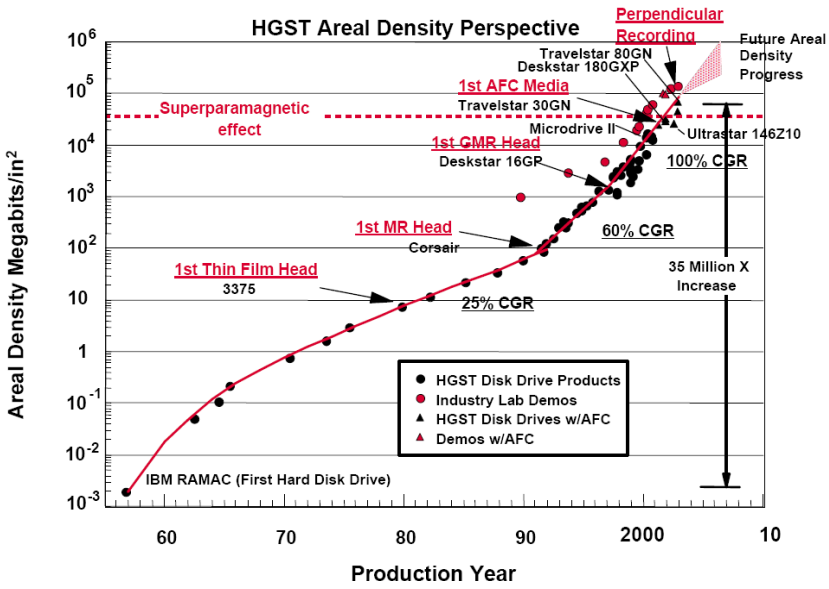

Figure 3-1 Growth of areal density of hard disk drives over years. After ref.[3.6].

Figure 3-2 A hard disk with GMR read head. After ref. [3.7].

3.1.1 Ordinary magnetoresistance (OMR)

Consider a sample with an electric current flowing along the positive x-direction, as shown in Figure.3.3. Once there is a magnetic field applied in the positive z-direction, electrons are deflected (yellow arrow) from their original paths (red arrow) by the Lorentz force acting on them. The electrons travel with

longer paths inside the sample in the presence of the magnetic field, and hence the sample resistance increases. The effect is coined as OMR.

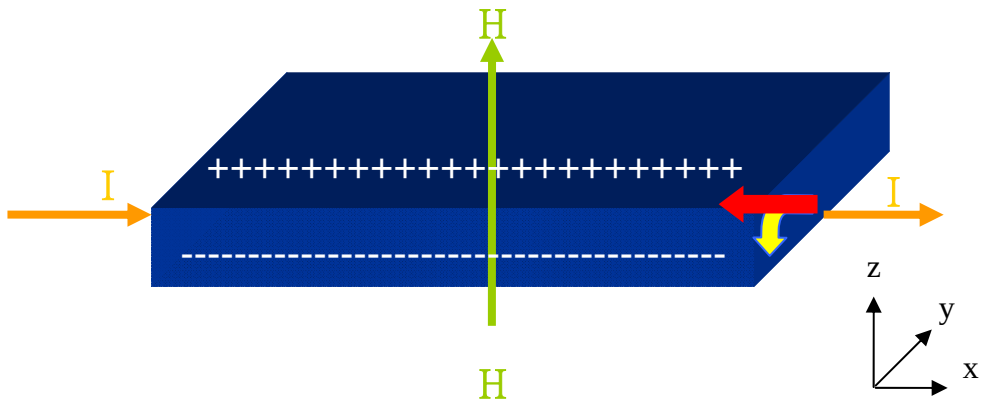

Figure 3-3 Schematic showing OMR effect.

3.1.2 Anisotropic magnetoresistance (AMR)

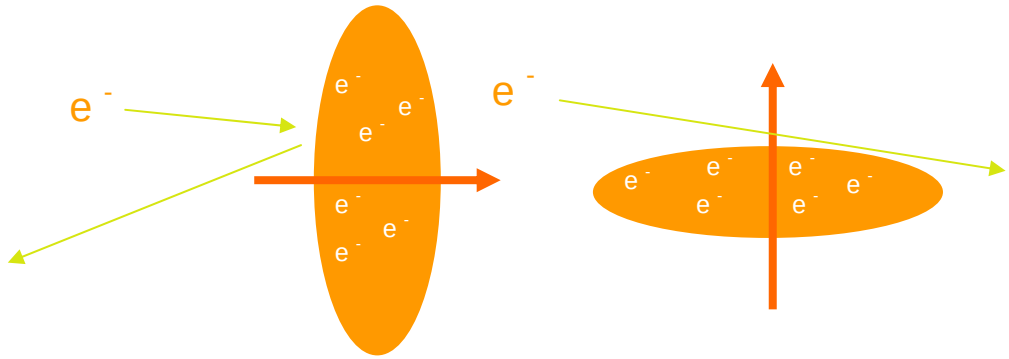

Figure 3-4 Schematic of the AMR effect.

The physical origin of AMR arises from spin-orbit interactions, in which electron clouds around the nuclei deform as the magnetization changes in direction. This deformation changes the amount of electrons to be scattered, thus achieving a change in resistance. As can be seen from Figure.3.4, the sample changes to a high resistance state with an increasing field, when the electric current is parallel to the sample magnetization. On the other hand, a low

resistance state is obtained when the current is perpendicular to the sample magnetization.

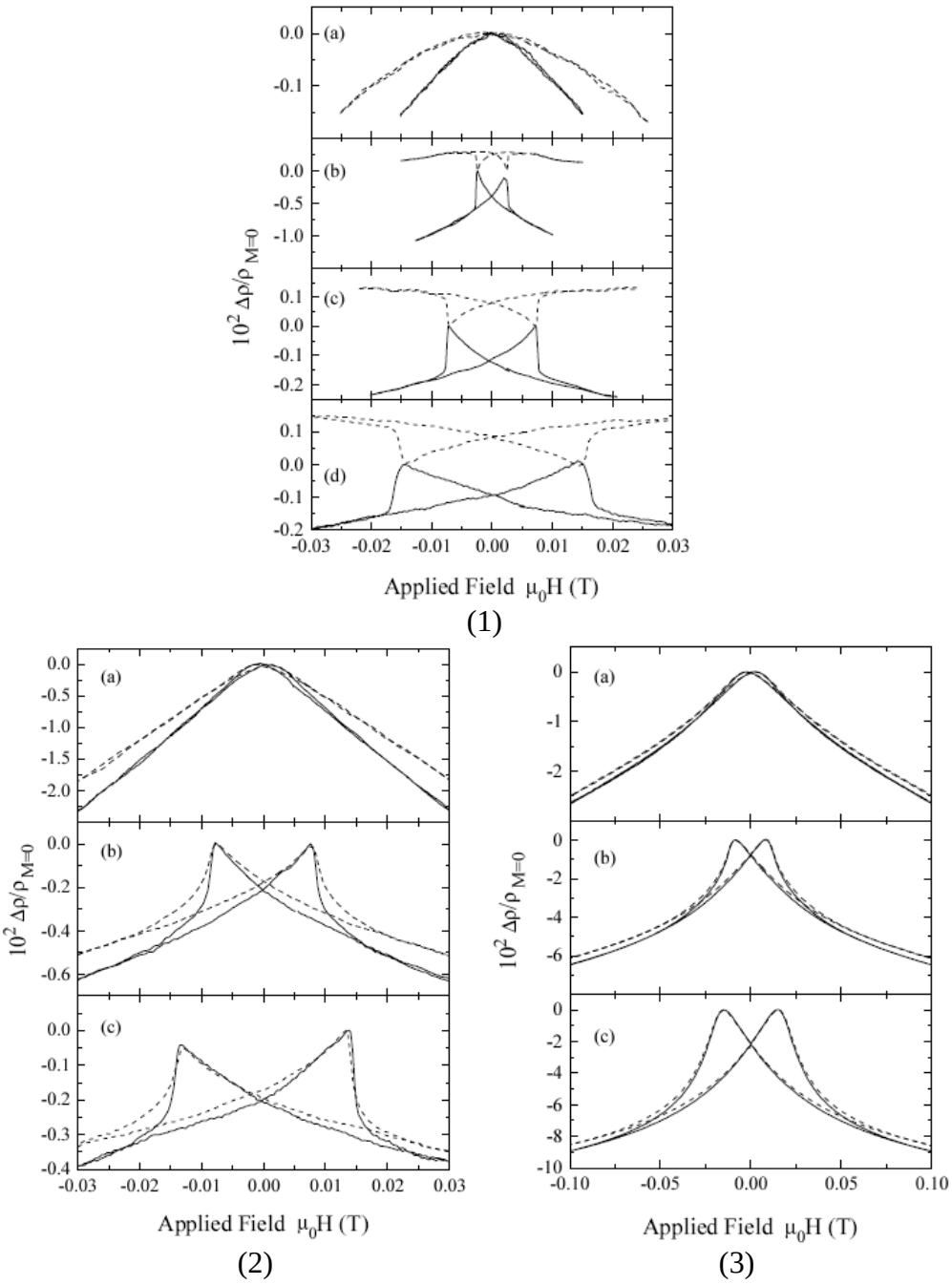

Figure 3-5 In-plane (solid lines) and out-of-plane (dashed lines) magnetoresistance of the post-annealed sample on (1) STO at (a) 285 K, (b) 264 K, (c) 201 K and (d)96 K, the as-grown samples on (2) LAO at (a) 232 K, (b) 159 K and (c) 96 K and (3) Si at (a) 211 K, (b) 159 K and (c) 96 K. (After Ref.[3.8]*.)*

AMR effect of thin films greatly depends on the kind of substrates they are deposited on. Figure.3.5 shows the work by Ziese *et al.* [3.8], who investigated the effect of substrates STO, LAO and Si on the AMR of LCMO. It is clearly shown that as-grown LCMO thin films on LAO and Si did not show AMR effect, as no difference in MR behaviour was observed with measurements made in longitudinal (current parallel to external field) and transverse (current perpendicular to external field) directions. On the other hand, AMR could be observed in post-annealed LCMO thin films on STO and LAO. The work by Ziese *et al.* provides information to my project on the preparation of manganite materials (LCMO and LSMO on LAO and STO substrates).

3.1.3 Colossal magnetoresistance (CMR)

As mentioned before, DE mechanism suggests that the hopping parameter of an electron between Mn ions increases with the degree of parallel alignment of Mn spins. This means when more Mn spins are aligned, the resistance of CMR manganites (with the general formula $RE_{1-x}M_xMnO_3$ (RE= rare earths, M= Ca, Sr, Ba, Pb)) is lowered. The CMR effect actually originates from DE mechanism. With CMR property, some materials can exhibit more than a thousand-fold change in resistance upon the application of an external field. McCormack *et al.* [3.9] reported an MR value of 127000% at 77K with a 6-T field applied to

LCMO thin films. It should also be mentioned that CMR materials attain largest MR around Curie temperatures.

3.1.4 Tunneling magnetoresistance

In a magnetic tunnel junction (MTJ), a very thin (usually several nm) insulating barrier is sandwiched between two ferromagnetic layers. The tunneling electric current depends on the relative orientation of magnetizations in the ferromagnetic layers. TMR originates from the different probabilities of electron tunneling into the (asymmetric) spin sub-bands of the ferromagnets. A detailed theoretical review can be found elsewhere [3.10]. Recently, room temperature MTJ devices with manganites as ferromagnetic electrodes was reported [3.11]. This opens up the possibility of utilizing manganites for high density magnetic storage (harddisk) and magnetic random access memory (MRAM).

3.2 Giant magnetoresistance

3.2.1 Origin of GMR

The GMR effect was first observed separately by the groups of Albert Fert [3.4] and Peter Grunberg [3.5]in 1988, in which the resistance of a magnetic/non-magnetic multilayered structure changes with applied magnetic field. The change in resistance can be more than 100 % [3.11]. The order of MR

strongly depends on the kinds of materials used, the sample structure, and also sample geometry [3.12]. There are four kinds of structure that can exhibit GMR, including magnetic multilayers, PSV, SV and granular structures (Figure.3.6). Currently, the most commonly used structure in industry is the spin valve structure, while pseudo spin valves were prepared in this work for sake of simplicity.

The theory behind GMR is the asymmetric scattering by different spin bands in the ferromagnets. Spins which are parallel to the magnetization are majority spins, while those anitiparallel to the magnetization are minority spins. The asymmetry of majority and minority spin bands in ferromagnets is illustrated in Figure.3.7. This asymmetry or splitting of two spin bands is due to exchange splitting.

Consider the 3d electronic band structures of different materials in Figure.3.7. It should be noted that the sp electrons (which are in 4s and 4p orbitals) are mainly responsible for the conduction in 3d transition ferromagnetic metals (Fe, Co and Ni) and their alloys, because they have high velocities, small density of states and hence long mean free path according to Mott [3.13]. The conductivity of 3d metals depends on the relative position of the Fermi energy to the d bands. After an in-plane field is applied, the majority d spin band of this

ferromagnetic metal (Figure.3.7) e.g. Co, with exchange splitting, is fully occupied. On the other hand, the minority d band is only partially occupied. Therefore, the Fermi level lies on the sp band for majority spin band, whereas still lies on the d band for minority spin. As mentioned before, sp electrons are mainly for conduction in ferromagnetic metals, therefore, the majority spin electrons have higher conductivity compared with that of the minority spin electrons. To conclude, the physical origin of the GMR is ascribed to spin dependent conduction or spin-dependent scattering.

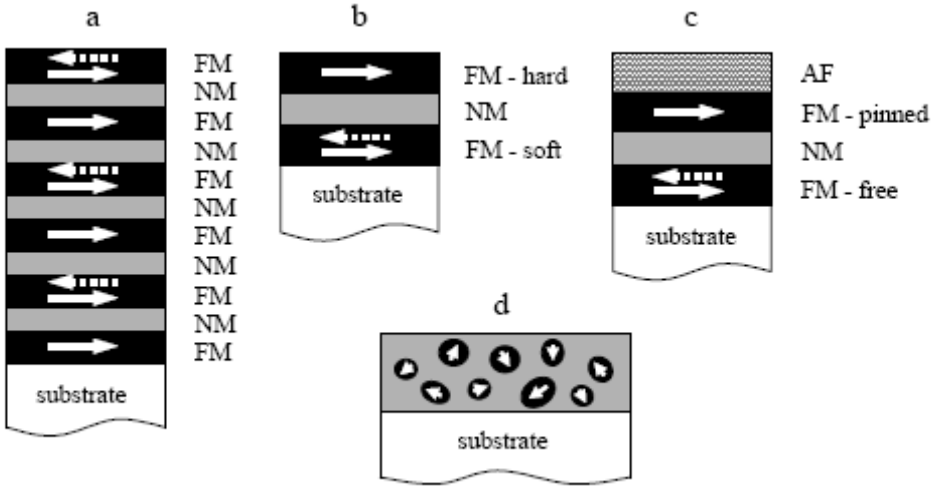

Figure 3-6 Various structures demonstrating GMR effect: (a) magnetic multilayer, (b) PSV, (c) SV and (d) granular thin film. (Taken from Ref.[3.12].)

Consider the PSV structure in Figure 3.8 (a), which consists of three layers of thin films on a substrate. In contrast with MTJ, one conductive layer (rather than an insulating layer) is sandwiched between two ferromagnetic electrodes with different coercivities. The magnetizations of both ferromagnetic

layers are free to rotate. Using the conclusion from the electronic band structures, the trilayer structure achieves a high resistance state (Figure.3.8(b)) when the ferromagnetic layers are in the antiparallel state. This is because both up-spin and down-spin electrons have the same probability to be scattered. On the other hand, the structure has a low resistance value (Figure.3.8(c)) when the majority spin electrons have lower probability of scattering than the minority spins. The complete picture concerning the correlations between magnetization configurations and resistance states can be seen in Figure.3.9.

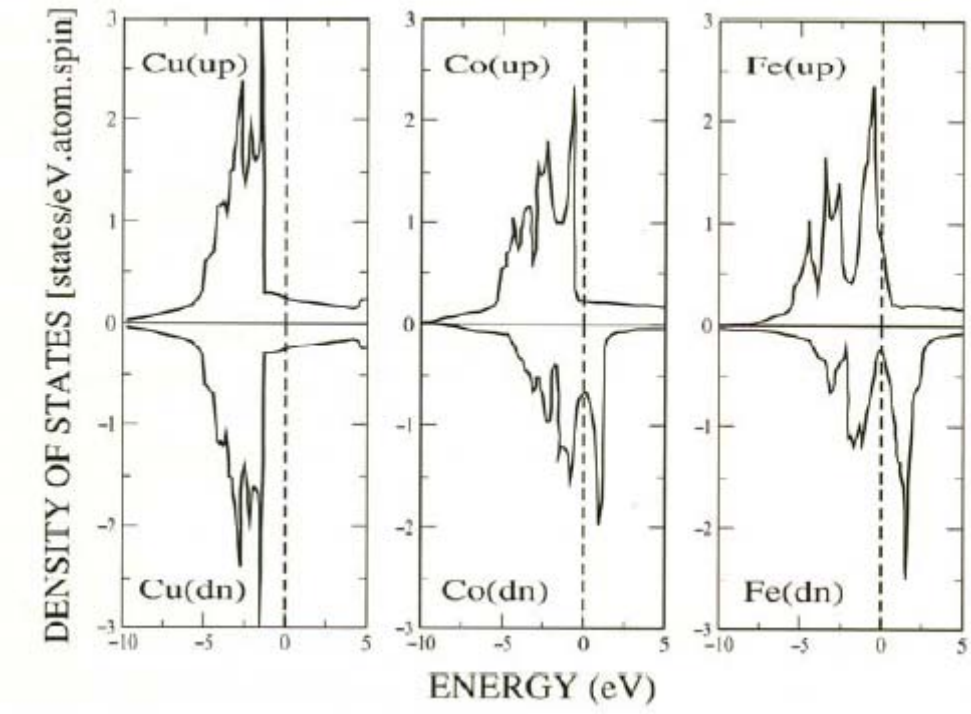

Figure 3-7 Density of states of 3d electron bands in copper, cobalt and iron. Broken line (----) indicates the position of the Fermi level. (After Ref.[3.14]*.)*

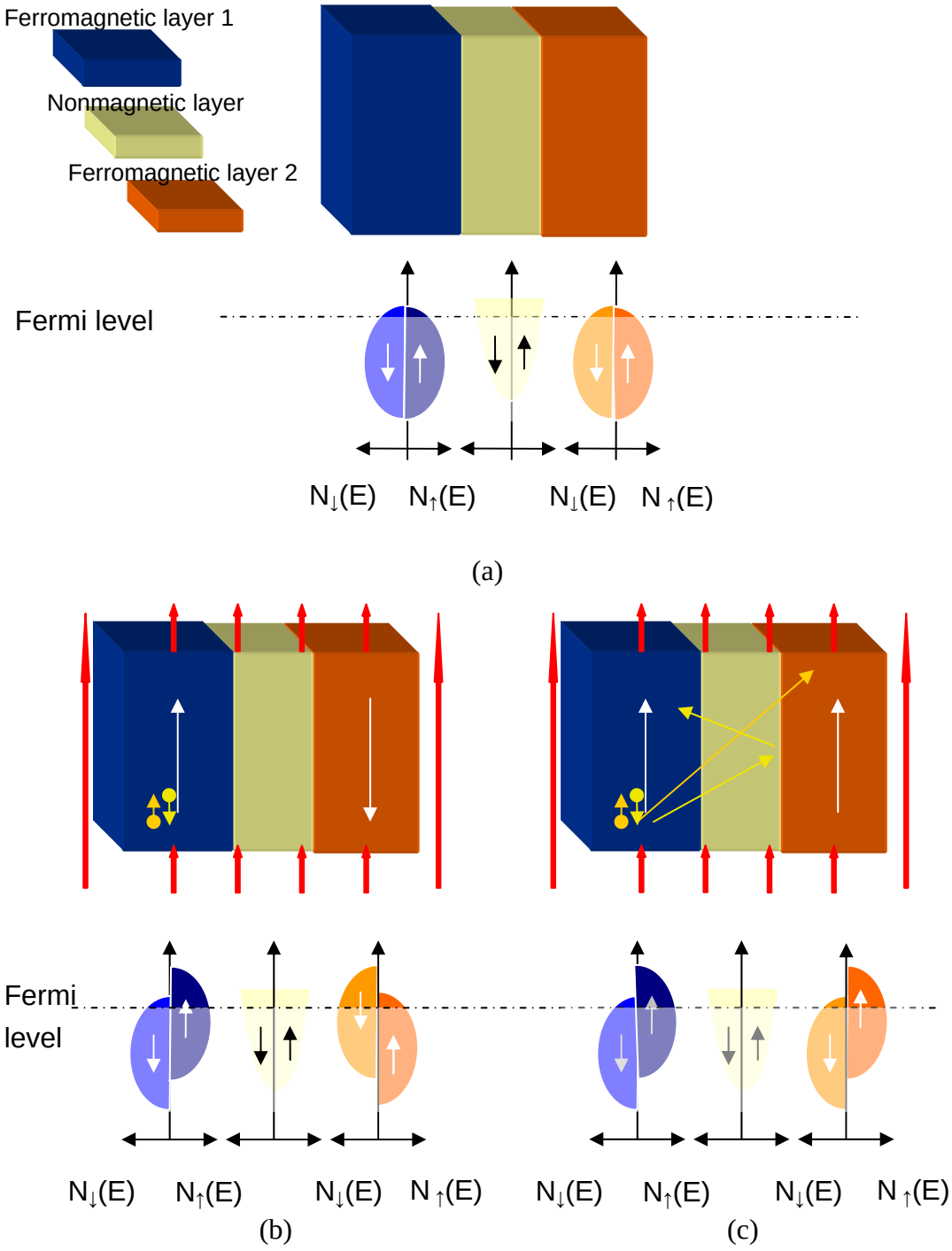

Figure 3-8 Schematic diagram of PSV and the corresponding density of states of different layers when (a) no field is applied (b), it is in the antiparallel state (high resistance state) and (c) it is in the parallel state (low resistance state).

In the coming sections, some parameters influencing the GMR will be reviewed, particularly those related to manganite thin films. A comprehensive

review about GMR in metallic thin films can be found in Ref.[3.15].

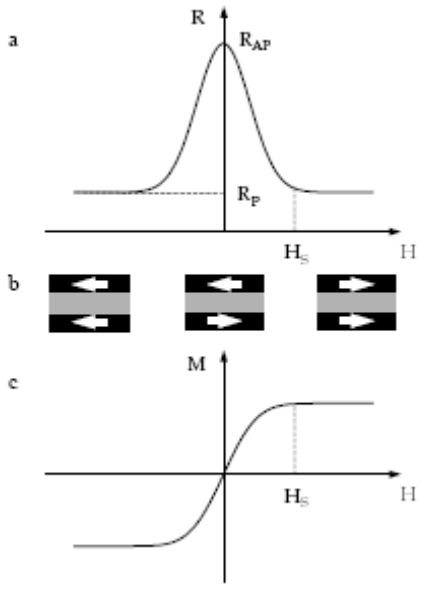

Figure 3-9 Schematic representations of GMR effect from the point of view of (a)magnetoresistive measurement, (b) arrangements of spins in the PSV structure and (c) hysteresis measurement. (After Ref.[3.15].)

3.2.2 Measurement geometry

There are two geometries for conducting MR measurements, which are current-in-plane (CIP) and current-perpendicular-to-plane (CPP), as depicted in Figure.3.10. The CIP configuration is easier to perform by preparing four separated electrodes on the trilayer PSV structure. In contrast, for the CPP geometry, it is necessary to produce a structure that forces the current to flow across the trilayer, which involves complicated fabrication processes. However, the analysis of GMR is simpler in CPP measurement geometry, and the corresponding theories are well developed [3.16]. To date, most GMR-related studies focus on CPP devices, because such devices yield larger MR and

demonstrate current induced magnetization switching as well.

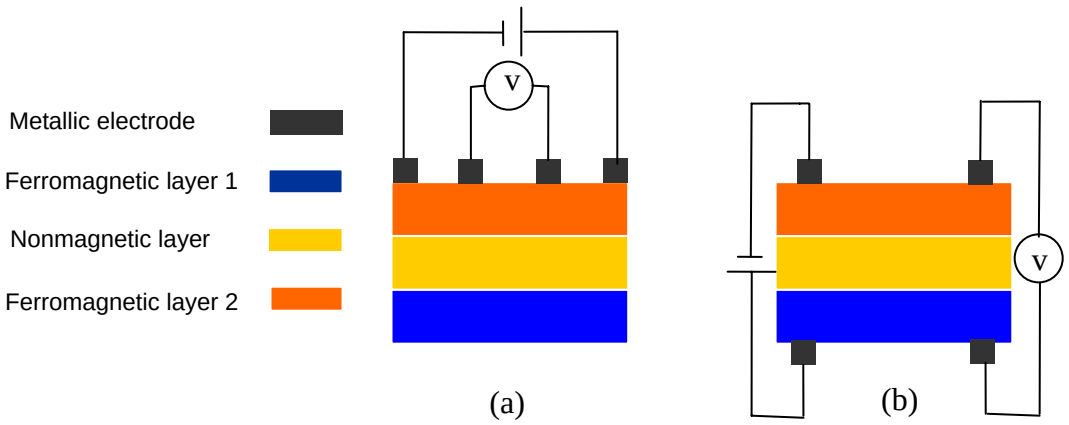

Figure 3-10 Two measurement geometries (a) CIP and (b) CPP of PSV structure.

3.2.3 Dependence on nonmagnetic layer thickness

Choosing the right thickness of nonmagnetic layer in GMR multilayers is more complicated than one can imagine. The non-magnetic layer cannot be much thicker that the electronic mean free path (for CIP device) or spin diffusion length [3.16] (for CPP device), or the GMR effect cannot be observed. It also cannot be too thin to induce interlayer exchange coupling [3.17] (IEC) between two ferromagnetic layers.

Nikolaev *et al.* [3.18-3.20] have done a series of experiments about IEC of all-oxide heterostructures similar to structures investigated in this work, except with very thin nonmagnetic spacers. From Figure.3.11, it shows oscillations of coupling strength with an increase in nonmagnetic layer (spacer) thickness, indicating the alternative changes in ferromagnetic and antiferromagnetic

coupling effect. The authors then tried to simulate the effect with RKKY model [3.21] (a conventional model for IEC), but, experimentally, the decay rate of the coupling strength was faster than the results predicted by the model. Therefore, they suggested that there is a damping coefficient in the RKKY model for explaining the experimental results. As shown in Figure.3.11, the RKKY model with the damping coefficient can successfully demonstrate a quantitative argument with the experiments. The authors further suggested that the damping coefficient resulted from a strong electron scatting in the LNO layer.

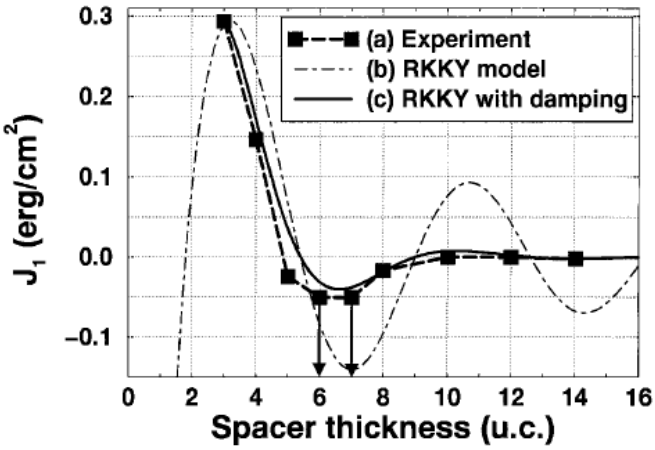

Figure 3-11 Spacer thickness dependence of coupling strength in the $La_{0.67}Ba_{0.33}MnO_3$/LNO/$La_{0.67}Ba_{0.33}MnO_3$/ $La_{0.33}Ca_{0.67}MnO_3$ heterorstructure. After Ref.[3.19].

Figure.3.12 illustrates MH measurements of samples with different spacer thickness, reported by Sirena *et al* [3.22]. The sample with spacer thickness 7 nm displayed double coercivity, showing that the ferromagnetic electrodes were magnetically decoupled. Other samples present typical hysteresis loops strongly influence by IEC. The study suggests clues for choosing suitable spacer

thickness in designing the GMR heterostructures investigated in our work.

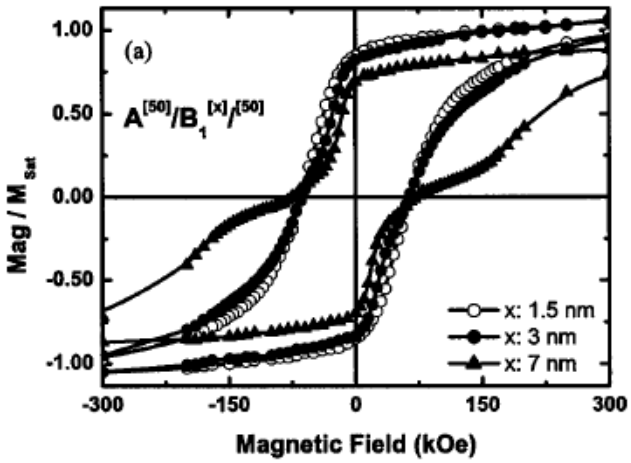

Figure 3-12 hysteresis loops of trilayer samples ($La_{0.55}Sr_{0.45}MnO_3$/STO/$La_{0.55}Sr_{0.45}MnO_3$) with different spacer (STO) thickness. After Ref.[3.22].

3.2.4 Roughness dependence

Surface roughness of individual layers or interface roughness [3.23] in SV structure is another parameter that deserves detailed investigations, as roughness is a determining factor for the properties of GMR in such structure. However, only a few works about the effect of interface roughness on GMR, in all-oxide spin valve structure or multilayer, can be found. A number of experiments about the roughness effect exist for metallic structures, one of which was presented by Fullerton *et al.* [3.24]. With the experimental results of monocrystalline Fe/Cr multilayer, they revealed that spin-dependent scattering at the interfaces can be enhanced by roughness. The same group also investigated the relations on polycrystalline Fe/Cr multilayer [3.25], but the results obtained was in contrary

to that of monocrystalline samples, showing that interface roughness could reduce GMR effect. These two articles suggested that spin-dependent scattering is very sensitive to the structure of interfaces.

If roughness at interfaces increases to a certain extent, pinhole [3.26] may occur and this can leads to a reduction in GMR. Pinholes (Figure.3.13) could have two effects on SV structure: (1) inducing magnetic coupling between two ferromagnetic electrodes when they are in direct contact, and (2) current "leaks" at pinhole can degrade GMR.

Figure 3-13 Schematic for the formation of pinhole in PSV structure

Most studies [3.26-3.28] on pinhole effect focused on the structure that exhibit TMR instead of GMR when the commercial magnetic recording heads employ TMR. Although the two transport mechanisms are totally different, insightful ideas can be obtained from such investigations. In this work, study of roughness of single layer manganite thin films will be presented in Chapter 5.

Chapter 4 Experimental Methods

4.1 Target fabrication

Material	Calcination	Sintering
LSMO	1100°C (10 hr) and 1200°C (10 hr)	1320°C (10 hr)
LNSMO	1100°C (10 hr) and 1200°C (10 hr)	1350°C (20 hr)
LSMRO	900°C (10 hr)	1400°C (10 hr)
LCMO	900°C (10 hr)	1400°C (10 hr)
LNO	900°C (2 hr)	1200°C (10 hr)

Table 4-1 Calcination and sintering temperatures of various targets.

Targets for PLD were synthesized using conventional solid-state-reaction methods. The LSMO target, for example, was fabricated by using starting materials of La_2O_3, $SrCO_3$, MnO_2 powders. The powders (especially for La_2O_3 and MnO_2) were first separately dehydrated at 100 °C for at least 2 hours in air. After dehydration, they were mixed at appropriate weight ratios and ball-milled for 6 hours. Stoichiometric mixture of powders were ground and reacted at 1100 °C for 10 hours and then calcinated at 1200 ^{o}C for 10 hours. The calcinated powders were ground into fine powder and pressed into a circular pellet by an oil compressor, using a force of 5 Tons. The pellet was then finally sintered at 1320 °C for 10 hours. Details of synthesis temperatures of different targets are listed in Table 4.1.

The as-prepared target was structurally characterized by XRD and compositionally by EDX.

4.2 Thin film processing

4.2.1 Substrate preparation

Commercial LAO (100), STO (100) and STO (110) (from CrysTec GmbH, Berlin, Germany and Hefei Kejing Materials Technology Co Ltd., Hefei, China) were used in this study. One side of each substrate was epi-polished. The substrates were cleaned with acetone and then ethanol in an ultrasonic bath for at least 5 minutes and then dried with compressed air before loading into the deposition chamber.

4.2.2 Pulsed laser deposition (PLD) method

Figure.4.1 shows the schematic of the PLD system used in this project. The vacuum chamber is attached with a digital pressure gauge, a rotary pump, a fused silica glass window, substrate and target holders.

Thin film deposition procedure is as follows. Cleaned substrates were fixed at the substrate holder with silver paste. Targets were fixed mechanically by screw and the target holder was set to rotate during deposition. Such a procedure reduced the possibility for leaving a deep trench on the target by the laser beam. The chamber was then pumped for about 45 minutes down to a base pressure of 1-10 mTorr. Subsequently, the substrate holder was heated up to a certain

temperature (optimal deposition conditions will be given in Chapter 5), and the chamber was filled with oxygen at 150 mTorr.

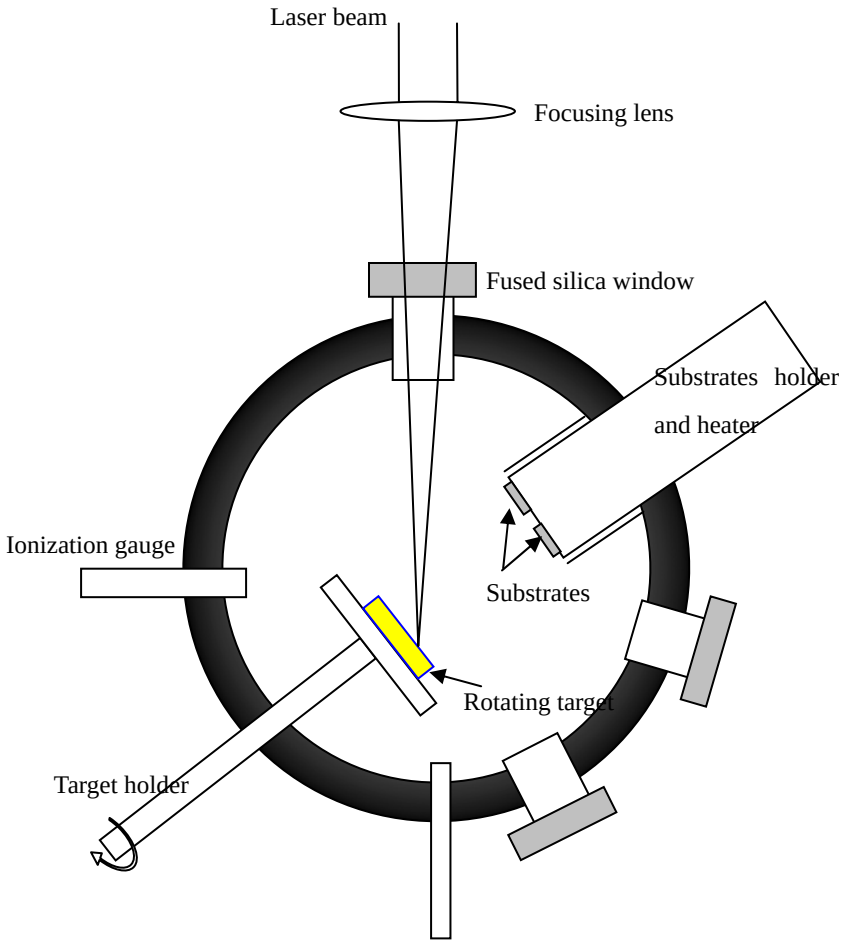

Figure. 4-1 Schematic diagram of PLD system for thin film deposition.

Afterwards, a Lambda Physik KrF excimer laser (λ = 248 nm) was used to fire laser pulses at a frequency of 5 Hz unless specified. The laser pulses were focused by a lens with a focal length of 30 cm and then transmitted through a fused silica glass window. The pulse energy was set to about 200 mJ (unless specified otherwise) for the smoothness of film surfaces. The focused laser beam struck onto the rotating target with a spot area of 1 mm^2. The energetic focused laser beam vaporized the target material and produced a plume of target species.

Particle of the target species finally fell on the substrate to form a thin film. After deposition, the heater was cooled down at a rate of about 0.16 ^{o}C/s to room temperature and then turned off.

4.2.3 Deposition of heterostructures by laser molecular beam epitaxy (LMBE)

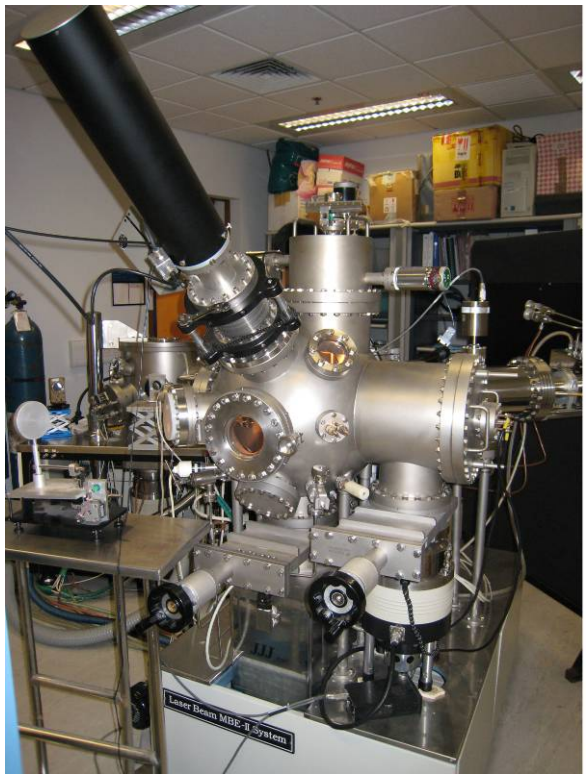

Figure 4-2 Laser Beam MBE-II system

The laser molecular beam epitaxy II system is shown in Figure.4.2. The system consists of a main chamber, separated from a load-lock chamber by a gate valve. It is equipped with a reflection high energy electron diffraction (RHEED) [4.1] system for monitoring the growth of epitaxial thin films in situ. A nanocluster beam source (NC200U Oxford Applied Research) [4.2] allows the

deposition of nanoclusters.

In the system, a turbomolecular pump is used to evacuate the system down to 10^{-8} Torr. If higher vacuum is required, the chamber is able to be further pumped down to 10^{-9} Torr by a LH-3 ion sputter pump. In order to maintain a high vacuum (10^{-8} Torr) in the main chamber, a load-lock chamber was used as a "buffer", which connected the main chamber to the ambient. For example, when substrates or targets are to be placed inside the main chamber, they are positioned onto the transfer arm in the load-lock chamber. The load-lock chamber is then evacuated to 10^{-6} Torr by a turbomolecular pump. The degree of vacuum is not greatly deteriorated after the gate valve is opened. This is because the pressure difference between the load-lock (10^{-6} Torr) and the main chamber (10^{-7}-10^{-8} Torr) is not large. Through the transfer arm, a maximum of four targes can be placed on the targets holders separted by 90^{o}. *In-situ* deposition of multilayers without breaking the vacuum is therefore feasible.

For removing any foreign materials on the target surfaces, the rotating targets were pre-ablated for 100 pulses. The substrate temperature was elevated to 600-800 ^{o}C, estimated by using an infra-red pyrometer. The substrate holder was set to rotate in order to obtain thin films with a high degree of thickness uniformity. Ambient oxygen of 150-190 mTorr, with a flow rate of 20 standard

cubic centimeters per minute (sccm), was maintained during deposition. In order to achieve such a high oxygen pressure, the gate valve separating the inner chamber from the molecular pump, was half-closed. This certainly lowered the efficiency of evacuation, and the base pressure was increased from 10^{-8} Torr to 10^{-5} Torr. All of the conditions were stabilized for 10 mins before deposition.

The laser (Lambda Physik KrF excimer laser with wavelength of 248 nm) used in LMBE-II was of the same model as the one in PLD system. The laser beam energy was set to roughly 250 mJ at a frequency of 5 Hz. The laser fluence was about 3-5 J/cm^2. For deposition of a thin film of 80 nm, the deposition time was about 10 mins. The actual film thickness was determined by cross-sectional SEM, as discussed in Section 4.3.1.1 below.

4.2.4 Device fabrication

4.2.4.1 UV photolithography

A two-step UV photolithography process was employed for the fabrication of CIP devices. Two masks were designed by using AutoCAD^{TM}, for producing a track of 100 μm in width with four electrodes on top. The fabrication process, as shown in Figure.4.3, included conventional UV photolithography, argon ion milling, Pt metallization and lift-off.

The process of photolithography was carried out in a class-1000 cleanroom in the Department of Applied Physics. After the deposition of trilayer structure, a 3-μm thick AZ 5214 E photoresist layer was spin-coated on the sample at 4000 revolutions per minute (rpm) for 60 seconds. The sample was then baked inside an oven at 95 ^{o}C for 1 minute. This was followed by illumination of UV light (Figure.4.3 (a)) with a power density of 24 mW/cm^2 though a chrome mask for 15 seconds. AZ 5214 E could be positive and negative photoresist under specific heat treatment; in this experiment, it was used as a positive resist. Photoresist at regions illuminated by UV light was removed by immersing the samples in a beaker of developer for 40 seconds. The desired pattern was finally transferred (Figure.4.3 (b)) from the mask to the photoresist layer.

The next step was to (Figure.4.3 (c)) etch the trilayer by bombardment of Ar-ions. In an ion miller, an Ar-ion source was set at 5 keV, and the etching beam current was about 100 μA. Etching a 100-nm thick trilayer structure required 30 minutes of time. Such an etching process removed the uncovered trilayer structure (Figure.4.3 (d)) down to the surface of the substrate. The surfaces of STO and LAO substrates, after etching, became oxygen-deficienct at high temperature in vacuum and hence they were conducting. Therefore, the samples were left in air for at least 24 hours to allow the surface to “recover” from

deoxygenation before the next photolithography step.

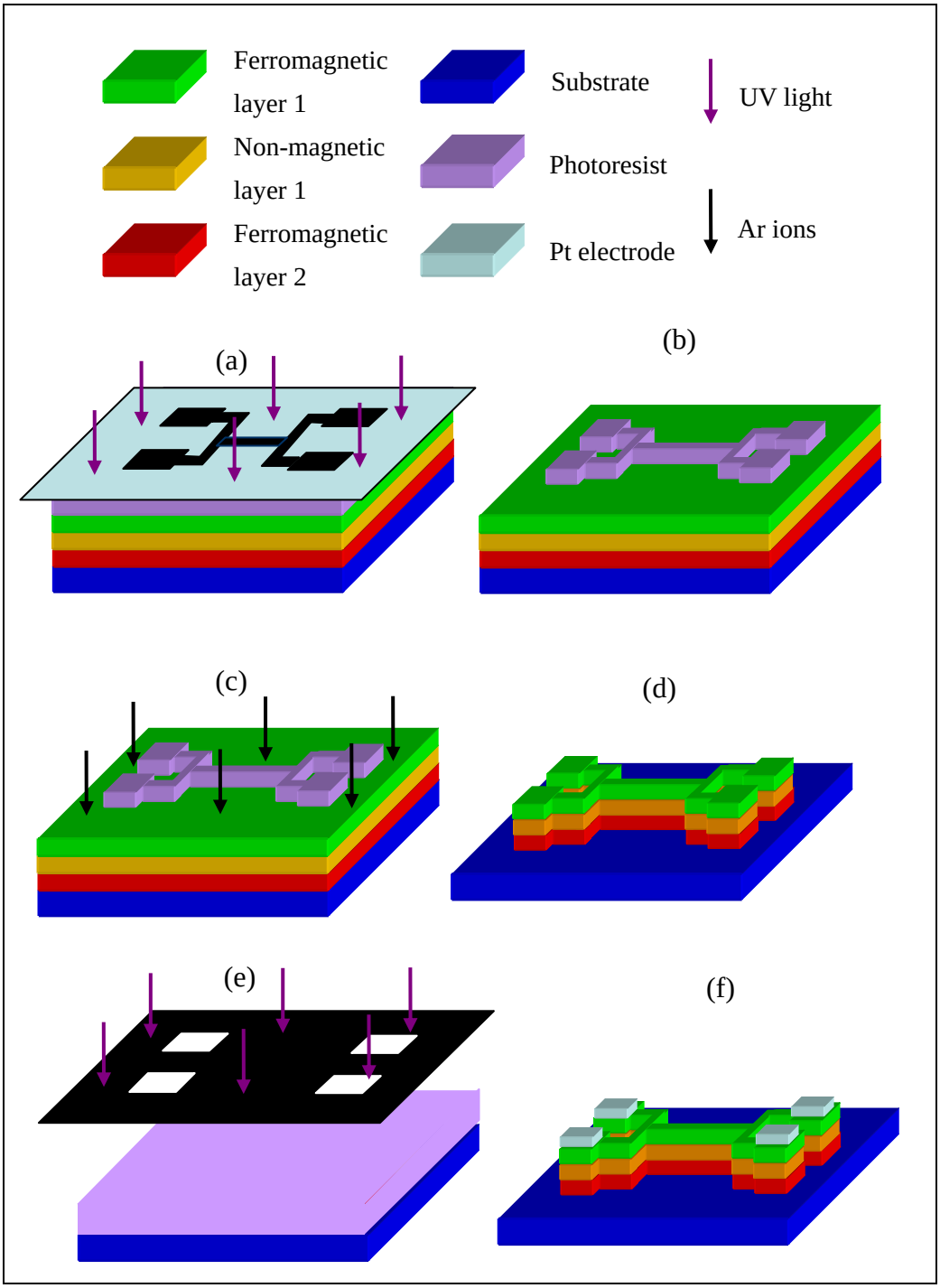

Figure 4-3 UV-lithography steps for fabricating a CIP device. Details of procedures are described in text.

In the second photolithography step, a different photomask (Figure.4.3 (e)) was used for the preparation of top eletrodes. Pt layer of 100 nm thick was

deposited (Figure.4.3 (f)) on the surface of the sample (with patterned resist) by PLD. In the final step, by placing the sample into acetone for about 2 hours (lift-off), four electrodes were remained on the pads and a CIP device was fabricated.

4.3 Characterization methods

4.3.1 Structural characterization and surface morphology

4.3.1.1 X-ray diffraction (XRD)

XRD provides crystal structure information of thin films and bulk samples. Using a Bruker D8 Discover x-ray diffractometer, measurement including θ-2θ scans, rocking curves (or ω-scans) and phi (ϕ) scans were conducted in this project. The schematic of x-ray measurement is shown in Figure.4.4.

As for θ-2θ scans, Bragg's law states that:

$$n\lambda = 2D\sin\theta, n = 1,2,3..., \qquad (4.1)$$

where D is the inter-planar distance, λ the wavelength of x-ray radiation, and θ the angle at which the incident rays illuminates the sample, was used to determine the lattice parameters. From the results, angle θ was measured, and hence lattice parameter a, b, c could be obtained by using Equation.4.1 when λ is known as 1.541 Å (Cu K_α radiation). In my case, the structures of materials were

all cubic or pseudo-cubic and therefore $a = b \approx c$.

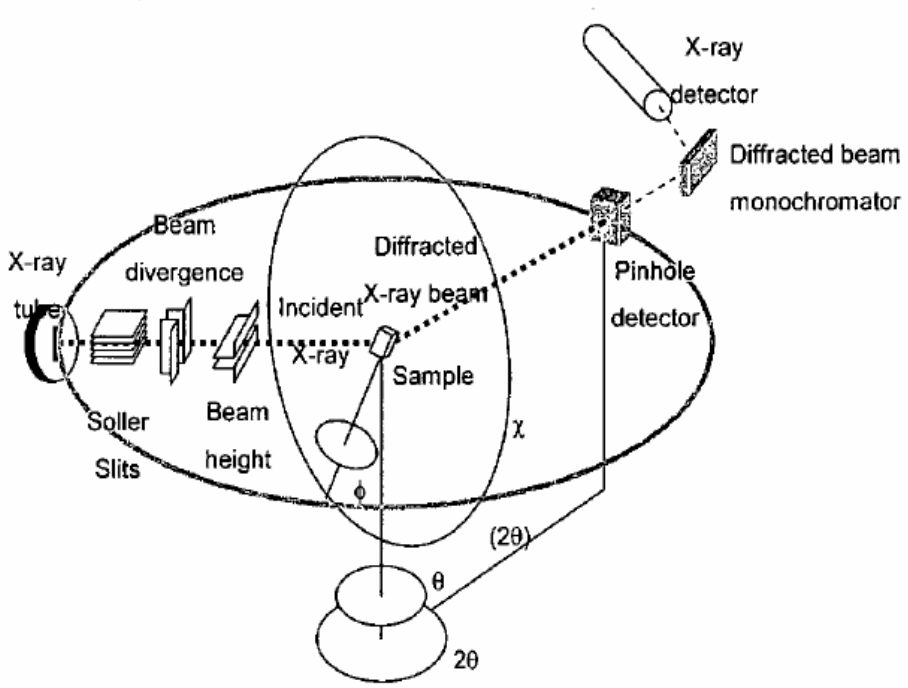

Figure 4-4 Diagram depicting the experimental geometry of X-ray diffractometer. There are slits, x-ray tube, photo-detector and four primary axis of gonimeter

After lattice parameters were obtained, the degree of crystallinity of the films could be determined by rocking curve measurements. In the measurements, the x-ray source and the detector were fixed at angles corresponding to a specific atomic plane spacing, while the sample was rocked about ω-axis (Figure.4.5). The tilting of the grains' atomic planes from the ω-axis can be detected by such scans, hence determining the degree of crystallinity of the film. Quantitatively, the full-width at half-maximum (FWHM) values of the rocking curves were used to compare the degree of crystallinities among samples (e.g. 0.5^{o} for LSMO and 0.1^{o} for LAO single crystalline substrate)

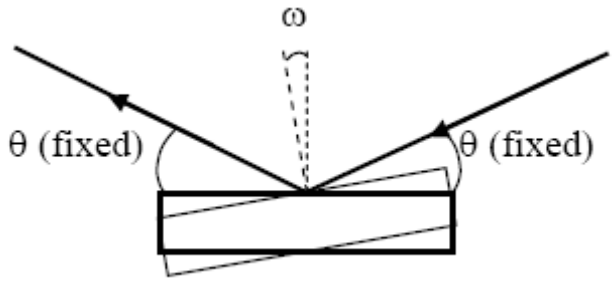

Figure 4-5 Schematics describing the geometry of ω-scan.

Regarding the ϕ-scans, since the crystal structure and orientations of single crystalline substrates were pseudocubic (001), the source and the detector were maintained at constant values corresponding to (002) planes of the substrates during the scans. The samples were then tilted along the χ-axis by 45°, followed by 360° ϕ-scans. For cubic structures, the scans demonstrated four peaks of $(20\bar{2})$, $(\bar{2}0\bar{2})$, $(\bar{2}02)$, and (202) planes separated by 90°, showing a four-fold symmetry of the lattice. For ϕ-scan mentioned below, it should be reminded that the samples were still maintained at 45° of χ angle.

In the ϕ-scan, the important thing to note is that if the measured thin films were *truly* cubic, the ϕ-scans of the films could be done by fixing the source and the detector at the angles of (202) planes of the films, which were calculated from the 2θ values of (200) planes in the θ-2θ scans.

However, most of the thin films were pseudo-cubic and hence the calculated 2θ values of (202) planes were somewhat different from the ideal values. Therefore, ϕ-scans with four peaks were hardly observable for the films because

the detector and the source were fixed at incorrect angles. For improving this situation, θ-2θ scans for obtaining correct θ values of (202) planes of the films would be used to allow easier observation of four peaks in ϕ-scans. By setting ϕ angle as one of the four peak values obtained from the substrate's ϕ-scan, θ-2θ scan at that particular ϕ angle showed a peak corresponding to (202) plane of each film. That peak value was finally the true and correct value for the ϕ scan of the films.

4.3.1.2 Atomic force microscopy (AFM)

AFM is a non-destructive technique to study the surface morphology of the film surfaces. One of the advantages of AFM is that the images grasped have a high correspondence with the actual film surface topologies. Therefore, the image can give very useful quantitative information such as surface roughness.

When investigating the sample surface, tapping-mode AFM (NanoScope IV, Digital Instruments)was used. In the tapping mode, the AFM probe was set to vibrate at a constant frequency (Hz) and scanned across the sample surface during profiling. When the probe came close to the surface of the sample, the probe was deflected. This deflection was detected by the variations on the positions of photodiode through a laser beam. The data obtained were then converted to a three dimensional surface profile of the sample.

4.3.1.3 Cross sectional scanning electron microscopy (SEM)

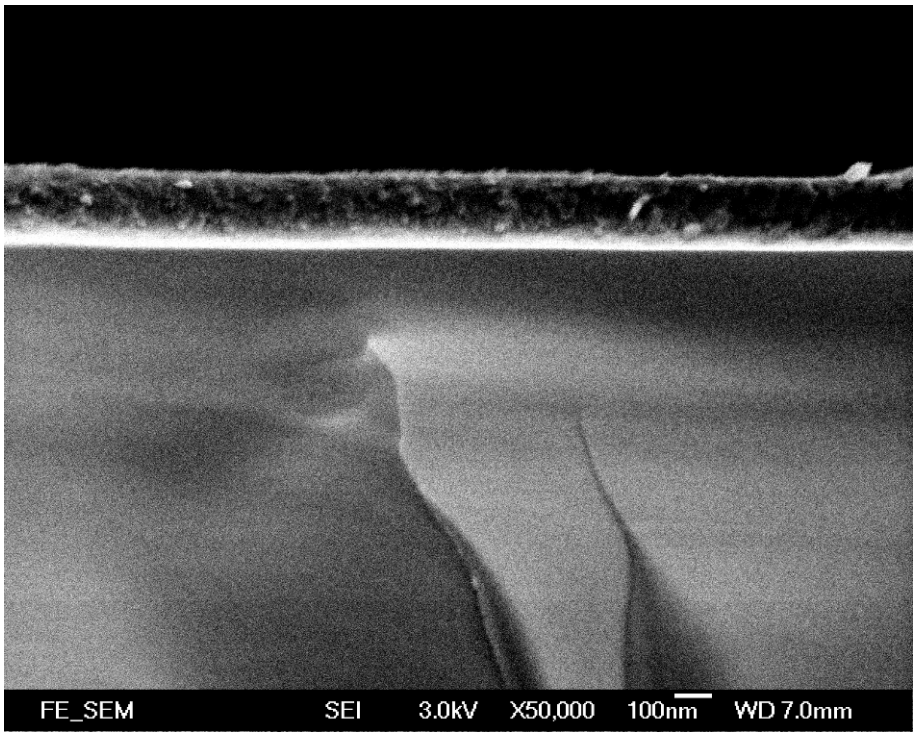

Figure 4-6 Cross-sectional image of a layer of thin film, with thickness about 200 nm, on a substrate.

SEM is a conventional technique to image surfaces of samples, either in thin films or in bulk form. The primary purpose of using SEM in this work was to calibrate the film deposition rate in our systems. In this work, a field emission SEM (FESEM) (JEOL JSM-6335F) was used to obtain cross-sectional images of the films with high resolution. FESEM provides narrower electron beams than convectional SEM, because electrons are generated by a field emission source with a tungsten wire fashioned into a sharp point subjected to a high electric field (~6 KV). Therefore, an image with high spatial resolution can be obtained. A

cross-sectional SEM image, showing a layer of LSMO thin film on LAO substrate, is displayed in Figure 4.6.

4.3.2 Composition characterization

4.3.2.1 SEM energy dispersive x-ray (EDX)

The SEM system used in this work is accompanied by an energy dispersive x-ray (EDX) system, and it was used for compositional characterization of bulk targets used for PLD.

When a specimen is excited by electron bombardment, some of atoms of the specimen are ionized, by transition of K-shell electrons into vacuum. Since there is a hole in the K-shell, there is a certain probability for the upper shell electrons to fill up the gap, resulting in a release of energy in form of a photon (x-ray) with definite energy. The energies of photons released from different elements are different, because of the unique energy levels between shells given by the specific atomic structure of an element. Hence, the composition of the specimen can be obtained by analyzing the x-rays detected by EDX.

4.3.3 Magnetic characterization and electrical transport measurements

4.3.3.1 Vibrating sample magnetometry (VSM)

This section gives a brief introduction to the operation of VSM, which was first invented by Foner [4.3, 4.4] in 1950s. VSM is a commonly used technique to measure magnetic response of a sample against the applied magnetic field. The schematic of a VSM is shown in Figure.4.7.

The simplest form of VSM comprises of a electromagnet, a vibrating stage, pick-up coils and a rod for attaching samples. A sample vibrating vertically at a specific frequency is placed between the poles of the electromagnet. With the application of a uniform magnetic field, a signal in form of an induced voltage is generated in the pickup coils according to Faraday's law, due to the presence of the oscillating magnetic flux from the sample. By comparing the induced voltage against that arising from a reference sample (with known magnetization), magnetic moments of other samples can be obtained. On the basis of the working principle of VSM, other magnetometers [4.5, 4.6] have been developed to investigate the specific magnetic properties.

A Lakeshore 7407 system, with a sensitivity down to the range of μemu (for

room temperature measurements) was utilized in this work. The system provides a cryogenic option for low temperature measurements, using a continuous-flow cryostat (model 74018). Measurements can be performed at temperatures ranging from 4.2 to 450 K, if liquid helium is used for cooling the samples. In this study, only liquid nitrogen was used, and the lowest temperature for measurements was 77K.

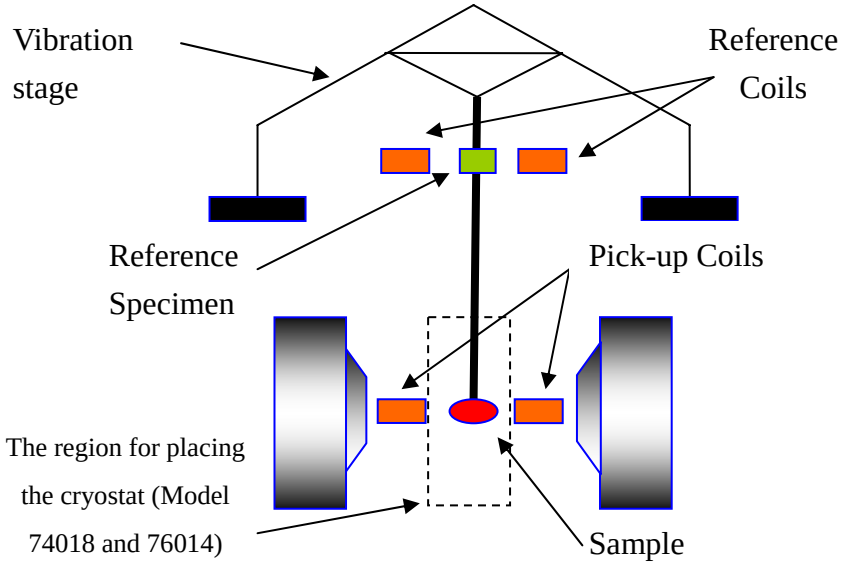

Figure 4-7 Schematic of a VSM. (After Ref.[4.4])

The model 74018 cryostat is displayed in Figure.4.8. It was first positioned within the electromagnet, as shown in Figure.4.7. Before measurements, the vacuum jacket was pumped down to 20 mTorr for about 30 minutes by a rotary pump. This was then followed by the introduction of liquid nitrogen into the cryostat. The cryogen flow rate was optimized, such that any temperature from 77K to 450 K could be achieved quickly with the minimum consumption of

liquid nitrogen.

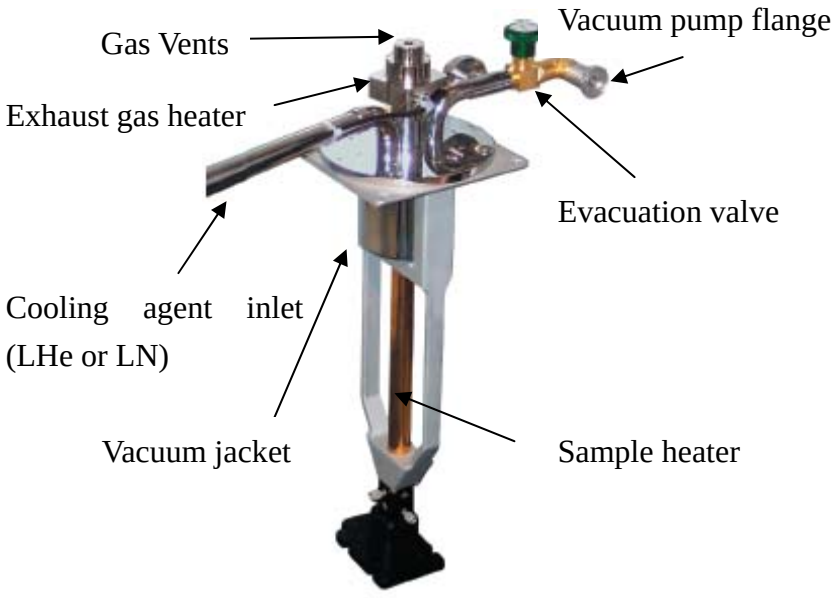

Figure 4-8 Low temperature cryostat for Lakeshore VSM system.

It should be mentioned that there are two heaters in the cryostat; one is the exhaust gas heater, which is located beneath the gas vents, and another one is the sample heater, placed near the bottom of the cryostat. The exhaust gas heater prevents condensation at the gas vents by keeping the temperature at 40^{o}C. The second heater is used to adjust and stabilize the temperature around the sample inside the cryostat. This design allows the sample to be exchanged at low temperature without greatly changing the temperature in the cryostat.

4.3.3.2 Resistance-temperature measurement (RT)

Electrical transport measurements were performed by using a four-point configuration so that the contact resistance would not contribute to the resistances measured. Figure.4.9 depicts the dimensions of the samples and the

electrodes on them. In order to avoid joule heating, a current between 0.1 mA and 100 mA was used to measure the sample resistance. In temperature dependent resistance (RT) measurements, samples were placed inside a close-cycled cryostat. The cooling and heating rates, adjusted by a temperature controller (Lake Shore 321), were set at 5 K/min in temperatures ranging from 20 K to 380 K. The system was automated, and was controlled by a Labview program.

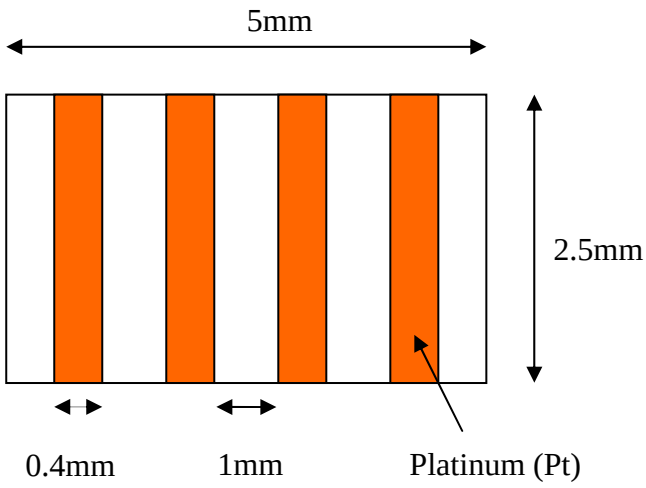

Figure 4-9 Dimensions and geometry of thin films and electrodes for electrical transport measurement.

4.3.3.3 Magneto-transport measurement system (MMS)

The magneto-transport measurement system (MMS) integrates the OmniPlex closed cycle cryostat (CCR) (Model 76014) into the electromagnet of the VSM system. Figure 4.10(a) displays the OmniPlex closed cycle cryostat. As depicted in Figure 4.10 (c), a sample, with the same dimensions and geometry described

in Figure 4.9, was positioned on a home-made PCB. Electrodes of the sample were ultrasonically bonded to the contact pads of PCB, while the pads were soldered with copper wires and connected to the contacts of the sample holder.

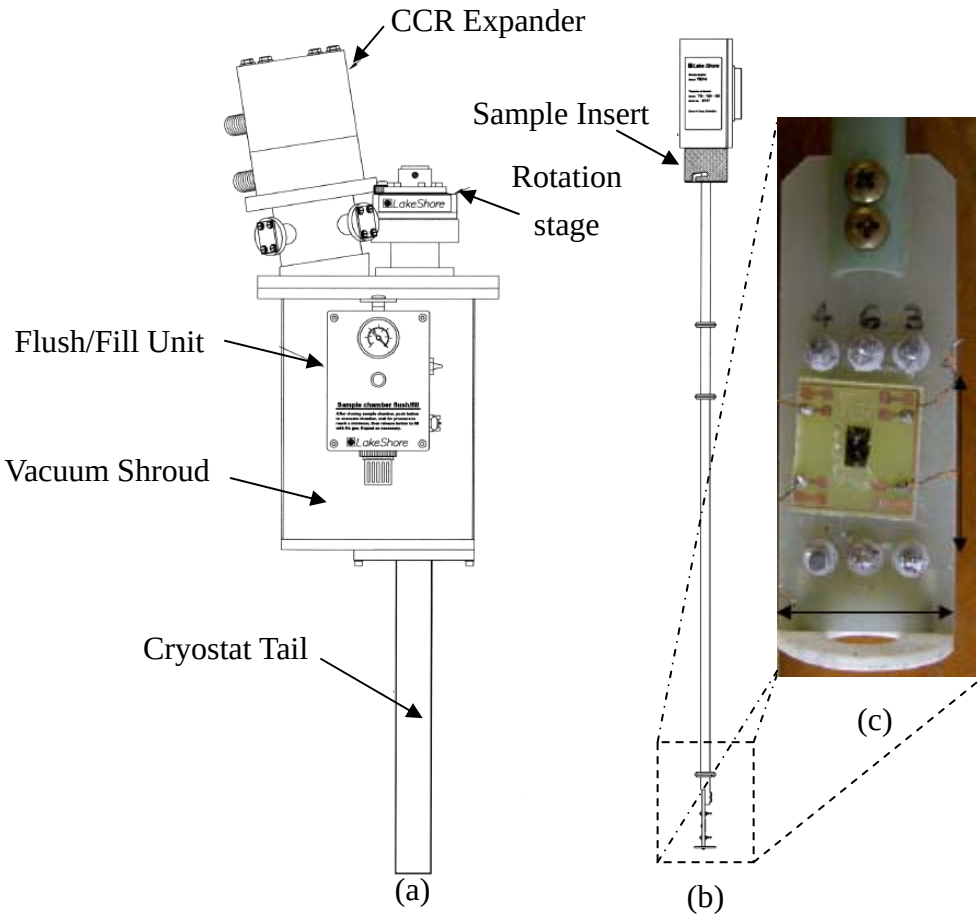

Figure 4-10 OmniPlex closed cycle cryostat assembly (Model 76014), (a) cryostat, (b) sample insert and (c) a photo of a sample mounted on the holder.

The sample, being fixed at the sample holder on the sample insert, was then introduced into the cryostat. Pumping of the sample space was required before cooling. It generally took 2 hours for cooling down from room temperature to 10 K, with a cooling rate 3.25 K/min. Before measurements, the maximum sample current that can be applied without causing joule heating was tested. This

was done by performing I-V measurements with a small but increasing current (starting from the order of μA). Such a test aimed at verifyimg that the sample followed Ohm's law, eliminating the factor of joule heating effect.

Chapter 5 Single-layered Perovskite Thin Films

5.1 Introduction

It has been mentioned that two thin film deposition systems were utilized in this project. The characterization of single layers in this chapter is separated into two parts, describing the characterization of films deposited by PLD and LMBE, respectively. The reason for switching between the two systems arose from the fact that the roughness of LSMRO thin films (to be discussed in this chapter) deposited by the PLD system was too high to be used for PSV fabrications.

In Chapter 4, I introduced the general ideas of fabricating PSV. Before device fabrication, the properties of individual layers in the PSV structure, such as crystallinity and surface roughness, should be thoroughly investigated. Such properties are important for the performances of devices. I have shown, for example, in Section.3.2.4 how the film roughness can deteriorate or enhance the magnitude of GMR. In this Chapter, I will discuss the details concerning the optimization of deposition processes for, and the characterization of, single-layered perovskite thin films. Such layers will be used as the constituents for the spin valve structures.

For that purpose, a standard procedure (Figure.5.1) was followed for conducting the characterization and optimization processes. Deposition of perovskite oxides by PLD has been studied for a long time [5.1]. At the beginning of the optimization process in my work, deposition parameters of various materials were obtained from the literature and used as reference points [5.1, 5.2].In the optimization process, surface morphology of the samples was examined by AFM and crystalline structure by XRD; because both techniques were non-destructive, the samples would not be damaged and subsequent measurements could be conducted. AFM measurements, in particular, required films free from surface contaminations. AFM measurements were conducted before other measurements took place.

The next step were resistance-temperature (RT) measurements, which required preparation of Pt electrodes on top of the perovskite layers. As mentioned in Chapter 4, Curie temperatures (T_c) of the films were estimated by the metal-insulator transition temperature (T_{IM}) in RT measurements. If the estimated Tc was below the value taken from literature, the oxygen pressure for deposition was increased. The optimization procedure of oxygen pressure stopped when the highest T_c of the films was found. Other parameters that determine Tc, such as target-to-substrate distance and substrate temperature

during deposition, could also be changed in the optimization process.

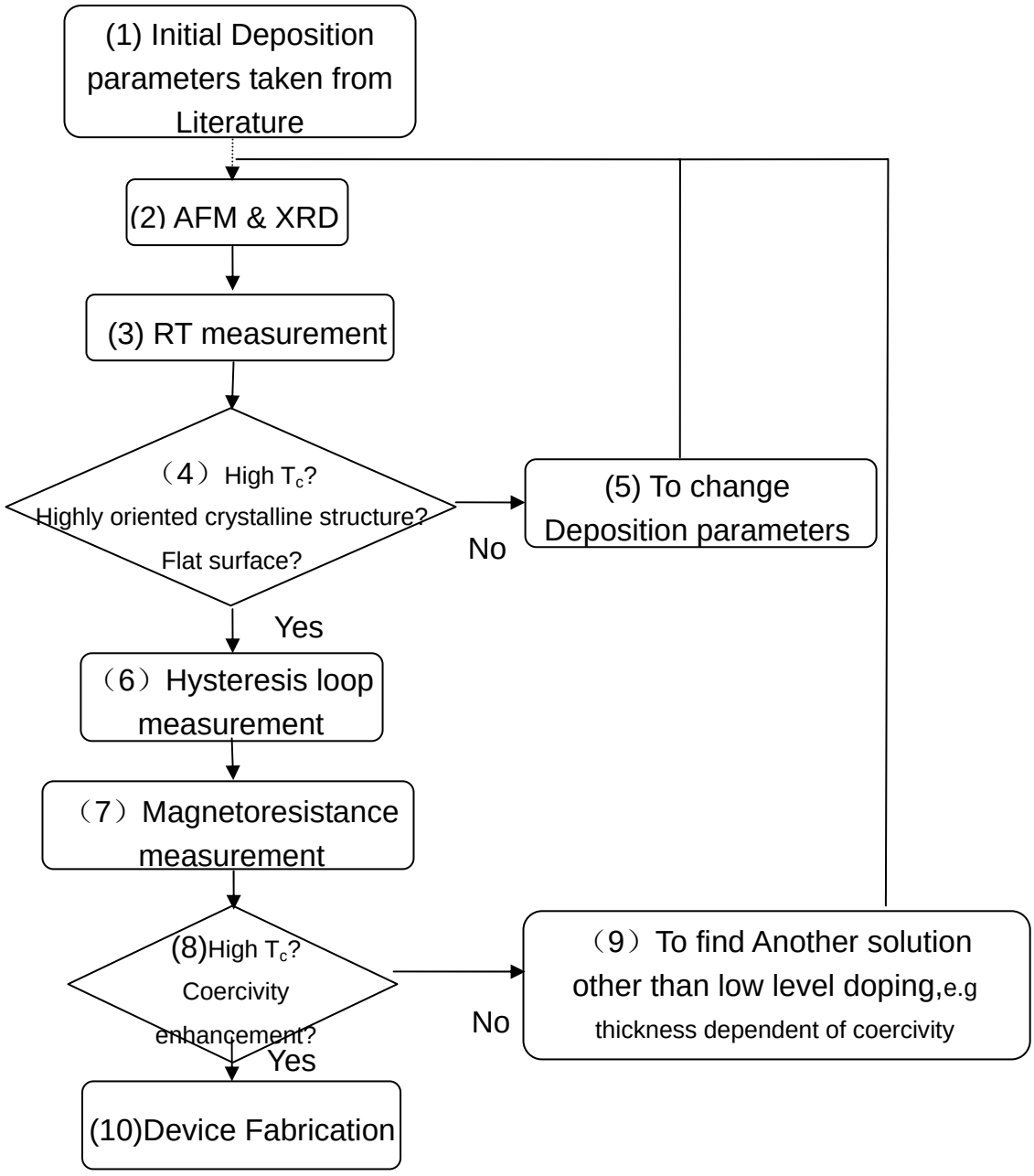

Figure 5-1 Optimization procedures for thin films deposition by PLD and LMBE.

The ultimate goal for conducting these three measurements (AFM, XRD, RT) during the optimization process was to obtain a thin film with high T_c (>300K), high crystalinity (FWHM<0.2), flat surfaces (root-mean squared (r.m.s.)

surface roughness <1 nm in scan area 1μm x 1μm) and high conductivity (~ 10^{-5} Ωm). These conditions can only be obtained by careful optimization of various deposition parameters.

Afterwards, magnetic measurements were performed on the films to verify the Tc (estimated by RT measurements beforehand) and measure the coercivity. The final step of characterizing the single-layered thin film was to investigate the magneto-transport properties to further confirm the coercivity of the films by magnetoresistance measurements. If low- level doping into LSMO was found to be ineffective route for coercivity enhancement, other means (mentioned in Section.2.4.3) would be employed for coercivity enhancement.

It was mentioned that PSVs require two ferromagnetic layers with distinct coercivities to produce pronounced step-like magnetoresistive changes. Therefore, apart from a high degree of crystallinity, low resistivity and surface roughness, the coercivity enhancement in LSMO by doping is also a focus of this Chapter.

It should be noted that deposition parameters and properties of perovskite thin film were summarized at the end of this Chapter (Section.5.8).

5.2 LSMO on LAO (001) by PLD

5.2.1 Surface morphology

The surface morphology of LSMO on LAO (001) substrates was studied. Since one of the works of this project was to fabricate PSV structure, it was necessary to deposit at least three layers of thin films. Rough film surfaces favor the formation of pinholes [5.3, 5.4] (section.3.2.4) and hence degrades the GMR exhibited by PSV. I therefore studied the roughness of thin films to make sure that the films were sufficiently flat for subsequent depositions, suppressing the formation of pinholes.

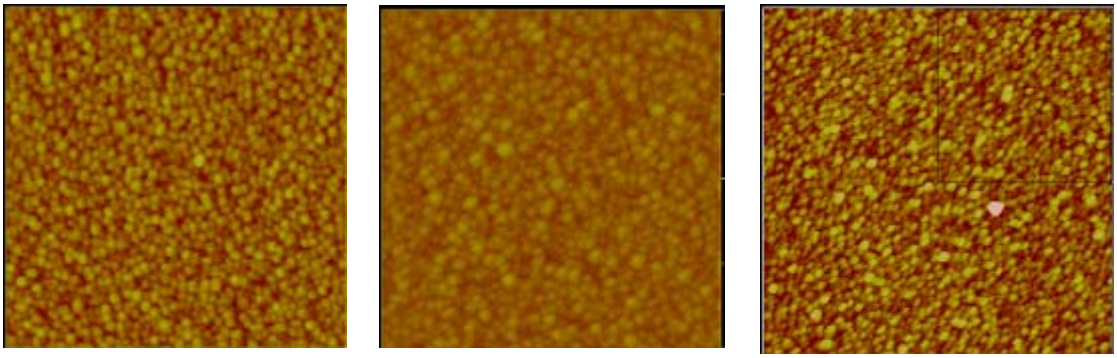

(a) (b) (c)

Figure 5-2 AFM images showing the surfaces of LSMO thin films deposited with different laser fluences: (a) 5.35 J/cm^2, (b) 4.77 J/cm^2 and (c) 3.82 J/cm^2. The r.m.s. roughness for the scans are (a) 1.2 nm, (b) 1.0 nm and (c) 1.0 nm respectively. The scan areas were 1 μm x 1 μm.

Unless specified, the films mentioned in this section were deposited at a substrate temperature of 650 ^{o}C, oxygen pressure of 150 mTorr and laser repetition rate of 5 Hz. As evident from Figure.5.2, the r.m.s. roughness of the

films decreases from 1.2 nm to 1 nm with decreasing laser fluence (scan area 1μm^2). At the lowest laser fluence of 3.82 J/cm^2, the r.m.s roughness was 1 nm and the film thickness was about 88 nm, as determined by SEM cross-sectional imaging. Since surface roughness increases with film thickness, it is important to know the r.m.s. roughness/film thickness ratio. The roughness r.m.s/film thickness is about 1.1%, which is considered to be sufficiently flat.

From the results, a laser fluence of 3.82 J/cm^2 was chosen to obtain smooth surfaces of LSMO thin films.

5.2.2 Microstructure

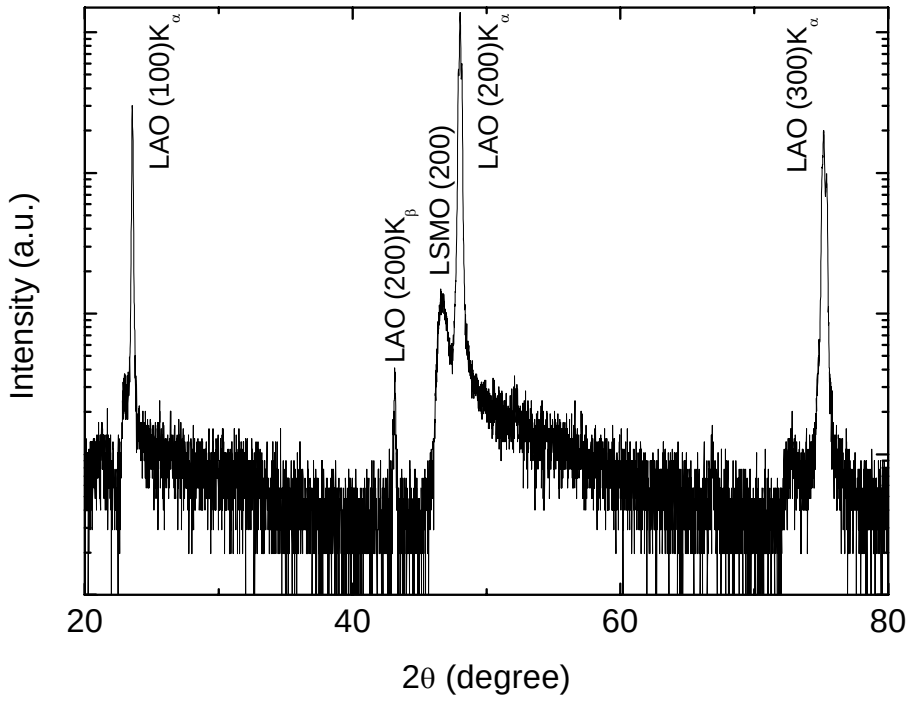

Figure 5-3 XRD θ-2θ diffraction pattern of a LSMO film deposited on LAO (001) substrate.

Figure.5.3 depicts the *θ*-2*θ* scan of a LSMO thin film grown, deposited with a

fluence of 3.82 J/cm^2, oxygen pressure of 150 mTorr, and substrate temperature of 650 ^{o}C, on a LAO (001) single crystalline substrate. (00h) peaks for the substrate and the film are observed, indicating an epitaxial growth of LSMO film on LAO. As shown in Figure.5.4, the rocking curve of LSMO at the (002) peak shows that the film was highly textured with a F.W.H.M of 0.35°.

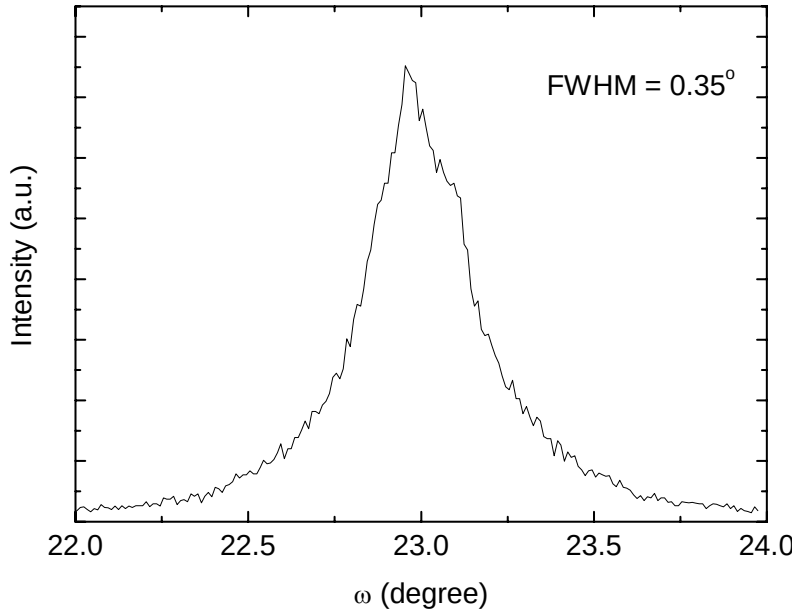

Figure 5-4 XRD rocking curve of LSMO (002) peak.

ϕ-scans in Figure.5.5 further confirmed the epitaxial nature of the film. The ϕ-scans of LSMO (202) and LAO (202) show four diffraction peaks separated by 90°. The four diffraction peaks at each scans indicate the four-fold symmetry of the film microstructure, confirming the cubic structure of the LSMO thin film and the LAO substrate. It should also be mentioned that the four peaks of LSMO in the ϕ-scan are sharp and their corresponding ϕ angles match to those of the peaks of LAO. This indicates that there was a cube-on-cube growth of LSMO

thin film on the LAO substrate.

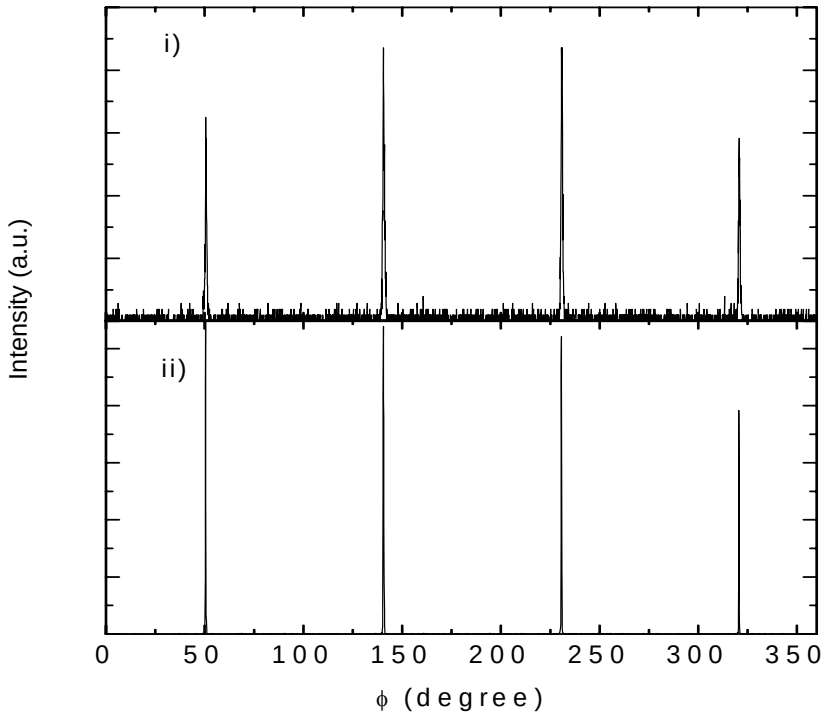

Figure 5-5 ϕ-scan of i) LSMO (202) and ii) LAO (202) planes.

5.2.3 Electrical Characterization

As mentioned in Figure.5.1, RT measurements were conducted after morphological and structural characterizations. Figure.5.6 shows the temperature-dependent resistivity of LSMO thin films deposited under different oxygen ambient conditions. Both LSMO thin films were 50 nm in thickness. For the film deposited under 100 mTorr oxygen ambient, it exhibited a semi-conducting behavior below 300 K. It was expected that similar behaviour would be observed above 300 K, because metal-semiconductor transition would only occur at temperatures below $T_{IM.}$ Measurements at higher temperatures were

therefore skipped. For the film deposited under an oxygen pressure of 150 mTorr, it showed a semi-conducting behavior above 330 K. On the other hand, it demonstrated a metallic behavior at the temperature ranging from 200 to 330 K, implying the existence of a ferromagnetic behavior in this range. The metallic-semiconducting transition (330K) is quite high, compared with the films deposited under a similar situation [5.5]. The resistivity at 300 K was about 3.9×10^{-5} Ωm.

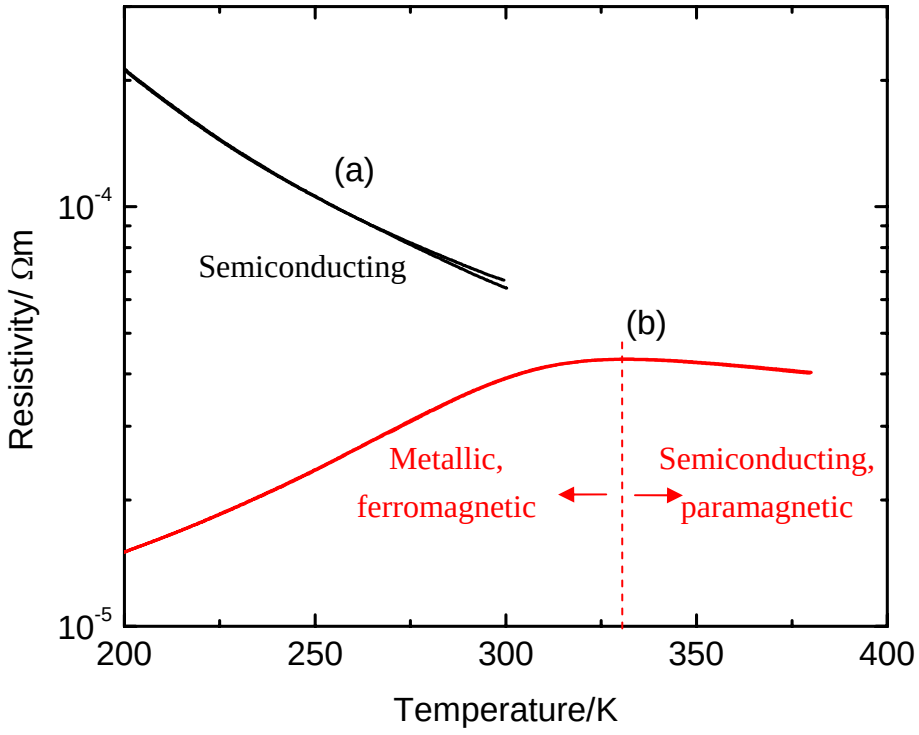

Figure 5-6 Temperature dependence of resistivity of LSMO thin films deposited under oxygen pressure of (a) 100 mTorr and (b) 150 mTorr.

Therefore, by considering results of RT measurements, an oxygen pressure of 150 mTorr was considered to be the optimal value for LSMO film deposition.

5.2.4 Magnetic and Magnetotransport Measurements

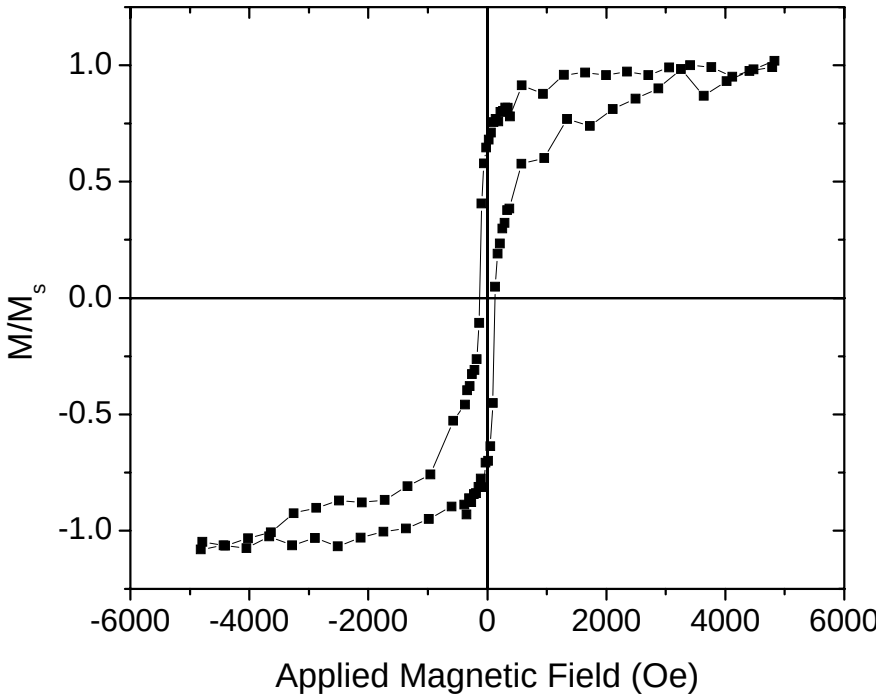

Figure 5-7 Hysteresis loop of an optimized, 50-nm thick LSMO film at 100 K. The external magnetic field was applied in-plane.

Figure.5.7 displays the field-dependent magnetization (MH) measurement of a LSMO thin film (thickness 50 nm) at 100 K, when the magnetic field was applied in the in-plane direction. Assuming that the LSMO thin film was saturated above 2000 Oe, the saturation magnetic moment was about 0.293 memu, equivalent to 3.03 μ_B/Mn ion. This represents a very strong ferromagnetic response compared with theoretical limit of 3.59 μ_B/Mn [5.6]. The coercive field of the film was about 130 Oe.

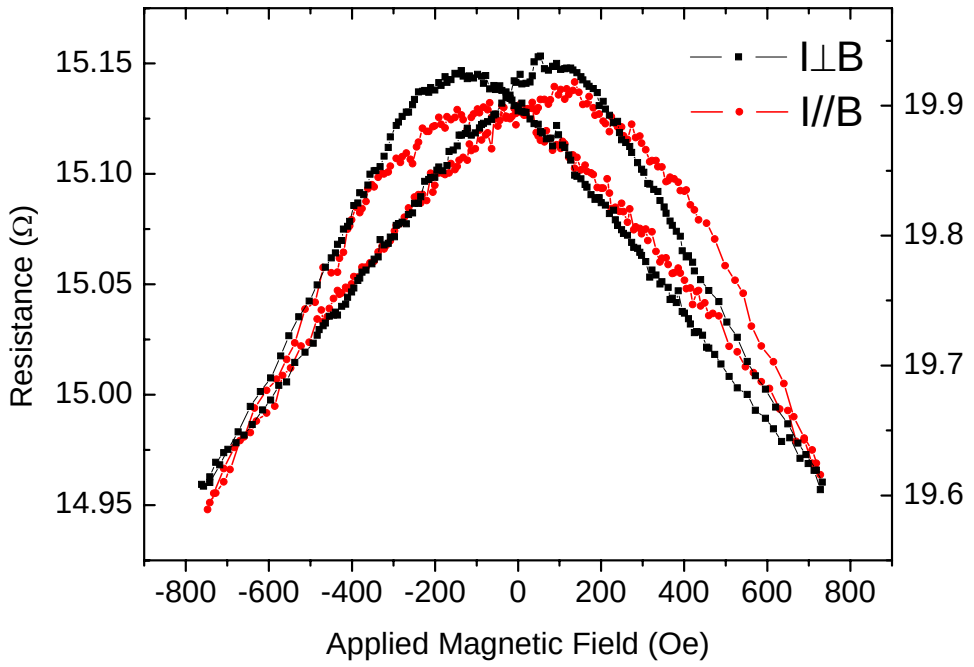

Figure 5-8 Magnetotransport measurements of a LSMO thin film at 20 K, when a magnetic field was applied along the sample plane. The applied current was parallel (•) and the current was perpendicular (■) to the field, respectively.

The LSMO thin film exhibited negative magnetoresistance when an in-plane field was applied parallel to the electric current, as shown in Figure.5.8. The film showed similar behavior in magnetotransport measurement with the in-plane field applied either parallel or perpendicular to the electric current. This kind of independence of magnetoresistive behavior to the relative orientation between applied current and field arises from the intergranular tunneling magnetoresistance reported by Hwang *et al.* [5.7] In other words, the film did not demonstrate AMR. Li [5.8] showed that such intergranular tunneling magnetoresistance can be as large as 15% in polycrystalline films. However, in this work, the LSMO thin film was highly textured, and the magnitude of MR

was about 0.8 % at 1000 Oe, which is comparable with reported value in the literature [5.8]. Figure.5.8 also indicates the MR peaks at 130 Oe, which match well with the coercivity of the film as obtained from MH measurement.

5.3 LNSMO on LAO (001) by PLD

For LNSMO thin film, study of surface morphology and microstructure will not be shown, but will only be summarized in Section.5.8. The r.m.s roughness of perovskite manganite films with deposition conditions as mentioned in Section.5.2 (substrate temperature 650 ^{o}C, oxygen pressure 150 mTorr, and laser fluence 3.82 J/cm^{2}) was generally below 1.5 nm, which is sufficient for the fabrication of PSV structures. The optimally-grown LNSMO thin films showed similar behavior (r.m.s roughness <1.5 nm). Regarding the micro structure characterization, features of microstructure of LNSMO films were very similar to those of LSMO films. Therefore, morphological and microstructural characterization was skipped, and the first step of characterization was to study the electrical transport properties of LNSMO thin films.

5.3.1 Electrical Transport Measurements

The influence of oxygen partial pressure on the properties of LNSMO was characterized by electrical measurement. Figure.5.9 clearly shows

metal-insulator transition for all samples deposited at different oxygen pressures. The resistance dropped dramatically when the oxygen partial pressure was increased from 100 to 300 mTorr. Since the thicknesses of the films were not determined, the resistivities cannot be obtained. However, it was obvious that the resistivity of the film deposited under 100 mTorr oxygen pressure was much larger than those of the others, given that all other deposition conditions were identical and all films were deposited on 2.5 x 5 mm^2 substrates. Under such circumstances, the measured resistances can only be changed by the film thickness and oxygen pressure. It can be clearly observed that the resistance values of the film deposited with 100 mTorr oxygen pressure was two orders of magnitude larger than those of the others. However, it would be unphysical for the film thickness to change by this amount to give such a large difference in resistance value. Therefore, the resistivity of the films was expected to decrease with increasing oxygen pressure. However, from observing the resistance value of the films deposited with 200, 250 and 300 mTorr oxygen pressure, the same conclusion cannot be drawn with certainly, due to the small changes in resistance values among these samples.

Eventually, an oxygen pressure of 200 mTorr was chosen for the deposition of LNSMO. Such a pressure yielded the highest obtainable T_{IM} or T_c as well as a

low resistivity. Oxygen pressures higher than 200 mTorr were not chosen, because such conditions would greatly increase the surface roughness of the films [5.1] and reduce the deposition rate.

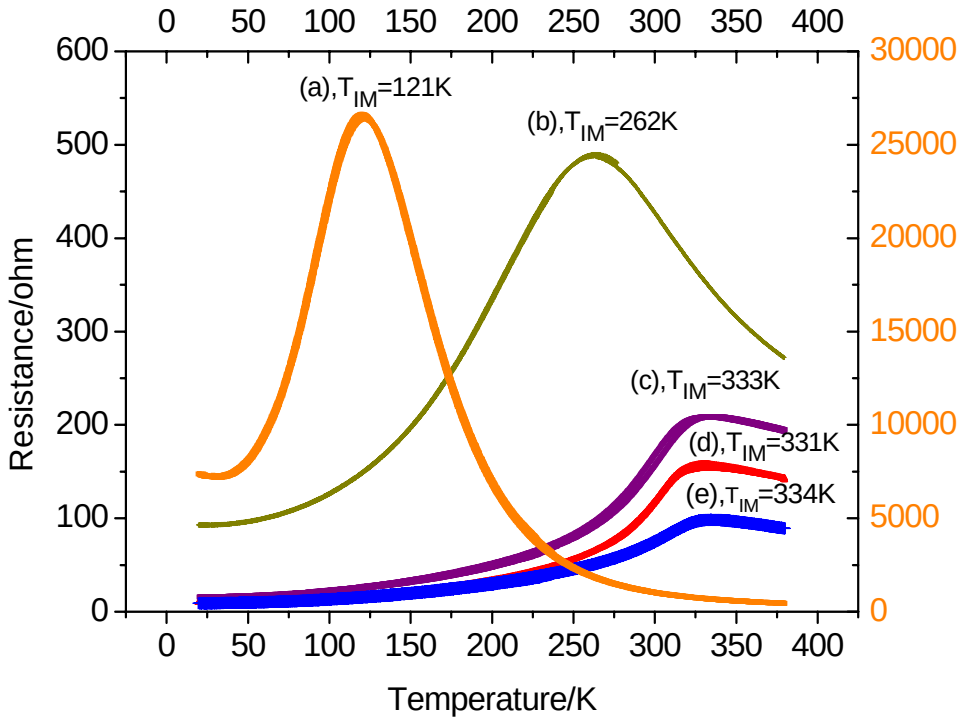

Figure 5-9 Temperature dependence of resistance for LNSMO films deposited under different oxygen pressures: (a) 100 mTorr, (b) 150 mTorr, (c) 200 mTorr, (d) 250 mTorr and, (e) 300 mTorr. The scale on the right axis (orange) is for curve (a) only. The corresponding metal-insulator transition temperatures T_{IM} are shown next to the curves.

For sake of simplicity, the resistivity of the LSMRO film deposited at 200 mTorr oxygen pressure (Figure.5.10) was measured with on a second film with twice the deposition time, other deposition conditions being identical to the sample represented by curve (c) in Figure.5.9. This made the film thickness measurement by SEM easier and more accurate. The measured resistivity of LNSMO deposited under such conditions was 4.5 x10^{-5} Ωm at 300 K. This

corresponds to a very high conductivity compared with numerous ferromagnetic oxides [5.9, 5.10]

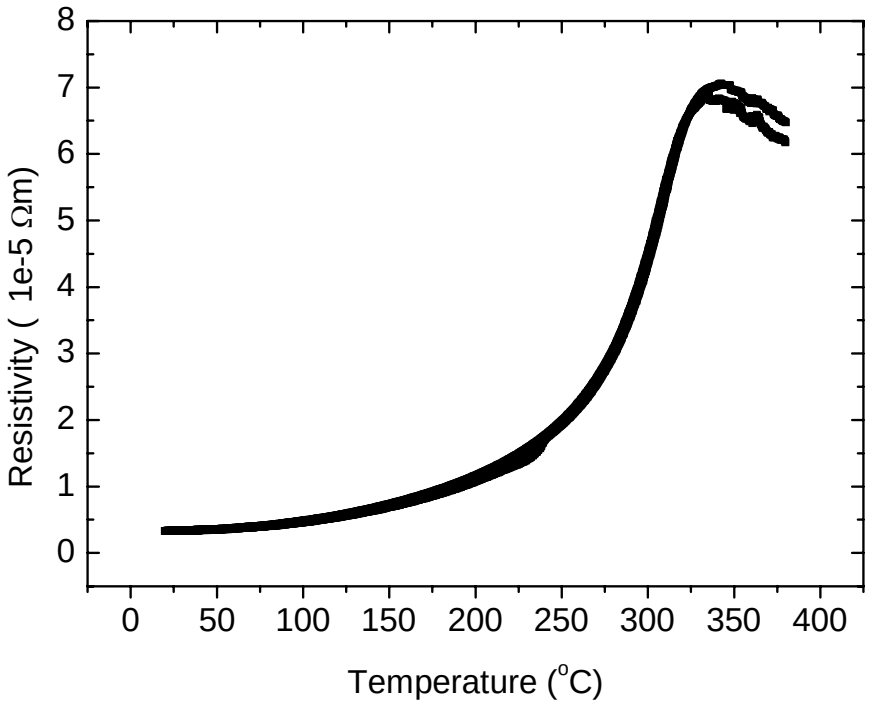

Figure 5-10 Resistivity against temperature plot of LNSMO deposited with oxygen partial pressure 200 mTorr.

5.3.2 Magnetic characterization

From M-H measurement (data not shown), the LNSMO film exhibited a magnetization of 3.14 μ_B/Mn at 100 K when it was saturated. Compared with LSMO, the saturation magnetization of LNSMO in terms of μ_B/Mn was about the same. As shown in Figure.5.11, the coercive field (~90 Oe) of LNSMO thin film was also comparable with that of LSMO. However, the goal of depositing LSMRO was to fabricate PSV with ferromagnetic layers having marked contrast in coercivity. Based on the result in Figure 5.11, LNSMO was not suitable to be

used as one of ferromagnetic layers in the PSV.

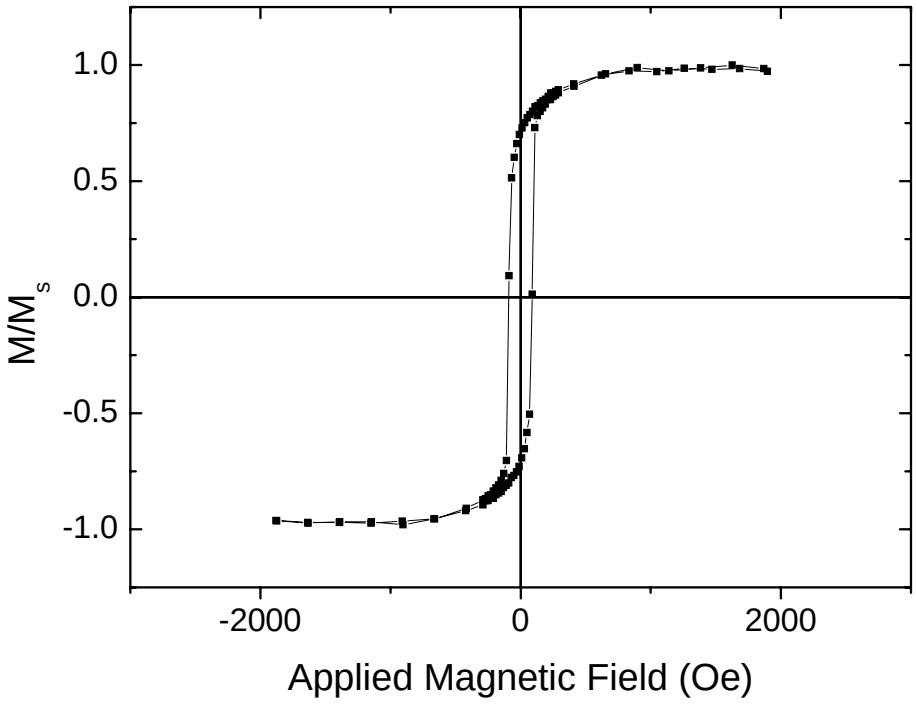

Figure 5-11 M-H plot of LNSMO thin film at 100 K when in-plane field was applied.

5.4 LSMRO on LAO (001) by PLD

5.4.1 Surface Morphology

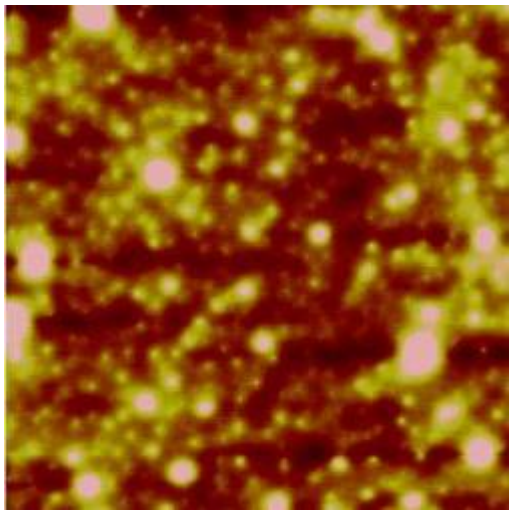

Figure 5-12 AFM image of LSMRO thin film deposited at 830^{o}C and 150 mTorr. The scan area was 10 μm x 10 μm.

Figure.5.12 depicts the AFM image of LSMRO thin film grown at a substrate temperature of 830^{o}C and oxygen pressure of 150 mTorr. The r.m.s roughness of the thin film surface was about 6.6 nm, representing a relatively rough surface. The rough surface may originate from the high substrate temperature, in combination with the high oxygen pressure as reported by Koubaa *et al* [5.1]. Small 'islands' can be observed in Figure.5.12, which was probably due to island growth rather than 2-D growth during deposition or due to large particles struck by high laser energy. The poor surface cannot be improved simply by decreasing the substrate temperature in this case, because a high substrate temperature is required for the growth of epitaxial LSMRO [5.11]. The rough surface could be one of the reasons why no GMR effect was exhibited in the CIP device grown in this work, which will be further discussed in the next chapter.

5.4.2 Microstructure

X-ray diffraction measurement in θ-2θ geometry was used to detect the out-of-plane lattice constant of the films, and the results are shown in Figure.5.13. For epitaxial LSMO films ($a_{LSMO\ bulk}$ ~3.873 Å) deposited on LAO (a_{LAO} ~ 3.788 Å), they are under in-plane compressive strain because a_{LSMO} is larger than a_{LAO}. The lattice mismatch δ (where $\delta = (a_{substrate} - a_{LSMO})/a_{substrate}$) between

LAO and LSMO is -2.2%. This negative lattice mismatch induces a lattice distortion and perpendicular magnetic anisotropy. Such results have been reported widely in literature [5.12] and in our previous work [5.13]. The two features are further enhanced in case of LSMRO, because of the increase in lattice parameters by Ru doping.

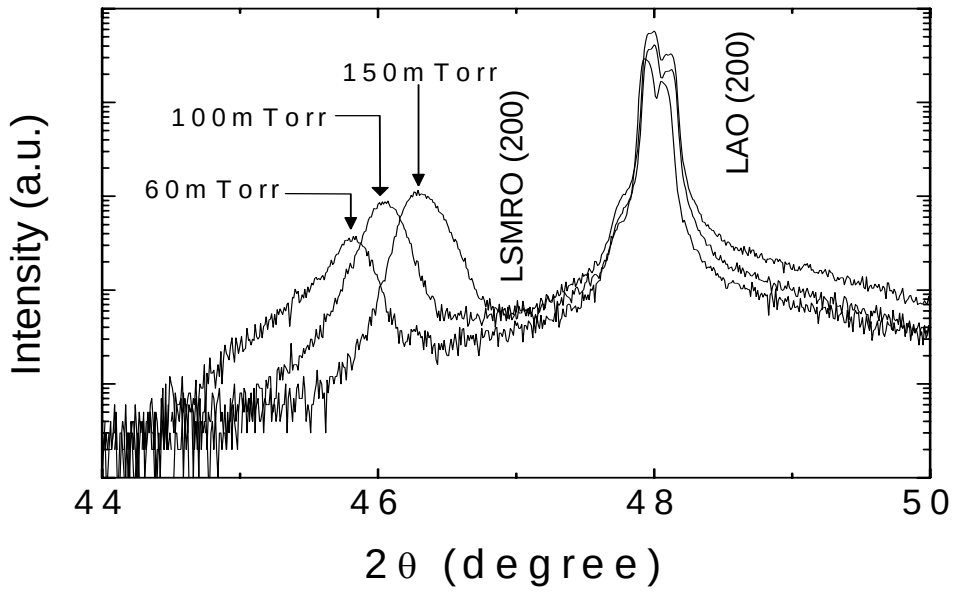

Figure 5-13 θ-2θ scans of LSMRO thin films deposited at 830 ^{o}C with different oxygen pressures.

As shown in Figure.5.13, the out-of- plane lattice constants were 3.921, 3.940 and 3.958Å for films deposited in oxygen pressure of 150 mTorr, 100 mTorr and 60 mTorr, respectively. Attention is drawn on the work by Yamada *et al*., [5.2], who have observed an *increase* in c-axis lattice constant in Ru-doped (La,Sr)MnO_3 (with x = 0.4) as the ambient oxygen increased from 0 to 60 mTorr. In their work, the relatively low oxygen pressure led to Ru deficiency in the films, and hence a small lattice parameter which resembled that of films without Ru

doping. The drop of lattice constant with increasing oxygen pressure, as observed in Figure.5.13, could be related to the oxygen deficiency effect, as suggested in previous studies on LSMO [5.5] and also evidenced in other measurements performed in this work, which will be shown later.

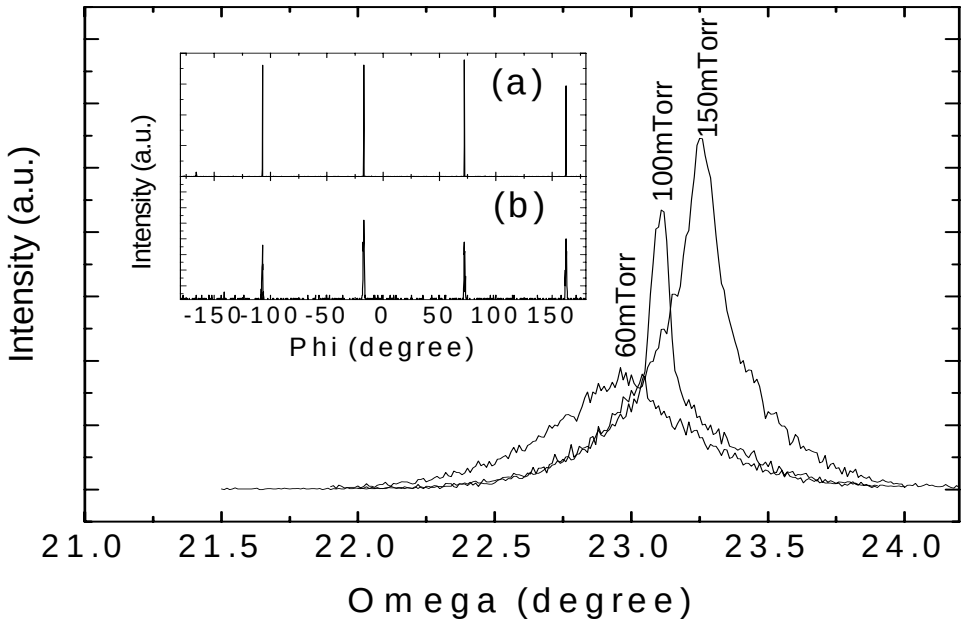

Figure 5-14 Omega scan of LSMRO thin films deposited under different oxygen pressures. The inset shows the phi scan on the (a) LAO (002) substrate and (b) LSMRO (002) reflection of the film deposited at 150 mTorr oxygen pressure.

Figure.5.14 illustrates the rocking curve measurements of the LSMRO films. The FWHM of the rocking curves were between 0.29° (oxygen pressure = 150 mTorr) and 0.59° (60 mTorr), showing an improved film crystallinity with increasing oxygen pressure. The enhanced crystallinity is related to the oxygen stoichiometry of the films. If the oxygen ambient pressure was further increased, Koubaa *et al* [5.1] discovered that other phases could be induced and deteriorate

the film crystallinity. The ϕ scan of the sample deposited in an oxygen pressure of 150 mTorr (inset of Figure.5.14) shows cube-on-cube growth of LSMRO thin film on LAO substrate, further indicating the high quality of the film.

5.4.3 Electrical Measurements

RT curves of LSMRO thin films are plotted in Figure.5.15. Samples deposited with higher oxygen pressure showed lower resistivity over the whole temperature range measured. Metallic semiconducting transition effect, manifesting itself through a peak in the R-T curve, was observed only for films deposited under oxygen pressures of 100 mTorr and 150 mTorr. Resistance peaks occur at temperatures (denoted as T_p) of 270 K and 330 K for the two samples, respectively. The film deposited with an oxygen pressure of 60 mTorr did not show any resistance peak over the whole measured temperature range. In manganite thin films, the ferromagnetic state is always accompanied by a metallic conduction behaviour, while the paramagnetic state is semiconducting [5.14], and T_p is approximately equal to T_c. Figure.5.15 therefore suggests that the LSMRO film deposited under an oxygen pressure of 150 mTorr is ferromagnetic at room temperature.

From Figure.5.15, the room-temperature resistivity of LSMRO film grown at 60 mTorr is at least an order of magnitude larger than that of other samples.

The resistivity of the film deposited under 150mTorr is 2.52 x 10^{-5} Ωm at 300 K, which is slightly lower than that of LSMO at the same temperature (~3.2 mΩcm). As shown from the results displayed so far, the LSMRO film deposited under an ambient oxygen of 150 mTorr was single-phased, had the highest crystallinity, and also demonstrated the highest T_C and lowest resistivity among all the samples. I therefore suggest that the optimal growth conditions for LSMRO films is with an ambient oxygen pressure of 150 mTorr and a substrate temperature 830 °C.

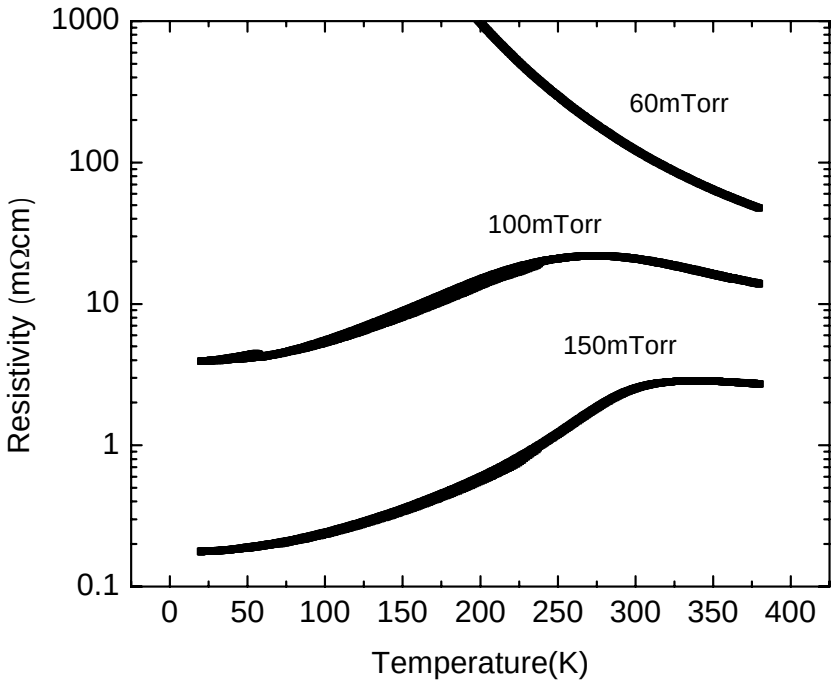

Figure 5-15 Temperature dependence of resistivity for LSMRO films deposited with different oxygen pressures.

5.4.4 Magnetic and Magnetotransport Measurements

Hysteresis loop measurements of LSMO and LSMRO are shown in Figure.5.16. It can be observed that the coercivity (310 Oe) of LSMRO thin film

(100 nm) was about 2.5 times (130 Oe) larger than that of undoped LSMO film (100 nm) at 80 K. Inset of Figure.5.17 illustrates the temperature dependence of hysteresis loops of the LSMRO thin film. The coercivity reduces gradually with increasing temperature. At around 300 K, the coercive field (~35 Oe) of the LSMRO thin film was still higher than that of single crystalline LSMO thin film(~2-5 Oe), providing sufficient coercivity contrast for the PSV so fabricated. The temperature dependence of M-H measurements also showed that the film exhibited ferromagnetic behavior even at 330 K (data not shown). As can be seen in Figure.5.18, the film exhibited anisotropic magnetoresistance effect (AMR), in which the resistance changes according to the relative orientation between the applied current and the magnetic field. The physical origin of AMR is due to spin-orbit coupling in the lattice [5.15]. The peaks of the AMR measurements indicate the coercive field (~500 Oe at 10 K) of the LSMRO thin film.

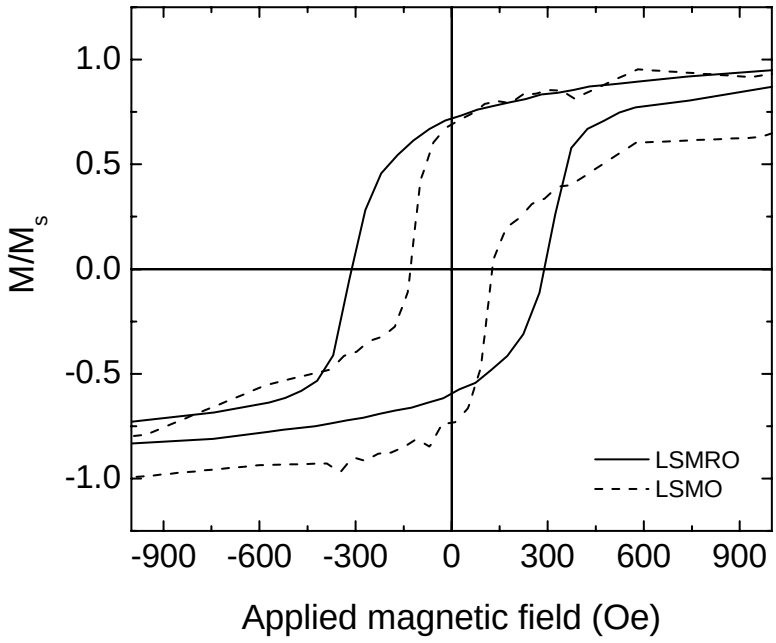

Figure 5-16 Normalized magnetization versus field measurements of optimized LSMO and LSMRO films at 80 K.

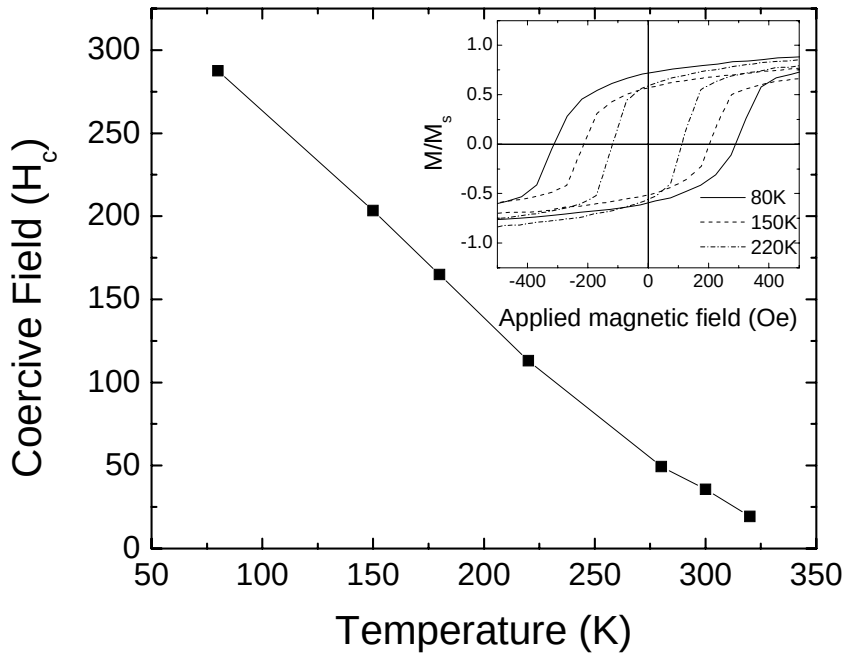

Figure 5-17 Temperature dependence of coercive field of LSMRO film deposited under an oxygen pressure of 150 mTorr. The inset shows the M-H plot of the LSMRO film measured at 80, 150, 220 K.

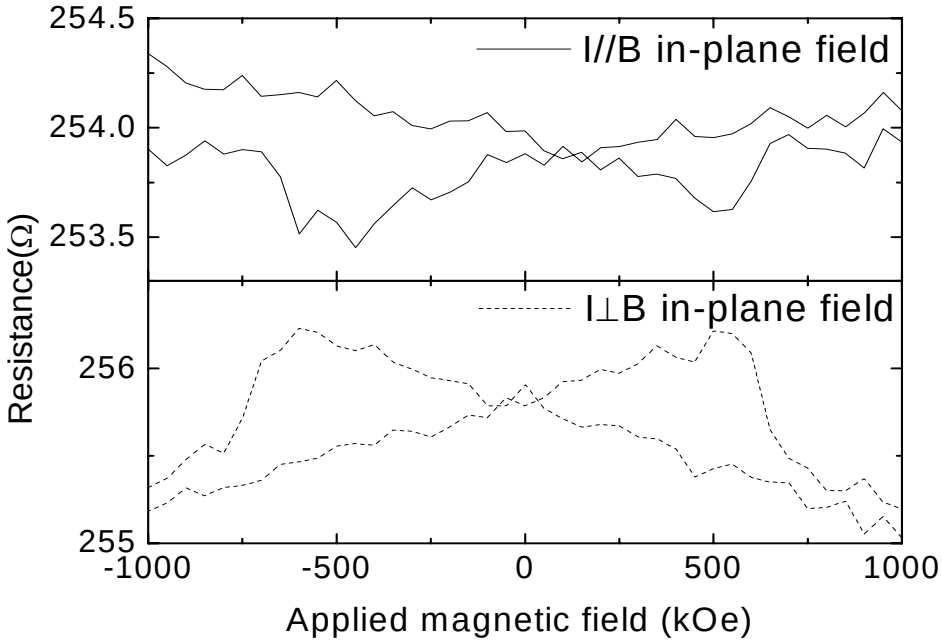

Figure 5-18 Magnetoresistance measurements of LSMRO thin film deposited under oxygen pressure of 100 mTorr at 10K.

Optimally-grown LSMRO thin films showed a coercivity enhancement compared with LSMO thin films of the same thickness. A three-fold increase of coercivity can be obtained at low temperatures, without greatly compromising the T_C and conductivity. These suggest the suitability of LSMRO thin films as one of the ferromagnetic electrodes for PSV structures.

5.5 LNO on LAO (001) by PLD

5.5.1 Surface Morphology

Similar to LSMO, LNO thin films exhibited a decrease in surface roughness with decreasing laser fluence. This can be observed from Figure.5.19. For the film deposited with a laser fluence 6.11 J/cm^2 (Figure.5.19 (a)), the

surface was highly irregular, with large grain size and bumpy surface, and the r.m.s roughness was 5.6 nm. With the laser fluence of 3.82 J/cm^2 (Figure.5.19(c)), the r.m.s roughness/film thickness was about 2.1% when the scan area was 5 μm x 5 μm and the film thickness was about 67 nm. In addition, Figure.5.19(c) exhibits the presence of outgrowth on the films. Such outgrowth increases the roughness of the surfaces and hence disrupts the epitaxial growth of subsequent deposited layers. The outgrowth effect of YBCO/STO (both YBCO and STO have similar structure and lattice parameter with LNO and LSMO) multilayer structure was studied and was shown to have a significant influence epitaxial growth of subsequently deposited layers [5.16]. Methods such as low laser repetition rate can be used to reduce the outgrowth effect on the films.

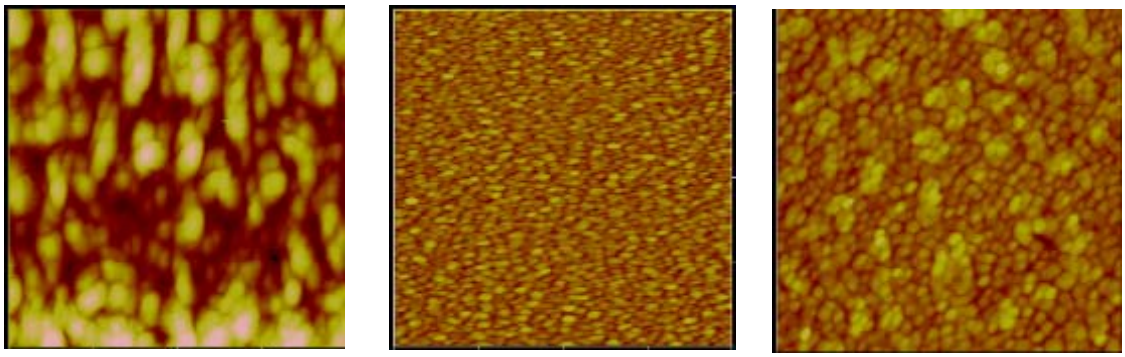

(a) (b) (c)

Figure 5-19 AFM images showing the surface of LNO thin films desposited with laser beam energy (a) 6.11 J/cm^2, (b) 4.77 J/cm^2 and (c) 3.82 J/cm^2 with r.m.s. roughness (a) 5.6 nm, (b) 1.3 nm and (c) 1.4 nm respectively. The scan areas were 1μm x 1μm.

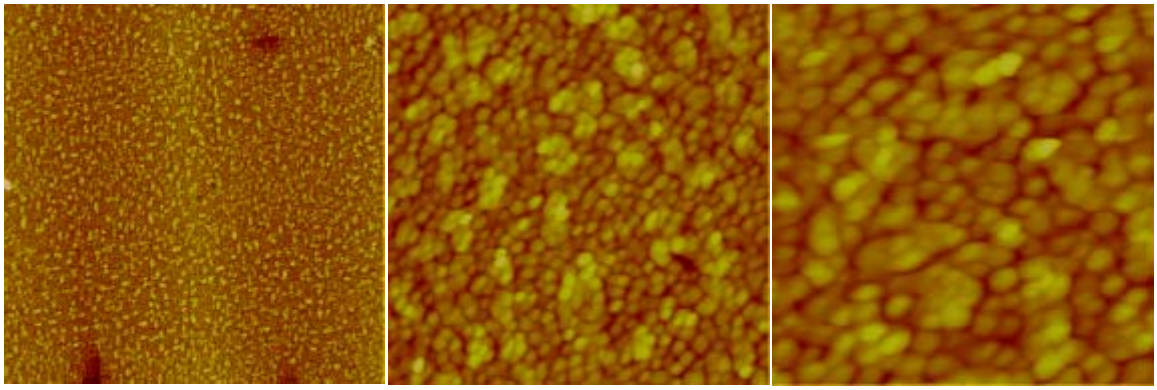

(a) (b) (c)

Figure 5-20 AFM images showing the surface of LNO thin film deposited with laser beam energy 3.82 J/cm^2, with different scan area (a) 5 μm x 5 μm, (b) 1 μm x 1 μm and (c) 0.5 μm x 0.5 μm. The r.m.s. roughnesses were (a) 1.4 nm, (b) 1.3 nm and (c) 1.2 nm.

5.5.2 Microstructure

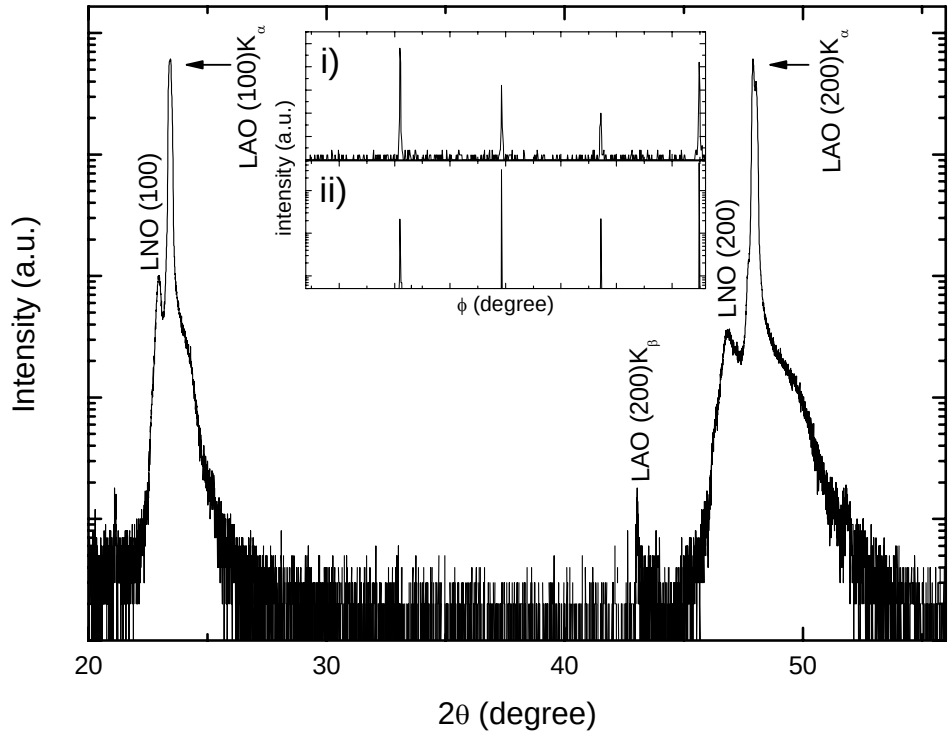

Figure 5-21 XRD θ-2θ scan of LNO film deposited on LAO (100) substrate. Inset shows ϕ scans of (i) LNO (202) and (ii) LAO (202).

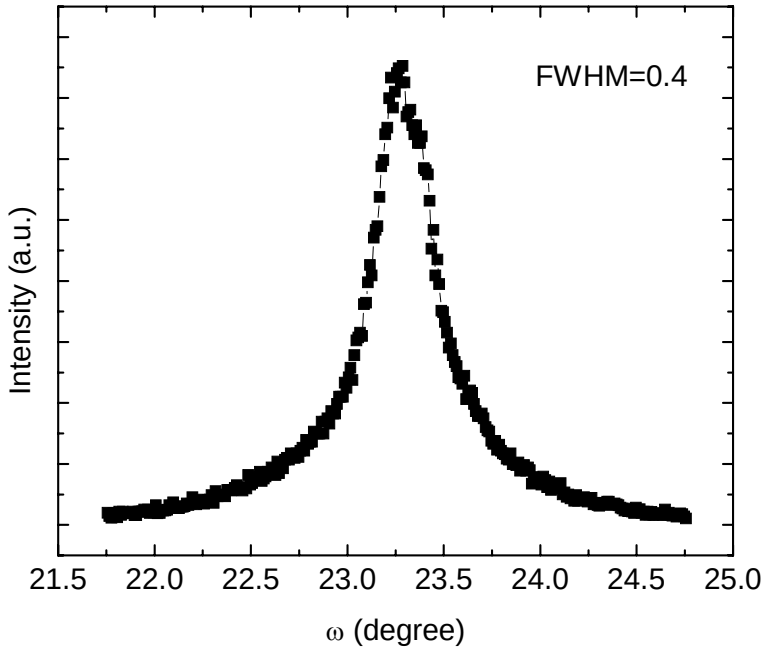

Figure 5-22 XRD ω scan of LNO (002) peak.

Figure.5.21 describes the XRD θ-2θ profile of LNO thin film deposited under an oxygen pressure of 150 mTorr, with a substrate temperature 650 ^{o}C and laser fluence of 3.82 J/cm^{2}. Most of the features shown by the diffraction patterns of the LNO thin film on LAO were similar to those of the LSMO on the LAO (Section 5.2). From Figures.5.21 and 5.22, the θ-2θ scan shows (00h) peaks of the LNO film on LAO substrate, and the ω scan illustrates that the corresponding (002) peak was highly textured with F.W.H.M=0.4°. The inset in Figure.5.21 further indicates the cube-on-cube growth of the highly-crystalline LNO thin film on LAO substrate.

5.5.3 Electrical Transport Measurements

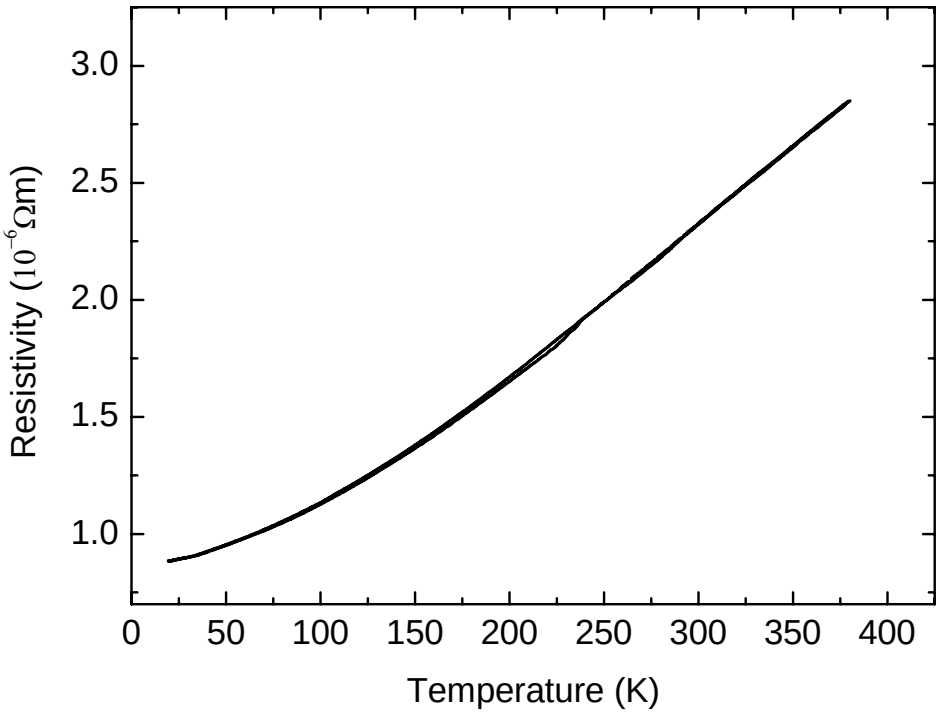

Figure 5-23 Plot of resistiviety against temperature of LNO film on LAO substrate.

RT measurement of LNO film is shown Figure.5.23, which was performed by the four–point-probe method mentioned in Section.4.3.3.2. Figure.5.23 shows that LNO exhibited a metallic-like transport behaviour over the whole temperature range measured (20-380K). In contrast with the resistivity of LSMO (Section.5.2), the resistivity of LNO (2.3 μΩm) was about one order of magnitude smaller at 300 K. It should be reminded that LNO thin film is non-ferromagnetic from 20K to 380K [5.17], which was confirmed by M-H measurements of the film (data not shown).

5.6 LSMO on LAO (001) and STO (001) by LMBE

5.6.1 Introduction

The characterization methods and the features of LNO and rare earth doped LMO and LNO thin films deposited by LMBE were very similar to those prepared by PLD. Therefore, general characterizations such as surface and microstructure studies, will not be included in this dissertation. Instead, a table summarizing the results obtained from the characterizations of samples will be shown in Section.5.8. The subsequent sections will introduce specialized topics, including magnetic anisotropy of LSMO films and anomalous temperature dependence of resistivity in LNO films.

5.6.2 Magnetic anisotropy

5.6.2.1 Substrate dependence

Figure.5.24 depicts hysteresis loops obtained from a LSMO film grown on LAO (001) under optimized conditions, when the external field applied either in-plane or out-of-plane. The LSMO film exhibited an in-plane magnetic anisotropy when the film was about 100nm in thickness. The out-of-plane hysteresis loop in the Figure.5.24 illustrated that the hard axis was in the out-of-plane direction. This is in contrast with LSMO film of the same thickness

grown on STO (001) substrate, as shown in Figure.5.25. The difference in magnetic anisotropic behavior could be ascribed to the stress induced by substrates (compressive stress for LSMO film on LAO substrate and tensile stress for LSMO on STO) as mentioned in Section.2.7.

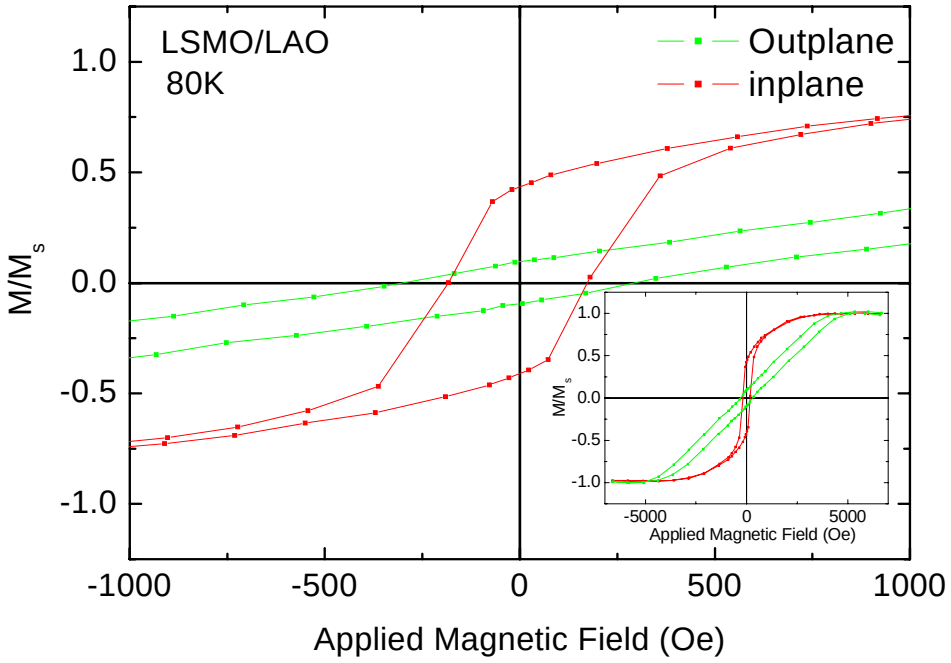

Figure 5-24 Normalized hysteresis loops of an optimized LSMO film (100 nm) on LAO (001) substrate at 80 K, measured with magnetic field applied parallel (red curve) and normal (green curve) to the film plane, respectively. Inset shows the M-H loops in enlarged field scale.

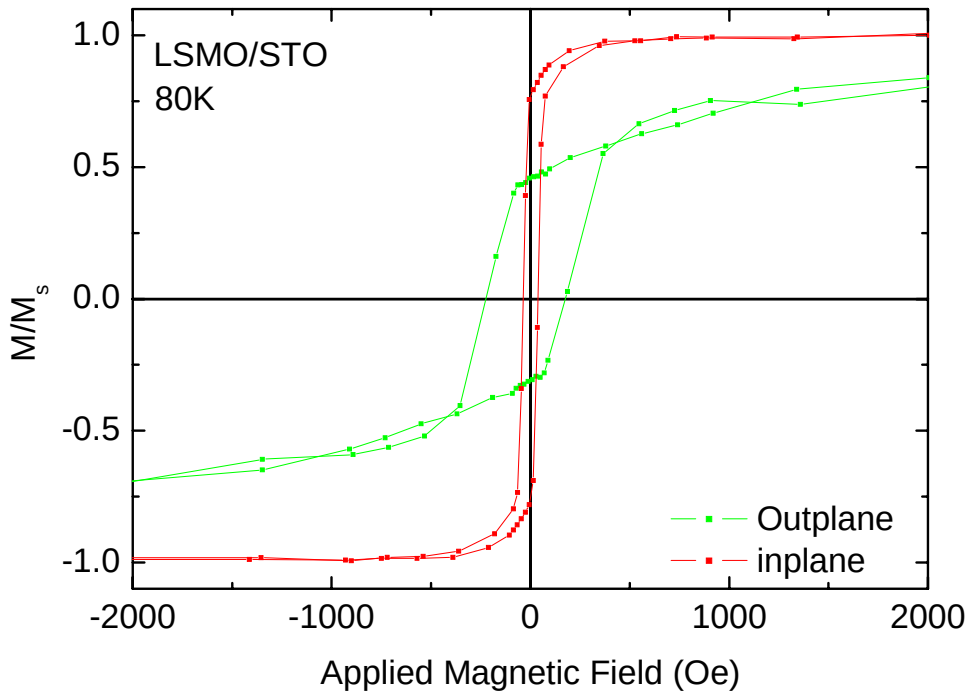

Figure 5-25 Normalized hysteresis loops of optimized LSMO film on STO (001) substrate at 80 K, measured with magnetic field applied parallel (red curve) and normal (green curve) to the film plane, respectively.

5.6.2.2 Thickness dependence

In the last section, I have shown the substrate dependence of magnetic anisotropy in LSMO thin films. This provides me a deeper understanding on the magnetic properties of manganite films and hence gives a clue for device fabrication. Apart from substrate dependence of magnetic anisotropy of LSMO, other group [5.18, 5.19] also studied the thickness dependence of magnetic anisotropy. In this Section, variations of magnetic anisotropy in LSMO films with different thicknesses are studied.

Depositions of three LSMO thin films with different thicknesses were performed, aiming at studying the dependence of coercive field with film

thicknesses. It can be seen from Figure.5.26 that there was coercivity enhancement for 15-nm thick LSMO film (320 Oe) compared with another sample with a thickness of 100 nm (180 Oe). Although coercivity enhancement was observed in the thinner film, complications will arise during the fabrication of CPP devices. This is because critical control of etching processes is necessary for fabricating CPP device. If the bottom layer is too thin (< 20 nm), etching for the preparation of bottom electrodes will become extremely difficult to control.

Other than coercivity enhancement, magnetic anisotropy can also be changed from in-plane to out-of-plane direction, as the film thickness was lowered from 15 nm to 7.5 nm (Figures.5.26 to 5.28). From Figures.5.26 and 5.27, LSMO thin films with thickness 15 and 100 nm showed in-plane anisotropy. By contrast, perpendicular anisotropy was shown by the sample with thickness 7.5 nm (Figure 5.28). Therefore, a transition of magnetic anisotropy took place for LSMO films at a thickness between 7.5 and 15 nm.

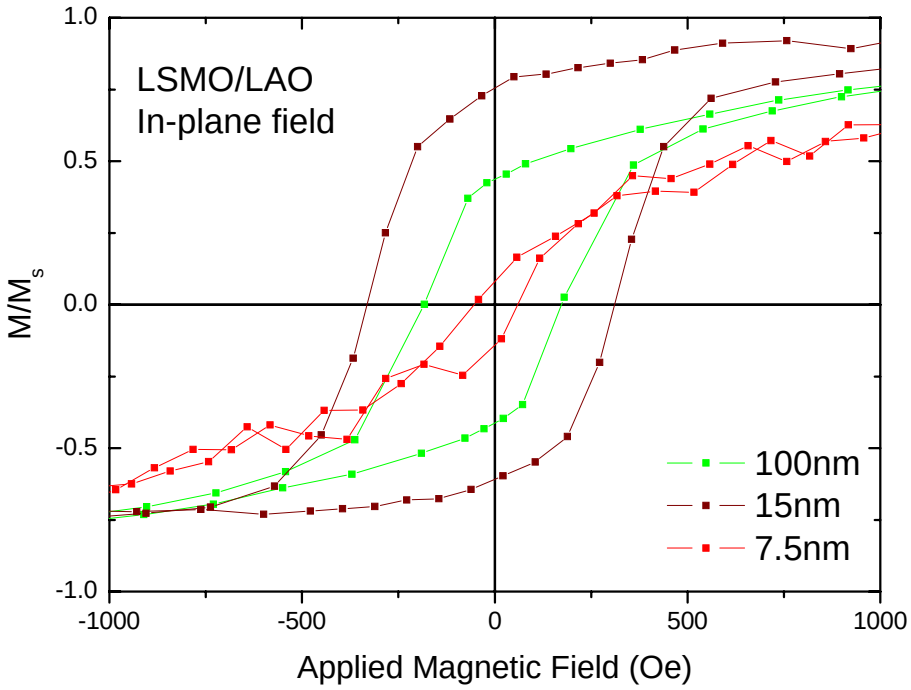

Figure 5-26 Normalized in-plane M-H loops of LSMO films with different thickness on LAO (001), measured at 80 K.

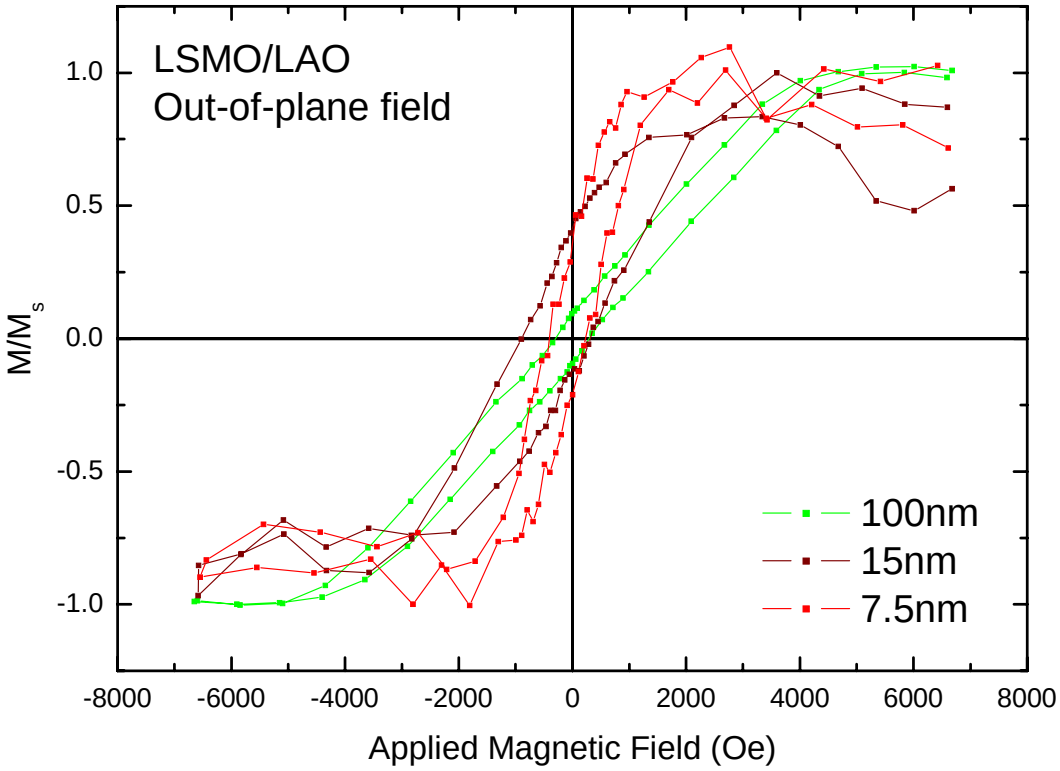

Figure 5-27 Normalized out-of-plane M-H loops of LSMO films with different thickness on LAO substrates at 80K.

`

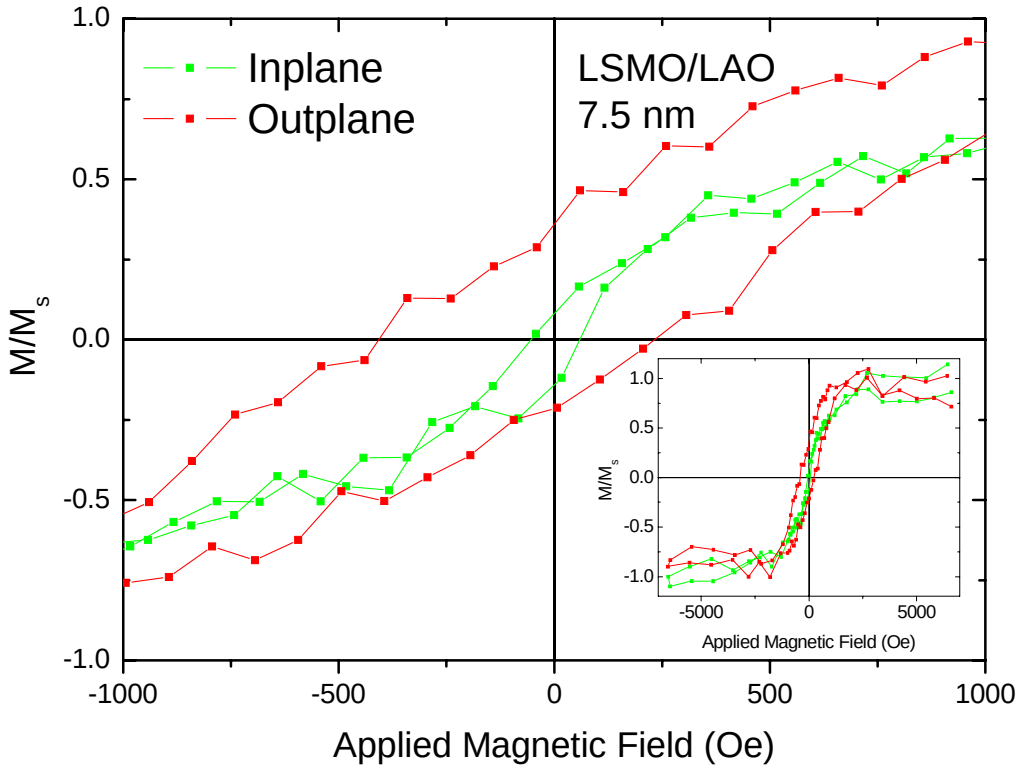

Figure 5-28 Normalized in-plane and out-of-plane hysteresis loops of a 7.5nm LSMO film on LAO substrate. Inset shows the M-H loops in enlarged field scale.

5.7 LNO on LAO (001) by LMBE

5.7.1 Anomalous temperature dependence of resistivity

From the inset of Figure.5.29, interestingly, it was observed that the resistivity of an oxygen-deficient LNO film fell to a minimum at 140 K, while the stoichiometric (or oxygen-balanced) LNO film showed metallic transport behavior (Figure5.29(b)). The deposition conditions of oxygen deficient and optimally deposited LNO film were identical except the post-deposition treatment: the optimally deposited LNO film was maintained in an oxygen ambient of 150 mTorr during the cooling process, while the oxygen-deficient

sample was cooled in the absence of oxygen after deposition.

Similar behavior has been found by Gayathri *et al* [5.20]. They studied the temperature dependence of electrical properties in bulk LNO ceramics with different oxygen content, and they claimed that an appearance of resistivity minima arises from the weak-localization effect. Further study has not been conducted in this work; however, it is noted that maintaining oxygen stoichiometry is an important issue for deposition of LNO thin films.

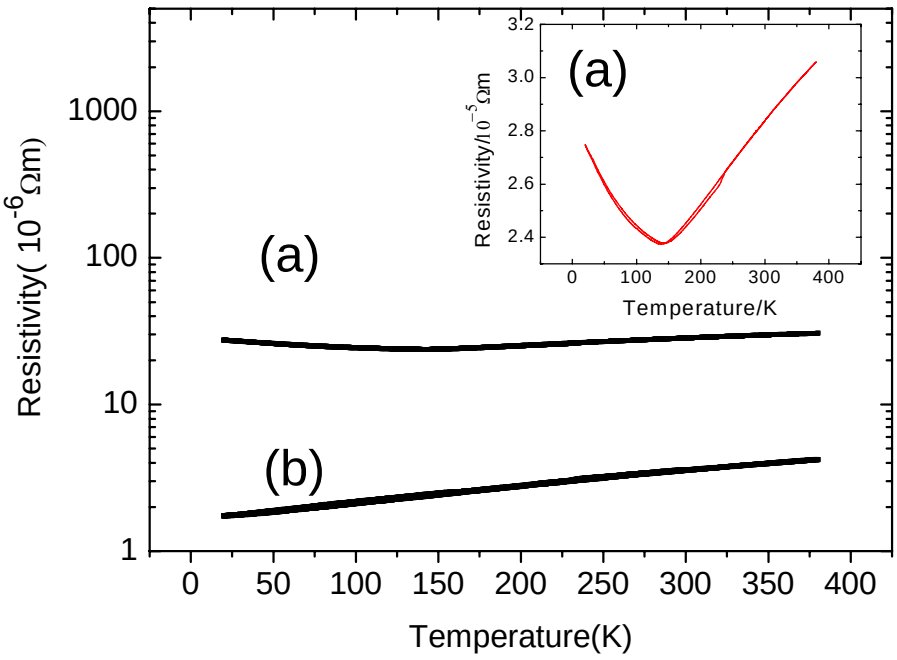

Figure 5-29 Semi-log plots of RT measurements for (a) oxygen deficient and (b) optimally grown LNO film deposited by LMBE. The inset shows the linear plot of (a).

5.8 Summary for deposition parameters and properties of perovskite thin films

Material	Deposition system	Laser fluence (J/cm^2)	Oxygen ambient (mTorr)	Base pressure (mTorr)	Target-to-substrate-distance (cm)	Substrate temperature (^oC)	Reprate rate (Hz)	Annealing time (secs)	Flow rate (sccm)
LSMO	PLD	3.82	150	~5	4	650	5	60	N/A
LNSMO	PLD	3.82	150	~5	4	650	5	60	N/A
LSMRO	PLD	3.82	150	~5	4	830	5	60	N/A
LNO	PLD	3.82	150	~5	4	650	5	60	N/A
LSMO	LMBE	5	188	$<5x10^{-2}$	5	680	5	60	20
LCMO	LMBE	5	188	$<5x10^{-2}$	5	680	5	60	20
LNO	LMBE	5	150	$<5x10^{-2}$	5	680	5	60	20

Table 5-1 Optimal deposition parameters for perovskite thin film by PLD and LMBE systems.

Material	Deposition system	Out-of-plane Lattice parameters (Å)	Full-Width-Half-Maximum (^{o})	R.M.S. roughness in scan area of 1 x 1 μm^2 (nm)	Resistivity at 20K (Ωm)	Resistivity at 300K (Ωm)	Coercive field (100 K) (Oe)	Magnetization (100 K) (μ_B/Mn ions)
LSMO	PLD	3.890	0.35	~1.1	$\sim 3x10^{-6}$	$\sim 3.2x10^{-5}$	130	3.03
LNSMO	PLD	3.859	0.32	~1.0	$3.30x10^{-6}$	$4.51x10^{-5}$	90	3.14
LSMRO	PLD	3.921	0.29	~6.6	$1.77x10^{-6}$	$2.52x10^{-5}$	260	3.16 (80K)
LNO	PLD	3.875	0.40	~1.3	$8.8x10^{-7}$	$2.32x10^{-6}$	N/A	Non magnetic
LSMO	LMBE	3.921	0.10	~1.0	$1.97x10^{-5}$	$1.25x10^{-4}$	120	undetermined
LCMO	LMBE	3.860	0.14	~1.0	$2.64x10^{-5}$	$\sim 4.77x10^{-5}$	95	undetermined
LNO	LMBE	3.868	0.08	~1.2	$1.73x10^{-6}$	$3.58x10^{-6}$	N/A	Non magnetic

Table 5-2 Properties of perovskite thin films deposited by PLD and LMBE systems.

Chapter 6 All-oxide pseudo spin valves in current-in-plane configuration

In this Chapter, I will present results obtained from perovskite oxide multilayers of structure LSMRO (100 nm)\LNO (15 nm)\LSMO (50 nm), deposited by PLD on (001) LAO single crystal substrates.

For the growth of single-phased epitaxial LSMRO films, precise optimization of oxygen pressure (P) and substrate temperature (T_{sub}) was necessary. Low P and high T_{sub} favours the intergrowth of Ru-deficient Sr_2RuO_4, whereas high P and low T_{sub} can lead to the growth of $SrRuO_3$ [6.1]. An oxygen pressure of 150 mTorr and a substrate temperature of 830^{o}C were finally chosen as optimal deposition conditions, as mentioned in Section.5.4. Due to the relatively high growth temperature of LSMRO (refer to previous chapter), it was deposited as the bottom layer of the spin valve stack in order to avoid interfacial diffusion. This was followed by the growth of LNO and LSMO layers at 650 °C.

The microstructures of the SV samples were characterized by XRD. Magnetic measurements were performed by VSM. Four-point magnetoresistance measurements, as mentioned in Section.4.3.3.2, in CIP geometry were done on the samples, with the magnetic field applied parallel to the film plane.

6.1 Microstructure

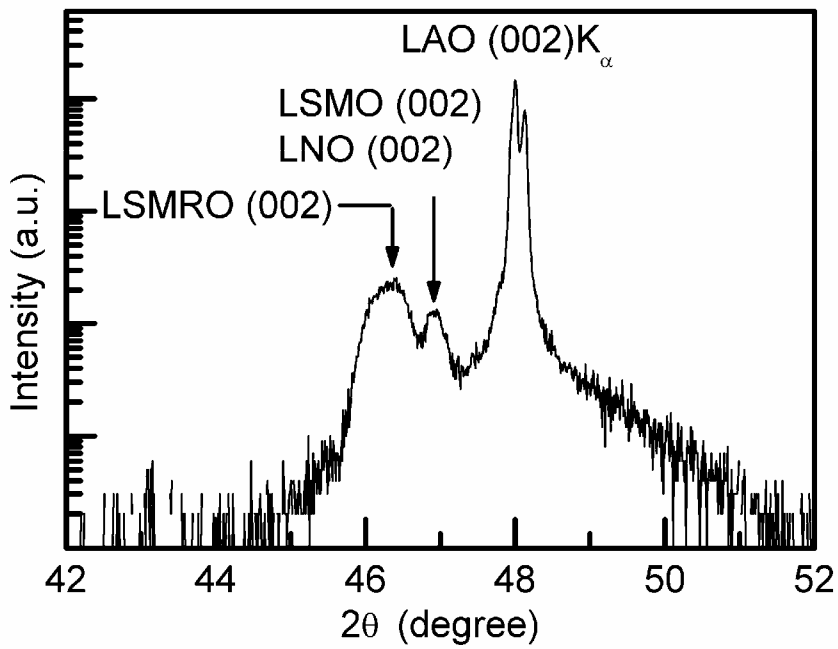

Figure 6-1 θ-2θ scan of a LSMRO\LNO\LSMO PSV multilayer sample.

The θ-2θ scan of a multilayer sample is displayed in Figure.6.1, indicating that all of the layers were highly (001)-oriented, with out-of-plane lattice constants of 3.91 Å (LSMRO) and 3.87 Å (LNO and LSMO). The LNO and LSMO peaks could not be resolved from the scan, which is similar to our previous observations on epitaxially-grown LNO\LSMO films [6.2]. The values of lattice constants obtained from Figure.6.1 are similar to those of the bulk materials (a_{LSMRO} = 3.86 Å, a_{LNO} = 3.84 Å, a_{LSMO} = 3.87 Å, assuming pseudo-cubic structures). The higher value of a_{LSMRO} could be understood as a consequence of elastic distortion of the larger unit cells, in order to conform to an

epitaxial growth on LAO substrate (a_{LAO} = 3.79 Å). On the other hand, rocking curve measurements corresponding to LSMRO and LNO\LSMO peaks revealed FWHM values of ~ 0.6° (data not shown), indicating the epitaxial nature of the samples.

Concerning the LSMRO layer, we have not observed any diffraction peaks other than the LSMRO(002) peak in Figure.6.1, suggesting the absence of phases other than LSMRO, down to the detection limit of the diffractrometer..

6.2 Magnetic Measurements

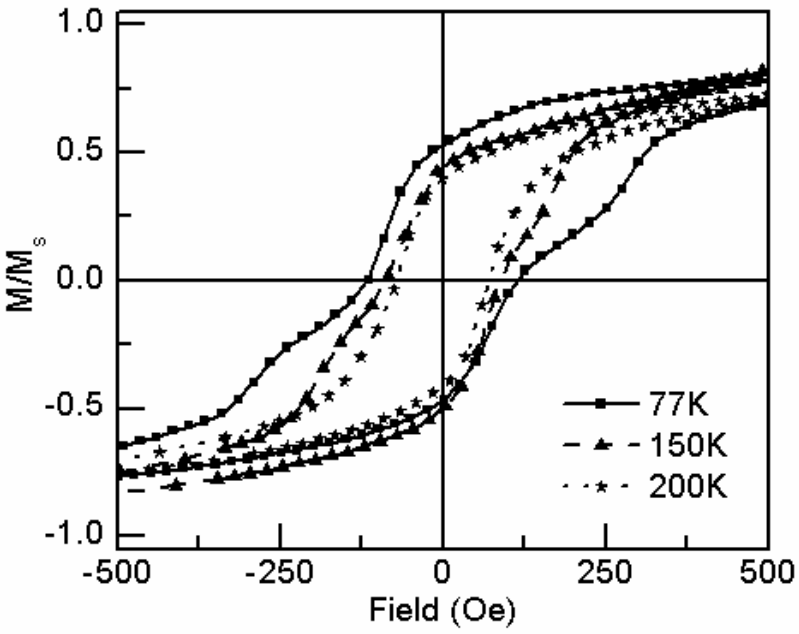

Figure 6-2 Hysteresis loops of a pseudo spin valve sample at various temperatures.

Figure.6.2 shows the in-plane hysteresis loops of the PSV structure at various temperatures. At 77 K, a double coercivity behavior was clearly observed.

The corresponding coercivity values were 80 and 280 Oe. These results matched quite well with values obtained from single LSMO (Section.5.2) and LSMRO layers (Section.5.4), respectively. We therefore attribute the switching at ±80 Oe to the reversal of LSMO layer, and that at ±280 Oe to the LSMRO layer switching. The coercivity contrast was suppressed as the temperature increased; the double coercivity behavior was no longer observed at temperatures above 200 K.

6.3 Transport Measurement

Magnetotransport properties of the PSV structure at 10 K is shown in Figure.6.3(b1) and (b2). In order to distinguish GMR from AMR effect, MR measurements were performed with the external field applied either parallel or perpendicular to the current flow direction. As observed in Figure 6.3(b1) and (b2), a negative MR behavior was observed; that is, a high resistance state was observed at the low magnetic field regime.

Closer inspection of Figure.6.3(b) reveals that the MR plots are superposition of two separate MR curves (Figure.6.3(a) and Figure.6.3(c)), clearly indicating that the current was flowing through all of the layers in the CIP device. From Figure.6.3(b), MR peaks were observed between ±150 Oe at low magnetic field. The sign of this MR peak was unchanged, when the relative

orientations between the applied field and current was switched by 90°. The independence of this MR peak to the relative orientation between current and magnetization is similar to the behaviour of single LSMO layer (Figure.6.3(c)).

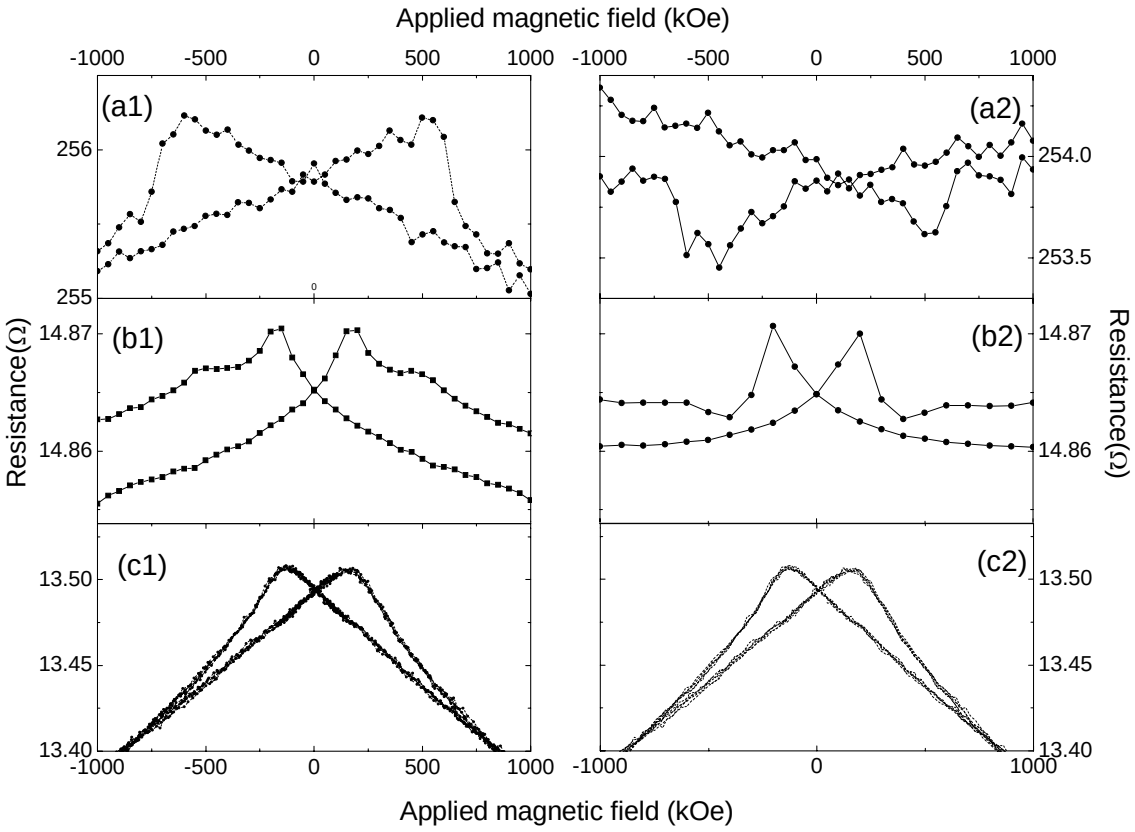

Figure 6-3 In-plane magnetoresistance measurements of (a) LSMRO single layer on LAO at 10 K, (b) CIP device at 10 K and (c) LSMO on LAO at 20 K. (a1) and (b1) have applied current perpendicular to the field, while (a2) and (b2) have applied current parallel to the field. (c1) and (c2) are the same graph because the magnetoresistive behavior of single layer LSMO is independent to the relative orientation between applied current and field.

At higher fields (up to ±600 Oe), a broad MR background was observed. Unlike the low-field MR peaks, this 'background' MR behavior changed sign when the in-plane field was rotated by 90°. The changed sign corresponds to the AMR effect shown by single layer LSMRO as described in Figure.6.3(a).

Although the MR measurements of single layer LSMO was performed at 20 K, it was expected that the MR of single LSMO layer will behave in the same way at 10 K, with the peaks at about the same positions. It seems that the magnetoresistive effect of the CIP device is the combination of AMR of LSMRO film and inter-granular tunneling of LSMO single layer.

6.4 Discussions

The aim of this project was to fabricate PSV structures. While I have demonstrated the double coercivity behavior in the as-deposited films (Figure.6.2), but it cannot be concluded that GMR effect was observed in Figure.6.3(a) solely based on the measurements shown here.

From the results of Figure.6.3(b), one may suggest that the low-field MR peaks were due to the GMR effect. At low magnetic field, the magnetization of the LSMO layer was switched, leading to a high resistance state. As the field was further increased, the LSMRO starts to reverse, leading to a drop in the resistance of the multilayer. As the field was further increased, the AMR effect of LSMRO dominated the MR behavior.

The fallacy of the above picture is as follows. The coercivity of LSMRO at 10 K, as seen from Figure.6.3(b), should be around 500 to 700 Oe. This is much higher than the value of ~ 250 Oe, at which the resistance of the low field MR

peaks in Figure.6.3(b) started to drop. Unless supported by magnetization measurement at the same temperature, one cannot conclude that the observed low-field MR behavior in Figure.6.3(a) was due to the GMR effect of the spin valve structure.

In Figure.6.3(c) I showed the MR behavior (intergranular tunneling) of a sample LAO(001)\LSMO(50 nm), measured at 20 K. It has portrayed a broad MR behavior, with switching fields that matched fairly well with the low field MR peaks in Figure.6.3(b). The data shown in Figure.6.3(c) further shows the MR behavior was independent to the relative orientation between applied current and field. Qualitatively, however, the sharp switching behavior of low-field MR in Figure.6.3(b) did not seem to match the broad reversal behaviour in Figure.6.3(c). Further investigations are therefore necessary to clarify the origin of the observed MR behavior in Figure.6.3(b).

One strategy to resolve the issue is to provide conditions that are conducive for the exhibition of GMR effect; this can be achieved by reducing the spacer layer thickness. Indeed, Granada *et al.* [6.3] have shown that the CIP GMR would be too small to be observed, once the LNO spacer thickness was above 8 nm. This is partly due to the high resistivity of LNO, which leads to a small carrier mean free path and adversely affect the MR ratio obtained [6.4]. In order

to observe the GMR effect, thinner LNO spacers will be deposited while trying to maintain a double coercivity behaviour.

On the other hand, the PSV structure shown in this work could possibly demonstrate GMR effect in the CPP geometry: in such a case, the spin diffusion length of charge carriers inside the spacer is the relevant length parameter [6.5]. In general the spin diffusion length is much longer than the electronic mean free path, at least in the case of metals [6.6]; no information about spin diffusion length in LNO was found in literature. Work is under progress along this direction.

6.5 Conclusion

I have fabricated epitaxial PSV structures, using various conducting perovskite oxides. In particular, coercivity contrast in ferromagnetic layers was achieved by using LSMO with or without Ru doping. Further attempts will be made to fabricate samples with thinner LNO spacers, in order to realize GMR in such a structure. Measurements will also be made in the CPP geometry, with the aim of extracting relevant spin transport parameters (such as spin diffusion length) in LNO. Successful probing of such parameters using the SV structure described here would serve as a protocol for further investigations of spin transport in other oxide systems.

Chapter 7 Magnetic properties of LSMO\LNO\LCMO pseudo spin valves by LMBE

7.1 Introduction

After the characterization of LSMRO single layers (Chapter 5) and measurements of CIP devices (previous chapter), it was found that LSMRO thin films were hardly reproduced in the both PLD and LMBE systems. The difficulty in reproducing LSMRO thin films was also mentioned elsewhere [7.1]. In order to obtain repeatable results, LSMO and LCMO were chosen as the ferromagnetic electrodes in PSV.

Microstructural analysis and magnetic characterization of LNO (200 nm)\LSMO (50 nm)\LNO (10 nm)\LCMO (25 nm) multilayer structure are presented in this Chapter. The PSV structure was deposited on single crystalline LAO substrates. The thick bottom LNO layer serves as the electrode, and the multilayer structure (LSMO/LNO/LCMO) on top forms the PSV structure. LNO bottom electrode was used instead of the LSMO layer in PSV, because this can minimize AMR contribution to the MR measurement. Like the CIP devices in Chapter 6, it was necessary to prepare two different ferromagnetic electrodes in the PSV with well-defined anti-parallel magnetic state, in order to produce reproducible step-like GMR [7.2].

Such multilayer stacks were deposited for the purpose of fabricating CPP devices, using a 3-D focused ion beam etching technique [7.3]. Such a process not only provides a simple means for fabricating CPP devices, but also small junctions (lateral dimensions < 200 nm) can be prepared to enhance magnetoresistive effect. This part of the work is pursued in collaboration with the Device Materials Group in Cambridge University, and is under progress at the time this thesis was submitted.

In this chapter, only measurements on the microstructural and magnetic properties of the multilayer will be given. Device fabrication and magnetoresistance measurements are under progress, and will be part of the future work.

7.2 Microstructure

XRD θ-2θ pattern of a multilayer stack sample is illustrated in Figure.7.1, showing that all the layers were highly (002)-oriented with out-of-plane lattice parameters of 3.82 Å (LCMO) and 3.87 Å (LNO and LSMO). Similar to the result on highly-textured LNO\LSMO bilayer on LAO substrates [7.4], the LNO and LSMO peaks could not be distinguished from each other in the scan. The peak at 47.5^{o} in Figure.7.1 was considered to be from the LCMO layer. As summarized in Table.5.2, the lattice parameter of LCMO on LAO was 3.86 Å.

The change of the out-of-plane lattice constant was attributed to compressive stress relaxation (Section.2.7) produced by the stack of layers (LNO\LSMO\LNO) beneath the LCMO layer. The values of lattice constants obtained from Figure.7.1 were found to match closely with those of the materials in bulk form (a_{LCMO} = 3.86 Å, a_{LNO} = 3.84 Å, a_{LSMO} = 3.87 Å, assuming pseudo-cubic structures). Apart from the θ-2θ pattern, rocking curve measurements and ϕ scan of the layers (data not shown) further unveiled that the sample was highly-oriented (FWHM values of LSMO/LNO and LCMO were ~0.8^o and ~1^o, respectively), and was grown cube-on-cube relationship on the substrate.

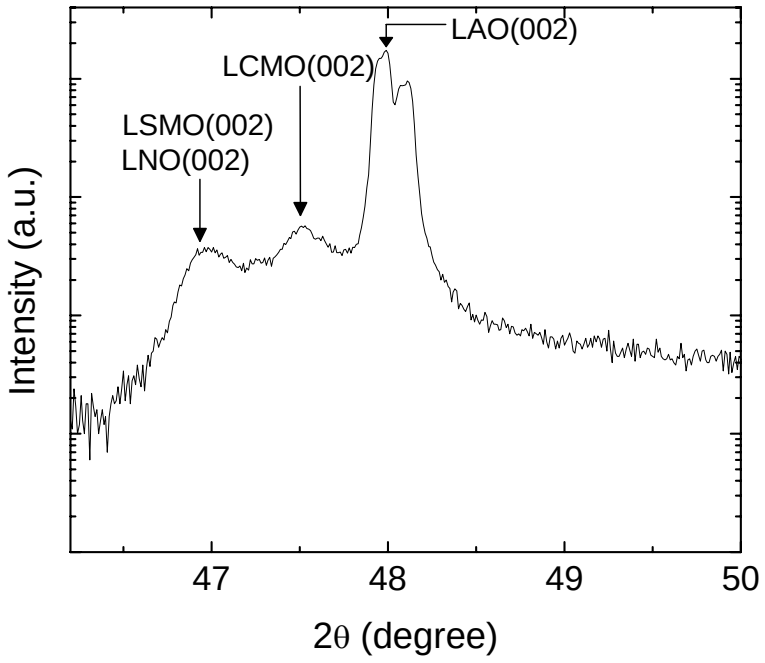

Figure 7-1 XRD θ-2θ pattern of a LNO\LSMO\LNO\LCMO sample.

7.3 Magnetic properties

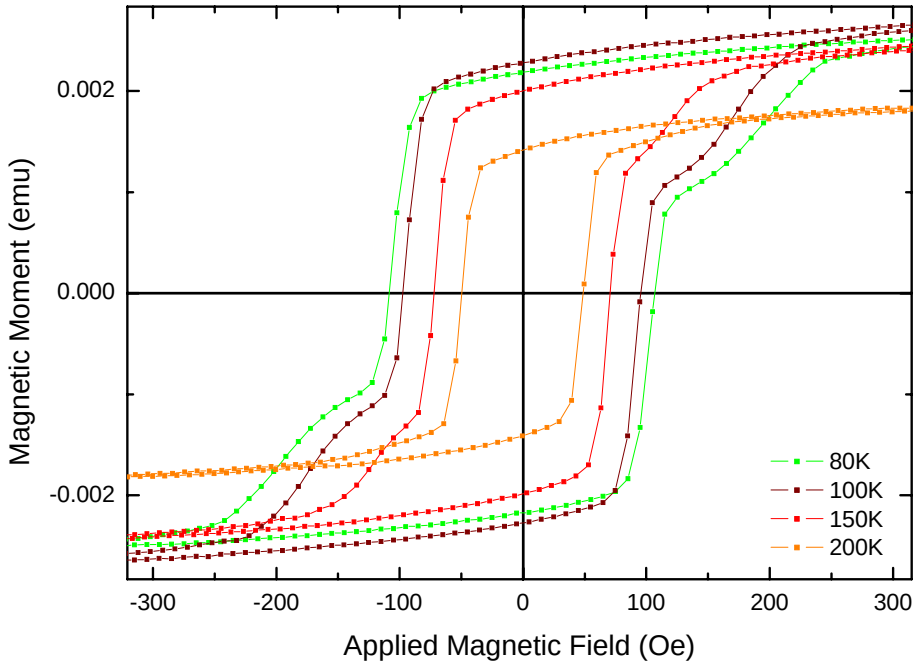

Figure 7-2 In-plane hysteresis loops of the multilayer at various temperatures.

Figure.7.2 displays the temperature dependence of MH measurements of the same multilayer sample used for XRD measurements. Double coercivity behavior was clearly shown at temperatures lower than 200 K, and the effect was more pronounced with decreasing temperatures. At 200 K and above, double coercivity could no longer be detected. There are a number of possibilities for explaining such a suppression of double coercivity behavior. The first one was that the coercivity contrast was no longer large enough to be detected by our VSM at 200 K and above. The disappearance of the effect could also be ascribed to the fact that the temperature at 200 K was very close to the Curie temperature (250 K) of the LCMO layer. This resulted in a very weak signal from the LCMO

layer. It should be stressed that the two effects are not mutually exclusive. However, it seems that the latter was more dominant, as LCMO on LAO samples (Chapter 5) have signals that were already too weak to be detected above 200 K.

The identification of the LSMO and LCMO layers can be done by the relative strengths of magnetization. As the LSMO layer was two times thicker than LCMO layer, the magnetization signals of the LSMO layer was also two times that of the LCMO film as the two materials have similar magnetization at low temperature. This can be observed clearly from Figure 7.2, for the M-H loop at 80 K. Based on this, I deduced that the switching at ±190 Oe (at 80 K) correspond to the LCMO layer, and the magnetization reversal at ~±100 Oe (at 80 K) correspond to the LSMO. This matched well with the results obtained from the LSMO single layer on LAO (Figure.5.7).

7.4 Conclusion

I have deposited PSV structures for fabricating CPP devices with different perovskite oxides. Microstructural analysis and MH measurements were performed. Coercivity contrast between the ferromagnetic electrodes was established, by means of two kinds of A-site doped lanthanum manganites. The deposited structures will be fabricated into CPP devices by focused ion beam etching, followed by magnetotransport measurements to verify the presence of

GMR effect. Further work will be made to estimate the spin transport parameters (e.g.spin diffusion length) of LNO spacers. Promising results of such parameters would suggest possibilities of using LNO layer in oxide spin electronics system.

Chapter 8 Conclusions

In the experimental study, I have presented two parts of results. One of them is the optimization of deposition parameters for single layered films. Another one is about properties of two types of devices, one in the CIP geometry and the other one for CPP measurements.

After precise optimization of deposition parameters, such as substrate-to-target distances, laser fluence, repetition rate and oxygen pressure, thin films with extremely flat surfaces and high crystallinity were obtained. Two PLD systems were utilized for depositing thin films in this project, one was a typical PLD system and the other one was a laser molecular beam epitaxy system (LMBE). Compared with PLD, LMBE can produce single crystalline films with atomic flatness due to a slower growth process. Experimental results showed that the roughness (r.m.s ~ 1 nm) and crystallinity (FWHM ~ 0.2° obtained from ω-scan) of the films fabricated by LMBE were superior to those produced by PLD (roughness r.m.s ~ 1nm and FWHM ~ 0.5). All properties and deposition parameters of thin films were summarized in Chapter 5.

CIP devices were fabricated in PSV structures LSMRO (100 nm)\ LNO (15 nm)\LSMO (50 nm). Ru doping in LSMO has been shown to induce coercivity enhancement of 2.5 times compared to that of LSMO (~100 Oe at 80 K). Double

coercivity was clearly observed in these devices. Magnetoresistance measurements were performed on the device at 10 K and the results showed that the magnetoresistive effect of the CIP device was the combination of AMR of LSMRO film and intergranular tunneling of LSMO layer.

LSMO (50 nm)\ LNO (15 nm)\LCMO (25 nm) PSVs, prepared to be fabricated into CPP devices, with LNO as bottom electrodes, were deposited on LAO substrates. Microstructure analysis showed the epitaxial nature of the films, and hysteresis loop measurements illustrated two-step switching (double coercivity) characteristic of the heterostructures. It was found that the one switching corresponded to LCMO and another one to LSMO.

A very similar work was found in the literature, in which La0.75Sr0.25MnO3/LNO/La0.75Sr0.25MnO3 CIP device was fabricated and claimed to exhibit GMR effect [8.1]. However, verification of the GMR could not be made possible without considering two crucial factors: (1) double coercivity effect, which was not clearly observed in their work. (2) angular measurements for MR were not done to eliminate contributions of AMR effect. In contrast, the device mentioned in Chapter 7 clearly showed double coercivity. Clearer verification of GMR can be made, if our device can demonstrate large MR changes through magnetization switching between parallel and antiparallel

states.

One of the issues investigated in the current project was the coercivity contrast between ferromagnetic layers in PSV, with the aim of demonstrating step-like GMR. Based on current results, MR response of the devices mentioned in Chapter 7 will be studied, in order to observe GMR in such structure. Successful demonstration of GMR would be the first work to show GMR in PSV with LNO as spacer, when the work by Granada *et al* did not provide enough evidences for the existence of GMR in a similar structure. Another interesting extension of this work is to probe experimentally the spin diffusion length of LNO. Such information will clarify the potential of using LNO as electrodes in spintronic devices using perovskite oxides. Successful preparation of the devices mentioned would serve as a protocol for further studies of spin manipulation in other oxide systems.

References

[1.1] M. Tsoi, A. G. M. Jansen, J. Bass, W. Chiang, M. Seck, V. Tsoi and P. Wyder, "Excitation of a Magnetic Multilayer by an Electric Current", *Phys. Rev. Lett.*, vol. 80, pp. 4281, 1998.

[1.2] J. A. Katine, F. J. Albert, R. A. Buhrman, E. B. Myers and D. C. Ralph, "Current-Driven Magnetization Reversal and Spin-Wave Excitations in Co /Cu /Co Pillars", *Phys. Rev. Lett.*, vol. 84, pp. 3149, 2000.

[1.3] J. Grollier, V. Cros, A. Hamzic, J. M. George, H. Jaffres, A. Fert, G. Faini, J. B. Youssef and H. Legall, "Spin-polarized current induced switching in Co/Cu/Co pillars", *Appl. Phys. Lett.*, vol. 78, pp. 3663-3665, 2001.

[1.4] S. M. Thompson, "The discovery, development and future of GMR: The Nobel Prize 2007", *J. Phys. D*, vol. 41, pp. 093001, 2008.

[1.5] A. Cho, "NOBEL PRIZES: Effect that Revolutionized Hard Drives Nets a Nobel", *Science*, vol. 318, pp. 179, 2007.

[1.6] GerstnerEd, "Nobel Prize 2007: Fert and Grunberg", *Nat. Phys.*, vol. 3, pp. 754-754, 2007.

[1.7] M. N. Baibich, J. M. Broto, A. Fert, F. N. Van Dau, F. Petroff, P. Eitenne, G. Creuzet, A. Friederich and J. Chazelas, "Giant Magnetoresistance of (001)Fe/(001)Cr Magnetic Superlattices", *Phys.Rev.Lett.*, vol. 61, pp. 2472-2475, 1988.

[1.8] G. Binasch, P. Grnberg, F. Saurenbach and W. Zinn, "Enhanced magnetoresistance in layered magnetic structures with antiferromagnetic interlayer exchange", *Phys.Rev.B*, vol. 39, pp. 4828-4830, 1989.

[1.9] E. Favre-Nicolin, L. Ranno, C. Dubourdieu and M. Rosina, "Spin-dependent tunnelling in $La_{0.7}Sr_{0.3}MnO_3/SrTiO_3$ superlattices", *Thin Solid Films*, vol. 400, pp. 165-168, 2001.

[1.10] Y. Ogimoto, M. Izumi, A. Sawa, T. Manako, H. Sato, H. Akoh, M. Kawasaki and Y. Tokura, "Tunneling Magnetoresistance above Room Temperature in $La_{0.7}Sr_{0.3}MnO_3/SrTiO_3/La_{0.7}Sr_{0.3}MnO_3$ Junctions", *Jpn. J. Appl. Phys*, vol. 42, pp. L369, 2003.

[1.11] P. Shakya, P. Desai, T. Kreouzis and W. P. Gillin, "Magnetoresistance in triphenyl-diamine derivative blue organic light emitting devices", *J. Appl. Phys.*, vol. 103, pp. 043706, 2008.

[1.12] J. D. Bergeson, V. N. Prigodin, D. M. Lincoln and A. J. Epstein, "Inversion of Magnetoresistance in Organic Semiconductors", *Phys. Rev. Lett.*, vol. 100, pp. 067201, 2008.

[1.13] W. Raberg and A. Gupta, "Materials Requirements for Magnetic Random-Access Memory (MRAM) Devices", *Thin Films and Heterostructures for Oxide Electronics*, pp. 129-151, 2005.

[1.14] J. C. Slonczewski, "Current-driven excitation of magnetic multilayers", *Journal of Magnetism and Magnetic Materials*, vol. 159, pp. L1-L7, 1996.

[1.15] J. Guo, M. B. A. Jalil and S. G. Tan, "Current-induced magnetization excitation in a pseudo-spin-valve with in-plane anisotropy", *Appl. Phys. Lett.*, vol. 92, pp. 182103, 2008.

[1.16] T. Inokuchi, H. Sugiyama, Y. Saito and K. Inomata, "Current-induced magnetization switching under magnetic field applied along the hard axis in MgO-based magnetic tunnel junctions", *Appl. Phys. Lett.*, vol. *89*,pp. 102502, 2006.

[1.17] S. Lepadatu, J. Wu and Y. B. Xu, "Current-induced magnetization switching in asymmetric necked wires", *Appl. Phys. Lett.*, vol. 91, pp. 062512, 2007.

[1.18] J. Wegrowe, S. M. Santos, M. Ciornei, H. Drouhin and J. M. Rubi, "Magnetization reversal driven by spin injection: A diffusive spin-transfer effect", *Phys. Rev. B*, vol. 77, pp. 174408, 2008.

[1.19] F. J. Albert, N. C. Emley, E. B. Myers, D. C. Ralph and R. A. Buhrman, "Quantitative Study of Magnetization Reversal by Spin-Polarized Current in Magnetic Multilayer Nanopillars", *Phys.Rev.Lett.*, vol. 89, pp. 226802, 2002.

[1.20] S. I. Kiselev, J. C. Sankey, I. N. Krivorotov, N. C. Emley, R. J. Schoelkopf, R. A. Buhrman and D. C. Ralph, "Microwave oscillations of a nanomagnet driven by a spin-polarized current", *Nature*, vol. 425, pp. 380-383, 2003.

[1.21] O. Boulle, V. Cros, J. Grollier, L. G. Pereira, C. Deranlot, F. Petroff, G. Faini, J. Barnas and A. Fert, "Shaped angular dependence of the spin-transfer torque and microwave generation without magnetic field", *Nat. Phys.*, vol. 3, pp. 492-497, 2007.

[1.22] D. R. Baselt, G. U. Lee, M. Natesan, S. W. Metzger, P. E. Sheehan and R. J. Colton, "A biosensor based on magnetoresistance technology", *Biosensors and Bioelectronics*, vol. 13, pp. 731-739, 1998.

[1.23] M. Megens and M. Prins, "Magnetic biochips: a new option for sensitive diagnostics", *Journal of Magnetism and Magnetic Materials*, vol. 293, pp. 702-708, 2005.

[1.24] Nature Publishing Group, "Nature Milestones Timeline in Spin", from Nature Pubishing Group website: http://www.nature.com/milestones/milespin/timeline.html. 2008.

[1.25] R. R. Gatazka, *Proceedings of the 14th International Conference on the Physics of Semiconductors*, vol. 43, pp. 133-140, 1978.

[1.26] S. A. Chambers, "A potential role in spintronics", *Materials Today*, vol. 5, pp. 34-39, 2002.

[1.27] D. D. Awschalom, M. E. Flatté and N. Samarth, "SPINTRONICS", *Sci. Am.*, vol. 286, pp. 66, 2002.

[1.28] C. Chappert, A. Fert and Van Dau, Frederic Nguyen, "The emergence of spin electronics in data storage", *Nat. Mater.*, vol. 6, pp. 813-823, 2007.

[1.29] D. Grundler, "Spintronics", *Phys. World*, pp. 39, Apr 2002.

[1.30] V. A. Ivanov, T. G. Aminov, V. M. Novotortsev and V. T. Kalinnikov, "Spintronics and spintronics materials", *Russian Chemical Bulletin*, vol. 53, pp. 2357-2405, 2004.

[1.31] D. J. Palmer, "Silicon and spintronics, together at last: Electronic materials", *Materials Today*, vol. 10, pp. 9, 2007.

[1.32] S. D. Sarma, "Spintronics", *Am. Sci.*, vol. 89, pp. p516, 2001.

[1.33] R. A. de Groot, F. M. Mueller, P. G. v. Engen and K. H. J. Buschow, "New Class of Materials: Half-Metallic Ferromagnets", *Phys. Rev. Lett.*, vol. 50, pp. 2024-2027, 1983.

[1.34] L. J. Singh, C. W. Leung, C. Bell, J. L. Prieto and Z. H. Barber, "Magnetoresistance of spin valve structures based on the full Heusler alloy Co_2MnSi", *J. Appl. Phys.*, vol. 100, pp. 013910, 2006.

[1.35] J. ark, E. Vescovo, H. Kim, C. Kwon, R. Ramesh and T. Venkatesan, "Direct evidence for a half-metallic ferromagnet", *Nature*, vol. 392, pp. 794-796, 1998.

[1.36] A. Anguelouch, A. Gupta and G. Xiao, "Thickness dependence of magnetic and transport properties of chromium dioxide (CrO_2) strained epitaxial thin films", *IEEE Transactions on Magnetics*, vol. 37, pp. 2135-2137, 2001.

[1.37] Q. Zhao, J. J. Yuan, G. H. Wen and G. T. Zou, "Preparation and magnetoresistance of thin CrO_2 films", *Journal of Magnetism and Magnetic Materials*, vol. 320, pp. 2356-2358, 2008.

[1.38] L. V. Hau, "Quantum physics: Tangled memories", *Nature*, vol. 452, pp. 37-38, 2008.

[1.39] F. Kuemmeth, S. Ilani, D. C. Ralph and P. L. McEuen, "Coupling of spin and orbital motion of electrons in carbon nanotubes", *Nature*, vol. 452, pp. 448-452, 2008.

[1.40] J. R. Hauptmann, J. Paaske and P. E. Lindelof, "Electric-field-controlled spin reversal in a quantum dot with ferromagnetic contacts", *Nat. Phys.*, vol. 4, pp. 373-376, 2008.

[1.41] M. Bibes and A. Barthelemy, "Oxide Spintronics", *IEEE Transactions on Electron Devices*, vol. 54, pp. 1003-1023, 2007.

[1.42] W J M Naber,S Faez and W G van der Wiel, "Organic spintronics", *J. Phys. D*, vol. 40, pp. R205-R228, 2007.

[1.43] S. Datta and B. Das, "Electronic analog of the electro-optic modulator", *Appl. Phys. Lett.*, vol. 56, pp. 665-667, 1990.

[1.44] H. Yamada, M. Kawasaki and Y. Tokura, "Ru-doped $La_{0.6}Sr_{0.4}MnO_3$ thin films as a coercivity tunable electrode for magnetic tunnel junctions", *Appl. Phys. Lett.*, vol. 86, pp. 192505, 2005.

[1.45] Y. Ishii, H. Yamada, H. Sato, H. Akoh, M. Kawasaki and Y. Tokura, "Perovskite manganite magnetic tunnel junctions with enhanced coercivity contrast", *Appl. Phys. Lett.*, vol. 87, pp. 022509, 2005.

[1.46] L. M. Wang, J. Lai, J. Wu, Y. Kuo and C. L. Chang, "Effects of Ru substitution for Mn on $La_{0.7}Sr_{0.3}MnO_3$ perovskites", *J. Appl. Phys.*, vol. 102, pp. 023915, 2007.

[1.47] W. B. Wu, K. H. Wong, C. L. Choy and Y. H. Zhang, "In situ oxygen control and high thermal stability of epitaxial $(La_{1-x}Nd_x)_{0.7}Sr_{0.3}MnO_3$ films fabricated by pulsed laser deposition", *Thin Solid Films*, vol. 389, pp. 56-61, 2001.

[1.48] W. Wu, K. H. Wong, X. -. Li, C. L. Choy and Y. H. Zhang, "Effect of annealing in reduced oxygen pressure on the electrical transport properties of epitaxial thin film and bulk $(La_{1-x}Nd_x)_{0.7}Sr_{0.3}MnO_3$", *J. Appl. Phys.*, vol. 87, pp. 3006-3010, 2000.

[2.1] G.H. Jonker and J.H. Van Santen, "Ferromagnetic compounds of manganese with perovskite structure", *Physica*, vol. 16, pp. 337-349, 1950.

[2.2] M. B. Salamon and M. Jaime, “The physics of manganites: Structure and transport”, *Rev. Mod. Phys.*, vol. *73*, pp. 583, 2001.

[2.3] L. P. Gor'kov and V. Z. Kresin, "Mixed-valence manganites: fundamentals and main properties", *Physics Reports*, vol. 400, pp. 149-208, 2004.

[2.4] E. Dagotto and A. Moreo, "Theory of manganites: key role of intrinsic inhomogeneities", *J Magn Magn Mater*, vol. 226-230, pp. 763-768, 2001.

[2.5] Jiandi Zhang, F Ye, Hao Sha, Pengcheng Dai,J A Fernandez-Baca and E W Plummer, "Magnons in ferromagnetic metallic manganites", *Journal of Physics: Condensed Matter*, vol. 19, pp. 315204, 2007.

[2.6] A. Haghiri-Gosnet and J. Renard, "CMR manganites: physics, thin films and devices", *J. Phys. D*, vol. 36, pp. R127, 2003.

[2.7] A. R. Bishop and H. Roder, "Theory of colossal magnetoresistance", *Current Opinion in Solid State and Materials Science,* vol. 2, pp. 244-251, 1997.

[2.8] E. Dagotto, T. Hotta and A. Moreo, "Colossal magnetoresistant materials: the key role of phase separation", *Physics Reports,* vol. 344, pp. 1-153, 2001.

[2.9] Y. Motome, N. Furukawa and N. Nagaosa, "An Origin of CMR: Competing Phases and Disorder-Induced Insulator-to-Metal Transition in Manganites", *Lecture Notes In Physics,* vol. 678, pp. 71, 2005.

[2.10] E. L. Nagaev, "Colossal-magnetoresistance materials: manganites and conventional ferromagnetic semiconductors", *Physics Reports,* vol. 346, pp. 387-531, 2001.

[2.11] W. Prellier, P. Lecoeur and B. Mercey, "Colossal-magnetoresistive manganite thin films", *Journal of Physics: Condensed Matter,* vol. 13, pp. R915-R944, 2001.

[2.12] Y. Tokura, "Critical features of colossal magnetoresistive manganites", *Reports on Progress in Physics,* vol. 69, pp. 797-851, 2006.

[2.13] J. Park, E. Vescovo, H. Kim, C. Kwon, R. Ramesh and T. Venkatesan, "Direct evidence for a half-metallic ferromagnet", *Nature,* vol. 392, pp. 794-796, 1998.

[2.14] R. Meservey and P. M. Tedrow, "Spin-polarized electron tunneling", *Physics Reports,* vol. 238, pp. 173-243, 1994.

[2.15] J. H. Song, J. Park, J. Kim, B. Park, Y. H. Jeong, H. Noh, S. Oh, H. Lin and C. T. Chen, "Spin-orbit-lattice coupling and magnetostriction of strained $La_{0.7}Ca_{0.3}MnO_3$ films", *Phys. Rev. B,* vol. 72, pp. 060405, 2005.

[2.16] Y. Tokura, "Correlated-Electron Physics in Transition-Metal Oxides", *Phys Today,* vol. 56, pp. 50, 2003.

[2.17] Y. Tokura and N. Nagaosa, "Orbital Physics in Transition-Metal Oxides", *Science,* vol. 288, pp. 462-468, 2000.

[2.18] C. Zener, "Interaction between the d-Shells in the Transition Metals. II. Ferromagnetic Compounds of Manganese with Perovskite Structure", *Phys. Rev.,* vol. 82, pp. 403-405, 1951.

[2.19] C. J. Ballhausen, *Introduction to Ligand Field Theory.* McGraw-Hill, 1962,

[2.20] H. A. Jahn and E. Teller, "Stability of Polyatomic Molecules in Degenerate Electronic States. I. Orbital Degeneracy", *Proceedings of the Royal Society of London.Series A, Mathematical and Physical Sciences (1934-1990),* vol. 161, pp. 220-235, 1937.

[2.21] J. M. D. Coey, M. Viret and S. V. Molnar, "Mixed-valence manganites", *Adv. Phys.*, vol. 48, pp. 167-293, 1999.

[2.22] J. Klein, J. B. Philipp, D. Reisinger, M. Opel, A. Marx, A. Erb, L. Alff and R. Gross, "Orbital order and anisotropic transport properties in doped manganites induced by epitaxial coherency strain", *J. Appl. Phys.*, vol. 93, pp. 7373-7375, 2003.

[2.23] B. Vertruyen, R. Cloots, M. Ausloos, J. -. Fagnard and P. Vanderbemden, "Unusual resistivity hysteresis in a bulk magnetoresistive ferromagnetic/ferrimagnetic composite ($La_{0.7}Ca_{0.3}MnO_3/Mn_3O_4$): Role of demagnetization effects", *Appl. Phys. Lett.*, vol. 91, pp. 062514, 2007.

[2.24] M. Ziese and S. P. Sena, "Anisotropic magnetoresistance of thin $La_{0.7}Ca_{0.3}MnO_3$ films", *Journal of Physics: Condensed Matter,* vol. 10, pp. 2727-2737, 1998.

[2.25] L. J. van der Pauw, "A Method of Measuring the Resistivity and Hall Coefficient on Lamellae of Arbitrary Shape", *Philips Tech. Rev.*, vol. 20, pp. 220-4, 1958.

[2.26] P. W. Anderson, "Antiferromagnetism. Theory of Superexchange Interaction", *Phys.Rev.*, vol. 79, pp. 350-356, 1950.

[2.27] J. C. Chapman, "Phase Coexistence in Manganites", University of Cambridge, Retrieved from http://www.msm.cam.ac.uk/dmg/papers/index.html, 2005.

[2.28] L. E. Hueso, L. Granja, P. Levy and N. D. Mathur, "Spintronic investigation of the phase separated manganite $(La,Ca)MnO_3$", *J. Appl. Phys.*, vol. 100, pp. 023903, 2006.

[2.29] M. Granada, J. C. R. Sanchez and L. B. Steren, "Giant magnetoresistance in oxide-based metallic multilayers", *Appl. Phys. Lett.*, vol. 91, pp. 072110, 2007.

[2.30] Y. Ogimoto, M. Izumi, A. Sawa, T. Manako, H. Sato, H. Akon, M. Kawasaki and Y. Tokura, "Tunneling Magnetoresistance above Room Temperature in $La_{0.7}Sr_{0.3}MnO_3/SrTiO_3/La_{0.7}Sr_{0.3}MnO_3$ Junctions", *Jpn. J. Appl. Phys,* vol. 42, pp. L369, 2003.

[2.31] Y. Ishii, H. Yamada, H. Sato, H. Akoh, M. Kawasaki and Y. Tokura, "Perovskite manganite magnetic tunnel junctions with enhanced coercivity contrast", *Appl. Phys. Lett.,* vol. 87, pp. 022509, 2005.

[2.32] R. A. de Groot, F. M. Mueller, P. G. v. Engen and K. H. J. Buschow, "New Class of Materials: Half-Metallic Ferromagnets", *Phys. Rev. Lett.,* vol. 50, pp. 2024-2027, 1983.

[2.33] K. Kobayashi, T. Kimura, H. Sawada, K. Terakura and Y. Tokura, "Room-temperature magnetoresistance in an oxide material with an ordered double-perovskite structure", *Nature,* vol. 395, pp. 677-680, 1998.

[2.34] Y. Ji, G. J. Strijkers, F. Y. Yang, C. L. Chien, J. M. Byers, A. Anguelouch, G. Xiao and A. Gupta, "Determination of the Spin Polarization of Half-Metallic CrO_2 by Point Contact Andreev Reflection", *Phys.Rev.Lett.,* vol. 86, pp. 5585-5588, 2001.

[2.35] F. Y. Yang, C. L. Chien, X. W. Li, G. Xiao and A. Gupta, "Critical behavior of epitaxial half-metallic ferromagnetic CrO_2 films", *Phys.Rev.B,* vol. 63, pp. 092403, 2001.

[2.36] M. Fonin, Y. S. Dedkov, R. Pentcheva, U. Rüdiger and G. Güntherodt, "Magnetite: a search for the half-metallic state", *Journal of Physics: Condensed Matter,* vol. 19, pp. 315217, 2007.

[2.37] S. Picozzi and A. J. Freeman, "Polarization reduction in half-metallic Heusler alloys: the effect of point defects and interfaces with semiconductors", *Journal of Physics: Condensed Matter,* vol. 19, pp. 315215, 2007.

[2.38] K. Schwarz, "CrO_2 predicted as a half-metallic ferromagnet", *Journal of Physics F: Metal Physics,* vol. 16, pp. 211-215, 1986.

[2.39] R. J. Soulen Jr., J. M. Byers, M. S. Osofsky, B. Nadgorny, T. Ambrose, S. F. Cheng, P. R. Broussard, C. T. Tanaka, J. Nowak, J. S. Moodera, A. Barry and J. M. D. Coey, "Measuring the Spin Polarization of a Metal with a Superconducting Point Contact", *Science,* vol. 282, pp. 85-88, 1998.

[2.40] M. I. Katsnelson, V. Y. Irkhin, L. Chioncel, A. I. Lichtenstein and R. A. de Groot, "Half-metallic ferromagnets: From band structure to many-body effects", *Rev. Mod. Phys.*, vol. 80, pp. 315, 2008.

[2.41] P. Dowben, "Half Metallic Ferromagnets", *Journal of Physics: Condensed Matter*, vol. 19, pp. 310301, 2007.

[2.42] J. Z. Sun, D. W. Abraham, R. A. Rao and C. B. Eom, "Thickness-dependent magnetotransport in ultrathin manganite films", *Appl. Phys. Lett.*, vol. 74, pp. 3017-3019, 1999.

[2.43] P. Orgiani, A. Y. Petrov, C. Adamo, C. Aruta, C. Barone, G. M. De Luca, A. Galdi, M. Polichetti, D. Zola and L. Maritato, "In-plane anisotropy in the magnetic and transport properties of manganite ultrathin films", *Phys. Rev. B*, vol. 74, pp. 134419, 2006.

[2.44] J. Dho and N. H. Hur, "Thickness dependence of perpendicular magnetic anisotropy in $La_{0.7}Sr_{0.3}MnO_3$ films on $LaAlO_3$", *Journal of Magnetism and Magnetic Materials*, vol. 318, pp. 23-27, 2007.

[2.45] M. He, J. Qiu, X. Liang, H. Lu and K. Jin, "Thickness-dependent surface morphology of $La_{0.9}Sr_{0.1}MnO_3$ ultrathin films", *Appl. Surf. Sci.*, vol. 253, pp. 6080-6084, 2007.

[3.1] W. Thomson, *Proc. R. Soc.*, vol. 8, pp. 546, 1857.

[3.2] W. Prellier, P. Lecoeur and B. Mercey, "Colossal-magnetoresistive manganite thin films", *Journal of Physics: Condensed Matter*, vol. 13, pp. R915-R944, 2001.

[3.3] A. Haghiri-Gosnet and J. Renard, "CMR manganites: physics, thin films and devices", *J. Phys. D*, vol. 36, pp. R127, 2003.

[3.4] M. N. Baibich, J. M. Broto, A. Fert, F. N. Van Dau, F. Petroff, P. Eitenne, G. Creuzet, A. Friederich and J. Chazelas, "Giant Magnetoresistance of (001)Fe/(001)Cr Magnetic Superlattices", *Phys.Rev.Lett.*, vol. 61, pp. 2472-2475, 1988.

[3.5] G. Binasch, P. Grnberg, F. Saurenbach and W. Zinn, "Enhanced magnetoresistance in layered magnetic structures with antiferromagnetic interlayer exchange", *Phys.Rev.B*, vol. 39, pp. 4828-4830, 1989.

[3.6] E. Grochowski, "HGST Areal Density Perspective", Hitachi, Retrieved from http://www.hitachigst.com/hdd/technolo/overview/chart02.html, 2003.

[3.7] GerstnerEd, "Nobel Prize 2007: Fert and Grunberg", *Nat. Phys.*, vol. 3, pp. 754-754, 2007.

[3.8] M. Ziese and S. P. Sena, "Anisotropic magnetoresistance of thin $La_{0.7}Ca_{0.3}MnO_3$ films", *Journal of Physics: Condensed Matter,* vol. 10, pp. 2727-2737, 1998.

[3.9] M. McCormack, S. Jin, T. H. Tiefel, R. M. Fleming, J. M. Phillips and R. Ramesh, "Very large magnetoresistance in perovskite-like La-Ca-Mn-O thin films", *Appl. Phys. Lett.*, vol. 64, pp. 3045-3047, 1994.

[3.10] R. Meservey and P. M. Tedrow, "Spin-polarized electron tunneling", *Physics Reports,* vol. 238, pp. 173-243, 1994.

[3.11] Y. Ogimoto, M. Izumi, A. Sawa, T. Manako, H. Sato, H. Akon, M. Kawasaki and Y. Tokura, "Tunneling Magnetoresistance above Room Temperature in $La_{0.7}Sr_{0.3}MnO_3/SrTiO_3/La_{0.7}Sr_{0.3}MnO_3$ Junctions", *Jpn. J. Appl. Phys*, vol. 42, pp. L369, 2003.

[3.12] J. Grollier, V. Cros, A. Hamzic, J. M. George, H. Jaffres, A. Fert, G. Faini, J. B. Youssef and H. Legall, "Spin-polarized current induced switching in Co/Cu/Co pillars", *Appl. Phys. Lett.*, vol. 78, pp. 3663-3665, 2001.

[3.13] N. F. Mott, "The Electrical Conductivity of Transition Metals", *Proc. Roy. Soc. (Lond.) A,* vol. 153, pp. 699, 1935.

[3.14] M. Ziese and M. J. Thornton, *Spin Electronics*, New York: Springer, 2001.

[3.15] E. Y. Tsymbal and D. G. Pettifor, "Perspectives of Giant Magnetoresistance", *Solid State Physics*, vol. 56, pp. 113-237, 2001.

[3.16] T. Valet and A. Fert, "Theory of the perpendicular magnetoresistance in magnetic multilayers", *Phys. Rev. B,* vol. 48, pp. 7099, 1993.

[3.17] S. S. P. Parkin, N. More and K. P. Roche, "Oscillations in exchange coupling and magnetoresistance in metallic superlattice structures: Co/Ru, Co/Cr, and Fe/Cr", *Phys. Rev. Lett.*, vol. 64, pp. 2304, 1990.

[3.18] K. R. Nikolaev, A. Bhattacharya, P. A. Kraus, V. A. Vas'ko, W. K. Cooley and A. M. Goldman, "Indications of antiferromagnetic interlayer coupling in $La_{2/3}Ba_{1/3}MnO_3/LaNiO_3$ multilayers", *Appl. Phys. Lett.*, vol. 75, pp. 118-120, 1999.

[3.19] K. R. Nikolaev, A. Y. Dobin, I. N. Krivorotov, W. K. Cooley, A. Bhattacharya, A. L. Kobrinskii, L. I. Glazman, R. M. Wentzovitch, E. D. Dahlberg and A. M. Goldman, "Oscillatory Exchange Coupling and Positive Magnetoresistance in Epitaxial Oxide Heterostructures", *Phys. Rev. Lett.*, vol. 85, pp. 3728-3731, 2000.

[3.20] K. R. Nikolaev, A. Y. Dobin, I. N. Krivorotov, E. D. Dahlberg and A. M. Goldman, "Temperature dependence of interlayer exchange coupling in manganite-based superlattices", *J. Appl. Phys.*, vol. 89, pp. 6820-6821, 2001.

[3.21] P. Bruno and C. Chappert, "Ruderman-Kittel theory of oscillatory interlayer exchange coupling", *Phys. Rev. B,* vol. 46, pp. 261, 1992.

[3.22] M. Sirena, N. Haberkorn, M. Granada, L. B. Steren and J. Guimpel, "Correlation between structure and magnetic properties of manganite-based multilayers", *J. Appl. Phys.*, vol. 93, pp. 7244-7246, 2003.

[3.23] P. Grunberg, D. E. Burgler, R. Gareev, D. Olligs, M. Buchmeier, M. Breidbach, B. Kuanr and R. Schreiber, "Experiments on the relation between GMR and interface roughness and on the interlayer exchange coupling across semiconductors", *J. Phys. D,* vol. 35, pp. 2403-2409, 2002.

[3.24] E. E. Fullerton, D. M. Kelly, J. Guimpel, I. K. Schuller and Y. Bruynseraede, "Roughness and giant magnetoresistance in Fe/Cr superlattices", *Phys. Rev. Lett.*, vol. 68, pp. 859, 1992.

[3.25] R. Schad, P. Beliën, G. Verbanck, C. D. Potter, H. Fischer, S. Lefebvre, M. Bessiere, V. V. Moshchalkov and Y. Bruynseraede, "Quantitative study of the interdependence OF interface structure and giant magnetoresistance in polycrystalline Fe/Cr superlattices", *Phys. Rev. B,* vol. 57, pp. 13692, 1998.

[3.26] X. Chen and R. H. Victora, "Effect of pinholes in magnetic tunnel junctions", *Appl. Phys. Lett.*, vol. 91, pp. 212104, 2007.

[3.27] V. Da Costa, C. Tiusan, T. Dimopoulos and K. Ounadjela, "Tunneling Phenomena as a Probe to Investigate Atomic Scale Fluctuations in Metal/Oxide/Metal Magnetic Tunnel Junctions", *Phys. Rev. Lett.*, vol. 85, pp. 876, 2000.

[3.28] B. J. Jonsson-Akerman, R. Escudero, C. Leighton, S. Kim, I. K. Schuller and D. A. Rabson, "Reliability of normal-state current--voltage characteristics as an indicator of tunnel-junction barrier quality", *Appl. Phys. Lett.*, vol. 77, pp. 1870-1872, 2000.

[4.1] J. Klein, C. Hofener, L. Alff and R. Gross, "Laser ablation of manganite thin films monitored by in situ RHEED", *J Magn Magn Mater*, vol. 211, pp. 9-15, 2000.

[4.2] P. F. Lee, J. Y. Dai and H. L. W. Chan, "Formation of Ge nanocrystals by utilizing nanocluster source", *Materials Science in Semiconductor Processing*, vol. 9, pp. 817-822, 2006.

[4.3] S. Foner, "Vibrating Sample Magnetometer", *Rev. Sci. Instrum.*, vol. 27, pp. 548, 1956.

[4.4] S. Foner, "Versatile and Sensitive Vibrating-Sample Magnetometer", *Rev. Sci. Instrum.*, vol. 30, pp. 548-557, 1959.

[4.5] S. Foner, "Review of magnetometry", *IEEE Transactions on Magnetics*, vol. 17, pp. 3358-3363, 1981.

[4.6] S. Foner, "The vibrating sample magnetometer: Experiences of a volunteer (invited)", *J. Appl. Phys.*, vol. 79, pp. 4740-4745, 1996.

[5.1] M. Koubaa, A. M. Haghiri-Gosnet, R. Desfeux, P. Lecoeur, W. Prellier and B. Mercey, "Crystallinity, surface morphology, and magnetic properties of $La_{0.7}Sr_{0.3}MnO_3$ thin films: An approach based on the laser ablation plume range models", *J. Appl. Phys.*, vol. 93, pp. 5227-5235, 2003.

[5.2] H. Yamada, M. Kawasaki and Y. Tokura, "Ru-doped $La_{0.6}Sr_{0.4}MnO_3$ thin films as a coercivity tunable electrode for magnetic tunnel junctions", *Appl. Phys. Lett.*, vol. 86, pp. 192505, 2005.

[5.3] X. Chen and R. H. Victora, "Effect of pinholes in magnetic tunnel junctions", *Appl. Phys. Lett.*, vol. 91, pp. 212104, 2007.

[5.4] S. Mukhopadhyay and I. Das, "Pinhole and tunneling conduction channels superimposed in magnetic tunnel junction: results and inferences", Retrieved from http://www.citebase.org/abstract?id=oai:arXiv.org:cond-mat/0603843, 2006.

[5.5] J. Dho, N. H. Hur, I. S. Kim and Y. K. Park, "Oxygen pressure and thickness dependent lattice strain in $La_{0.7}Sr_{0.3}MnO_3$ films", *J. Appl. Phys.*, vol. 94, pp. 7670-7674, 2003.

[5.6] L. E. Hueso, L. Granja, P. Levy and N. D. Mathur, "Spintronic investigation of the phase separated manganite (La,Ca)MnO_3", *J. Appl. Phys.*, vol. 100, pp. 023903, 2006.

[5.7] H. Y. Hwang, S. Cheong, N. P. Ong and B. Batlogg, "Spin-Polarized Intergrain Tunneling in $La_{2/3}Sr_{1/3}MnO_3$", *Phys.Rev.Lett.*, vol. 77, pp. 2041-2044, 1996.

[5.8] X. W. Li, A. Gupta, G. Xiao and G. Q. Gong, "Low-field magnetoresistive properties of polycrystalline and epitaxial perovskite manganite films", *Appl. Phys. Lett.*, vol. 71, pp. 1124-1126, 1997.

[5.9] K. Nishimura, Y. Kohara, Y. Kitamoto and M. Abe, "Magnetoresistance in magnetite films prepared from aqueous solution at room temperature", *J. Appl. Phys.*, vol. 87, pp. 7127-7129, 2000.

[5.10] H. Chang, T. C. Lu, H. C. Kuo and S. C. Wang, "Effect of oxygen on characteristics of nickel oxide/indium tin oxide heterojunction diodes", *J. Appl. Phys.*, vol. 100, pp. 124503, 2006.

[5.11] L. M. Wang, J. Lai, J. Wu, Y. -. Kuo and C. L. Chang, "Effects of Ru substitution for Mn on $La_{0.7}Sr_{0.3}MnO_3$ perovskites", *J. Appl. Phys.*, vol. 102, pp. 023915, 2007.

[5.12] A. Haghiri-Gosnet and J. Renard, "CMR manganites: physics, thin films and devices", *J. Phys. D*, vol. 36, pp. R127, 2003.

[5.13] W. F. Cheng and C. W. Leung, "Effect of Post Annealing on $La_{0.7}Sr_{0.3}MnO_3$ Thin Films", *Acta Phys Pol A*, vol. 111, pp. 117, 2007.

[5.14] L. P. Gor'kov and V. Z. Kresin, "Mixed-valence manganites: fundamentals and main properties", *Physics Reports*, vol. 400, pp. 149-208, 2004.

[5.15] E. Favre-Nicolin and L. Ranno, "Anisotropic magnetoresistance in manganite films", *Journal of Magnetism and Magnetic Materials*, vol. 272-276, pp. 1814-1815, 2004.

[5.16] B. Prijamboedi, H. Takashima and A. Shoji, "Surface morphology study of a $SrTiO_3$ thin film in a multilayer structure treated by chemical–mechanical polishing", *Journal of Crystal Growth*, vol. 283, pp. 163-169, 2005.

[5.17] N Gayathri, A K Raychaudhuri, X Q Xu, J L Peng and R L Greene, "Magnetoresistance of the metallic perovskite oxide $LaNiO_{3-\Delta}$", *Journal of Physics: Condensed Matter*, vol. 11, pp. 2901-2907, 1999.

[5.18] A. de Andres, J. Rubio, G. Castro, S. Taboada, J. L. Martinez and J. M. Colino, "Structural and magnetic properties of ultrathin epitaxial $La_{0.7}Ca_{0.3}MnO_3$ manganite films: Strain versus finite size effects", *Appl. Phys. Lett.*, vol. 83, pp. 713-715, 2003.

[5.19] J. Dho and N. H. Hur, "Thickness dependence of perpendicular magnetic anisotropy in $La_{0.7}Sr_{0.3}MnO_3$ films on $LaAlO_3$", *Journal of Magnetism and Magnetic Materials*, vol. 318, pp. 23-27, 2007.

[5.20] N. Gayathri, A. K. Raychaudhuri, X. Q. Xu, J. L. Peng and R. L. Greene, "Electronic conduction in $LaNiO_{3-\Delta}$: the dependence on the oxygen stoichiometry Δ", *Journal of Physics: Condensed Matter*, vol. 10, pp. 1323-1338, 1998.

[6.1] H. Yamada, M. Kawasaki and Y. Tokura, "Ru-doped $La_{0.6}Sr_{0.4}MnO_3$ thin films as a coercivity tunable electrode for magnetic tunnel junctions", *Appl. Phys. Lett.*, vol. 86, pp. 192505, 2005.

[6.2] W. F. Cheng, A. Ruotolo, Y. K. Chan, K. H. Wong and C. W. Leung, "Spacerless metal-manganite pseudo-spin-valve structure", *J. Appl. Phys.*, vol. 103, pp. 103903, 2008.

[6.3] M. Granada, J. C. R. Sanchez and L. B. Steren, "Giant magnetoresistance in oxide-based metallic multilayers", *Appl. Phys. Lett.*, vol. 91, pp. 072110, 2007.

[6.4] E. Y. Tsymbal and D. G. Pettifor, "Perspectives of Giant Magnetoresistance", *Solid State Physics*, vol. 56, pp. 113-237, 2001.

[6.5] T. Valet and A. Fert, "Theory of the perpendicular magnetoresistance in magnetic multilayers", *Phys. Rev. B*, vol. 48, pp. 7099, 1993.

[6.6] F. J. Jedema, A. T. Filip and van Wees, B. J., "Electrical spin injection and accumulation at room temperature in an all-metal mesoscopic spin valve", *Nature*, vol. 410, pp. 345-348, 2001.

[7.1] H. Yamada, M. Kawasaki and Y. Tokura, "Ru-doped $La_{0.6}Sr_{0.4}MnO_3$ thin films as a coercivity tunable electrode for magnetic tunnel junctions", *Appl. Phys. Lett.*, vol. 86, pp. 192505, 2005.

[7.2] Y. Ishii, H. Yamada, H. Sato, H. Akoh, M. Kawasaki and Y. Tokura, "Perovskite manganite magnetic tunnel junctions with enhanced coercivity contrast", *Appl. Phys. Lett.*, vol. 87, pp. 022509, 2005.

[7.3] M. C. Wu, A. Aziz, D. Morecroft, M. G. Blamire, M. C. Hickey, M. Ali, G. Burnell and B. J. Hickey, "Spin transfer switching and low-field precession in exchange-biased spin valve nanopillars", *Appl. Phys. Lett.*, vol. 92, pp. 142501, 2008.

[7.4] W. F. Cheng, A. Ruotolo, Y. K. Chan, K. H. Wong and C. W. Leung, "Spacerless metal-manganite pseudo-spin-valve structure", *J. Appl. Phys.*, vol. 103, pp. 103903, 2008.

[8.1] M. Granada, J. C. R. Sanchez and L. B. Steren, "Giant magnetoresistance in oxide-based metallic multilayers", *Appl. Phys. Lett.*, vol. 91, pp. 072110, 2007.